

GROWTH AND CHARACTERIZATION OF ZNO AND PZT FILMS FOR
MICROMACHINED ACOUSTIC WAVE DEVICES

Except where reference is made to the work of others, the work described in this dissertation is my own or was done in collaboration with my advisory committee. This dissertation does not include proprietary or classified information.

Sang Hoon Yoon

Certificate of Approval:

ZhongYang Cheng
Associate Professor
Materials Engineering

Dong-Joo Kim, Committee Chair
Associate Professor
Materials Engineering

Stuart M. Wentworth
Associate Professor
Electrical and Computer Engineering

Jong Wook Hong
Assistant Professor
Materials Engineering

George T. Flowers
Dean of the Graduate School
Graduate School

GROWTH AND CHARACTERIZATION OF ZNO AND PZT FILMS FOR
MICROMACHINED ACOUSTIC WAVE DEVICES

Sang Hoon Yoon

A Dissertation

Submitted to

the Graduate Faculty of

Auburn University

in Partial Fulfillment of the

Requirement for the

Degree of

Doctor of Philosophy

Auburn, Alabama
May 09, 2009

GROWTH AND CHARACTERIZATION OF ZNO AND PZT FILMS FOR
MICROMACHINED ACOUSTIC WAVE DEVICES

Sang Hoon Yoon

Permission is granted to Auburn University to make copies of this dissertation at its discretion, upon request of individuals or institutions and their expense. The author reserves all publication rights.

Signature of Author

Date of Graduation

VITA

Sang H. Yoon graduated from Metallurgical Engineering in Kookmin University, Seoul, Korea(R.O.K) in Feb. 1991, and obtained Master degree of Metallurgical Engineering in Feb. 1994. After graduation, he worked at Kookmin University as a Teaching Assistant, and taught several classes related to mechanical property of materials. He started his master degree in Material Science and Engineering of University of Florida and got Master degree in 2003. He continued his Ph. D. program in Materials Engineering of Auburn University, AL, USA from 2003. On November 01, 1995, he married with Mijeong Cha and lives with his spouse and two daughters, Insun Yoon and Adelina Soyoung Yoon.

DISSERTATION ABSTRACT

GROWTH AND CHARACTERIZATION OF ZNO AND PZT FILMS FOR
MICROMACHINED ACOUSTIC WAVE DEVICES

SANG HOON YOON

Doctor of Philosophy, May 9, 2009

(Master of Science and Engineering, University of Florida, 2002)

(Master of Engineering, Kookmin University, Korea (R.O.K.), 1994)

(B.E. Metallurgical Engineering, Kookmin University, Korea (R.O.K.), 1991)

219 Typed Pages

Directed by Dong-Joo Kim

The ability to detect the presence of low concentrations of harmful substances, such as biomolecular agents, warfare agents, and pathogen cells, in our environment and food chain would greatly advance our safety, provide more sensitive tools for medical diagnostics, and protect against terrorism. Acoustic wave (AW) devices have been widely studied for such applications due to several attractive properties, such as rapid response, reliability, portability, ease of use, and low cost. The principle of these sensors is based on a fundamental feature of the acoustic wave that is generated and detected by a piezoelectric material. The performance of the device, therefore, greatly depends on the properties of piezoelectric thin film. The required properties include a high piezoelectric

coefficient and high electromechanical coefficients. The surface roughness and the mechanical properties, such as Young's modulus and hardness, are also factors that can affect the wave propagation of the device. Since the film properties are influenced by the structure of the material, understanding thin film structure is very important for the design of high-performance piezoelectric MEMS devices for biosensor applications.

In this research, two piezoelectric thin film materials were fabricated and investigated. ZnO films were fabricated by CSD (Chemical Solution Deposition) and sputtering, and PZT films were fabricated by CSD only. The process parameters for solution derived ZnO and PZT films, such as the substrate type, the effect of the chelating agent, and heat treatment, were studied to find the relationship between process parameters and thin film structure. In the case of the sputtered ZnO films, the process gas types and their ratio, heat treatment in situ, and post deposition were investigated. The key results of systematic experiments show that the combined influence of chemical modifiers and substrates in chemical solution deposition have an effect on the crystallographic orientation of the films, which is explained by the phase transformation that occurs from amorphous pyrolyzed film to crystalline film. Sputtered ZnO films do not show a strong dependence on the parameters, possibly indicating a reduced energy barrier for the growth of ZnO film due to plasma energy. Based on an understanding of the relationship between process and thin film structure, the growth mechanism of CSD ZnO is proposed. The devices are fabricated on 4-inch silicon wafers by a microelectronic fabrication method. The fabrication procedure and issues relating to device fabrication are discussed.

ACKNOWLEDGMENTS

I would like to express my respects and thanks to my advisor Dr. Dong-Joo Kim for their directions, patience, and encouragement. Without his invaluable advices, this dissertation would not be finished. Thanks are also due to Dr. Stuart M. Wentworth, Dr. ZhongYang Cheng, Dr. Jong Wook Hong, and Dr. Minseo Park for their help and advice. They gave me a challenging subject to solve. I would like to thank my colleagues, Jung-Hyun Park, Dongna Shen, Dan Liu, Hosang Ahn, Seon-Bae Kim, Dr. H. Clyde Wikle, Dr. Joo-Hyon Noh, and Dr. Youngho Kim. I also wish to acknowledge Mr. Michael Johnson, Mr Roy Howard, and Mr. Charles D. Ellis for their help during my doctoral course.

I would like to express special thanks to my parents, Young-Shik Yoon and Jung-Ja Kim, for their belief in me without question. The memory that my father studied still lives in my mind and gives me strength to finish this long journey. Also, I would like to thank my wife, Mijeong Cha to take care of the children and me while I am in my doctoral course. I would like to express my love to my daughters, Insun Yoon and Soyoung Yoon. They have grown strong even though I have not spent much time with them. This dissertation is so worthy to me not because I did it, but because my family did it altogether. Finally, I would like to express my deep appreciation to my mother-in-law, Ms. Seung-Youn Choi, who passed away in 2006 during my doctoral course. She always encouraged me in my study, when I was depressed. Still I miss her so much.

Style manual or journal used Guide to Preparation and Submission of Theses and
Dissertations

Computer software used Microsoft Word 2003 and Origin 7.

TABLE OF CONTENTS

LIST OF FIGURES	xi
LIST OF TABLES	xvii
CHAPTER 1 INTRODUCTION	1
1.1 Motivation.....	1
1.2 Research Objectives and Dissertation Organization.....	4
CHAPTER 2 LITERATURE SURVEY OF ZNO AND PZT FILMS AND BACKGROUND OF FPW DEVICE	6
2.1 Piezoelectric Materials for FPW Device.....	6
2.1.1 ZnO	7
2.1.2 PZT	11
2.2 Piezoelectric Property	23
2.2.1 Piezoelectricity.....	23
2.2.2 Electromechanical Coupling Coefficient.....	32
2.3 Acoustic Wave Devices and FPW device.....	33
2.3.1 Acoustic Wave Devices.....	33
2.3.2 FPW Device.....	35
CHAPTER 3 ZNO FILMS BY CHEMICAL SOLUTION DEPOSITION (CSD).....	39
3.1 Introduction.....	39
3.2 Detailed Experiment	41
3.3 Parametric Study of Precursors.....	45
3.4 Nucleation and Growth Mechanism of CSD ZnO Film	56
3.5 Raman Characterization on Thin Film Structure.....	65
3.6 Evolution of Morphology and Surface Topograph.....	77
3.7 Conclusion	79
CHAPTER 4 ZNO FILM DEPOSITION BY SPUTTERING METHOD.....	82
4.1 Introduction.....	82
4.2 Detailed Experiment	86
4.3 High Crystallinity and Morphology Evolution of Sputtered ZnO films through the modification of Substrate and Heat treatment	88
4.4 Microstructural Evolution of Crystalline ZnO films influenced by Sputtering Gas and Pressure.....	100
4.5 Stress analysis with Defects Consideration by Raman Spectroscopy	106
4.6 Hardness and Modulus Investigation of ZnO films with Gas Effect.....	115

4.7 Conclusion	118
CHAPTER 5 PZT FILMS BY CHEMICAL SOLUTION DEPOSITION (CSD).....	120
5.1 Introduction.....	120
5.2 Detailed Experiment	125
5.3 Precursor Study by Solution Chemistry.....	128
5.4 Film Orientation Evolution by Nucleation and Growth Mechanism.....	132
5.5 Raman Characterization on Film Stress.....	146
5.6 Ferroelectric Property of CSD PZT Films with film Orientation.....	154
5.8 Conclusion	157
CHAPTER 6 DEVICE FABRICATION AND CHARACTERIZATION.....	159
6.1 Introduction.....	159
6.2 Device Fabrication Process and Issues	161
6.3 Device Design and Characterization.....	165
6.4 Conclusion	185
CHAPTER 7 CONCLUSION OF DISSERTATION AND FUTURE WORK	186
7.1 Conclusion of Dissertation.....	186
7.2 Future Work.....	189
BIBLIOGRAPHY.....	190

LIST OF FIGURES

2.1 Wurtzite hexagonal structure of ZnO	7
2.2 Crystal structure of perovskite PZT	12
2.3 Schematic diagram of B-site ion movement by external electric field.....	14
2.4 Schematic diagram of	15
a) tetragonal polarization in $\langle 100 \rangle$ direction and resultant shape change due to the polarization	
b) rhombohedral polarization in $\langle 111 \rangle$ direction and resultant shape change due to the polarization	
2.5 Schematic diagram of 180° and 90° domain walls	16
2.6 Schematic diagram of poling effect on the electric dipoles.....	18
2.7 Typical hysteresis loop of ferroelectric materials with schematic diagram of crystal lattice cell.....	20
2.8 Phase diagram of $\text{PbZrO}_3 - \text{PbTiO}_3$ compounds	22
2.9 Displacement graphs in respect to electric field	26
a) Electrostriction	
b) Piezoelectricity	
c) Ferroelectricity	
2.10 The response of the materials, b) piezoelectric and c) ferroelectric in terms of time according to the applied electric field a).....	27
2.11 Relations between electrical and mechanical variables	31
2.12 Frequency and amplitude changes by measurands	35
2.13 Top, side and particle displacement of FPW device.....	37
3.1 Experimental procedure of ZnO film fabrication by sol-gel method, which shows 20 coatings to reach over 600nm thickness with 0.7M solution.....	43

3.2 FTIR of the precursor at 0.5M concentration with different chelating agents.....	46
3.3 Results of TG/DSC for DEA- and MEA-chelated precursor for the fabrication of ZnO films by Sol-Gel method.....	52
a) DSC graph	
b) TG graph	
3.4 XRD results for DEA- and MEA-chelated precursor for the fabrication of 10 layers of ZnO films by Sol-Gel method on Pt(111) oriented layered silicon wafer from 200 to 700°C temperature range in one step heat treatment scheme	53
a) ZnO films with DEA chelated precursor	
b) ZnO films with MEA chelated precursor	
3.5 XRD results of 5 coatings ZnO films fabricated by DEA-chelated 0.1M solution concentration with the variation of:	54
a) Annealing temperature from 500°C to 700°C	
b) Pyrolysis temperature from 200°C to 400°C	
3.6 XRD data of 5 coated ZnO films deposited onto various substrates with same heat treatment of 300°C pyrolysis and 700°C annealing condition with DEA chelated solution of 0.1M solution concentration in:	57
a) Linear scale	
b) Log scale	
3.7 Schematic diagram of crystallographic surface configuration between ZnO(002) and Pt(111) and Pt(200)	61
3.8 X-ray diffraction patterns of ZnO films grown on different substrates from sol-gel solutions modified by two different chelating agents of 0.5M solution concentration, pyrolyzed at 300°C for 10min and annealed at 700°C for 1hr.....	63
a) with MEA chelated solution on SiNx/Si substrate	
b) with MEA chelated solution on Pt(111)/Si substrate	
c) with DEA chelated solution on SiNx/Si substrate	
d) with DEA chelated solution on Pt(111)/Si substrate.	
3.9 Schematic diagram of energy barriers of DEA- and MEA-chelated solutions.....	64
3.10 FTIR spectrum of CSD ZnO films with 0.7M precursors	67
3.11 Raman data for the study of the pyrolysis temperature effect on 20 coated ZnO film with 0.7M solution concentration.....	70-71
a) ZnO films derived by DEA-chelated precursor annealed at 700°C with different pyrolysis temperature	
b) ZnO films derived by MEA-chelated precursor annealed at 700°C with different pyrolysis temperature	

c) ZnO films derived by DEA-chelated precursor pyrolyzed at 300°C with different annealing temperature	
d) ZnO films derived by MEA-chelated precursor pyrolyzed at 300°C with different annealing temperature	
3.12 E ₂ mode of ZnO single crystal by Raman experiment.....	72
3.13 Raman data of E ₂ mode in 20 coated ZnO films on Pt(111)/Si substrate with different chelating agent and different heat treatment by 0.7M solution concentration.....	73-74
a) with DEA-chelated precursor with 200°C - 400°C pyrolysis and 700°C annealing	
b) with MEA-chelated precursor with 200°C - 400°C pyrolysis and 700°C annealing	
c) with DEA-chelated precursor with 500°C - 700°C annealing and 300°C pyrolysis	
d) with MEA-chelated precursor with 500°C - 700°C annealing and 300°C pyrolysis	
3.14 SEM images of ZnO films prepared at different conditions by 0.1M DEA chelated precursor	78-79
a) pyrolyzed at 300°C and annealed at 500°C on Pt(111)/Si	
b) pyrolyzed at 300°C and annealed at 700°C on Pt(111)/Si	
c) pyrolyzed at 300°C and annealed at 500°C on Pt(002)/Si	
d) pyrolyzed at 300°C and annealed at 700°C on Pt(002)/Si	
e) pyrolyzed at 300°C and annealed at 500°C on amorphous SiN _x /Si	
f) pyrolyzed at 300°C and annealed at 700°C on amorphous SiN _x /Si	
3.15 AFM surface morphology of ZnO films grown on Pt(111)/Si and amorphous SiN _x /Si substrates (pyrolysis = 300°C, annealing = 700°C, film thickness = 360 nm)	79
4.1 Schematic diagram of the configuration of sputtering system.....	87
4.2 XRD patterns of the sputtered ZnO films deposited at RT on different substrates ...	89
4.3 SEM images of 1 um thick ZnO films prepared by sputtering deposition at different substrates. The gas ratio is Ar:O ₂ =3:1. All films were deposited at room temperature	90
a) Pt(111)/Si	
b) Pt(200)/Si	
c) Si ₃ N ₄ /Si	

4.4 AFM images of 1 μm thick ZnO films prepared by sputtering deposition at different substrates. The gas ratio is Ar:O ₂ =3:1. All films were deposited at room temperature	92
a) Pt(111)/Si	
b) Pt(200)/Si	
c) Si ₃ N ₄ /Si	
4.5 The effect of the matched and mismatched substrates on the nucleation and growth of ZnO films oriented in the <002> direction.	95
4.6 XRD patterns of the sputtered ZnO films deposited at RT with various heat treatment with Ar:O ₂ =1:1 ratios on Pt(111) substrate	97
4.7 XRD patterns of the sputtered ZnO films deposited at RT with various gas ratio ..	101
4.8 SEM images of ZnO films with various gas ratio. The films were deposited at RT without annealing process onto Pt(111).....	102
4.9 Stress variation with the variation of gas ratio by Raman spectroscopy of ZnO films onto Pt(111)- and Pt(200)-oriented layered silicon wafers.....	108
4.10 Raman spectroscopy of ZnO films deposited on Pt(111) with Ar:O ₂ =1:1 and various heat treatments.	111
4.11 Raman shift for evaluation of stress in ZnO films deposited on Pt(111) with Ar:O ₂ =1:1 and various heat treatments.....	113
4.12 Schematic diagram of the effect of substrate temperature on the bombardment of energetic particles onto the substrate.	113
4.13 Hardness and modulus of ZnO films deposited at RT with various gas ratios on SiN substrate, measured by Nanoindentation.	116
5.1 Fabrication procedure of PZT precursor.....	124
5.2 Experimental procedure diagram of PZT film fabrication by sol-gel.....	126
5.3 Infra-red spectra of PZT precursors with/without AcAc	127
a) as synthesized, but aged over 72 hours at RT	
b) heat treated below 110°C for 12 hours	
5.4 XRD results of solution derived PZT thin films on Pt(200)/Si substrate	133
a) with acetylacetone	
b) without acetylacetone	

5.5 XRD result of solution derived PZT thin films on Pt(111)/Si substrate.....	134
a) with acetylacetone	
b) without acetylacetone	
5.6 XRD results of PZT films with a heat treatment of 700°C.....	136
5.7 Fluorite structure (left) and perovskite structure (right).	137
5.8 SEM images of PZT films derived by the solution with AcAc on Pt(111) with 700°C annealing temperature and with different pyrolysis temperature at	142
a) 250°C	
b) 350°C	
c) 450°C	
d) 700°C heat treatment only	
5.9 SEM images of PZT films with 250°C pyrolysis - 700°C annealing	144
a) on Pt(111) derived by the solution with AcAc	
b) on Pt(111) derived by the solution without AcAc	
c) on Pt(200) derived by the solution with AcAc	
d) on Pt(200) derived by the solution without AcAc	
5.10 SEM image of PZT film with only 700°C heat treatment on Pt(111)	145
5.11 AFM images of PZT films with 250°C pyrolysis - 700°C annealing.....	145
a) on Pt(111) derived by the solution with AcAc	
b) on Pt(111) derived by the solution without AcAc	
5.12 Raman spectroscopy results of PZT films with 3 layers fabricated by a heat treatment of 250 °C pyrolysis and 700°C annealing.....	152
a) on Pt(111) with and without AcAc	
b) on Pt(200) with and without AcAc	
5.13 Raman spectroscopy results of PZT films with 3 layers fabricated with various heat treatment conditions on Pt(111) substrate.....	153
5.14 Hysteresis loops of PZT films.....	154
5.15 Remanent Polarization of PZT films	155
6.1 FPW device fabrication procedure.....	164
6.2 Schematic diagram of Network analyzer set-up for device characterization	165

6.3 Calculated antisymmetric and symmetric modes of Lamb waves.....	166
6.4 Schematic diagram of IDT design	176
6.5 Mask design of FPW device array in this study	179
6.6 The array of FPW device a) front side view, and b) backside view (KOH etched side).....	181
6.7 FPW device response with sputtered ZnO film.	183
a) FPW device with 150 μ m of IDT period, 25 pairs of IDT, 1550 μ m of aperture	
b) Frequency range of 1MHz to 2MHz according to (a)	
c) FPW device with 100 μ m of IDT period, 25 pairs of IDT, 750 μ m of aperture	
d) Frequency range of 3MHz to 4MHz according to (c)	
6.8 FPW device response of three different device design.....	184

LIST OF TABLES

3.1 Summary of Raman data with 20 coated ZnO films on Pt(111)/Si substrate with different chelating agent and different heat treatment by 0.7M solution concentration	75
5.1 Summary of the remanent polarization values of 3-layered PZT films on Pt(111) with different fabrication conditions with film orientation investigation.....	157
6.1 FPW device fabrication issues	163

CHAPTER 1

INTRODUCTION

1.1 Motivation

The marvelous growth of the biosensor market, which is around \$10 billion [1], has resulted from newly emerging applications across a wide range that includes analyzing, monitoring, and controlling for medical, environmental, microbiological, and industrial fields. Biosensors use several transduction modes: electrochemical (e.g. ion-selective electrode and solid electrolyte gas sensors), optical (e.g. optical fibers and surface plasmon resonance), acoustic (e.g. piezoelectric materials, SAW, and FPW), and thermal (calorimetric sensors). The optical and acoustic transduction modes have attracted more attention in biosensors due to their fast response to analytes [2]. In particular, the sensor technology based on acoustic wave (AW) devices offers advantages over the optical-based sensors [3] since they do not require expensive microscopic optical components and time for laser alignment, and the read-out electronic circuit of acoustic

devices can be easily integrated on a conventional silicon wafer. AW devices use piezoelectric materials for transducing the mechanical perturbation to an electric signal, and vice versa. Among piezoelectric materials for such devices, zinc oxide (ZnO) and lead zirconate titanate (PZT) are considered to be excellent candidates.

ZnO is a well-known n-type wide band gap semiconductor of 3.4eV with a direct band gap and a relatively high exciton binding energy of 60meV [4]. The electrical properties of ZnO films can easily be modified by doping elements such as Al, Ga, In, NH₃, and hydrogen gas [4, 5]. And, ZnO can even exhibit ferromagnetism by doping with some transition metal elements such as V, Cr, Fe, Co, and Ni [4, 5]. In addition to electric properties, other advantages such as no toxicity, chemical stability, biocompatibility, and compatibility of micromachining processes allow ZnO to be exploited for a wide range of applications. Regarding the properties relevant to piezoelectric devices, it is reported that ZnO has an attenuation of 35.9dB/ μ s at 1 GHz and electromechanical coupling coefficients of $\sim 7.8\%$ [6]. It has a piezoelectric constant of $e_{33} : 0.89$ and $e_{31} : -0.51$ [7], and the dielectric constant of ZnO has been reported to be 8.2 [8].

Another excellent candidate material for piezoelectric devices is PZT (Lead Zirconia Titanate). PZT is a ferroelectric material and has attracted much attention for

electronic devices, such as electro-optics [9, 10], ferroelectric memories [11-13], non-volatile memories [14, 15], and ferroelectric field effect transistors (FET) [16]. These applications result from the ferroelectric nature of the films, which have electromechanical coupling coefficients of $\sim 20.25\%$ [6], and piezoelectric coefficients of $e_{33} : \sim 240$ [17], $e_{31} : \sim -32.4$ [18]. The dielectric constant of PZT has been reported to be 1180 [19] at the MPB (Morphotropic Phase Boundary), which is much higher than that of ZnO and means that it can be utilized for actuator applications.

The performance of micromachined piezoelectric devices is strongly related to the material properties, which are determined by process and structure. Therefore, understanding the relationship between process, structure, and properties is very important for advancing the knowledge of thin film piezoelectric materials and for improving piezoelectric devices.

In this research, two piezoelectric thin film materials were fabricated and investigated. ZnO films were fabricated by Chemical Solution Deposition (CSD) and sputtering, and PZT films were fabricated by CSD. The process parameters for solution-derived ZnO and PZT films, such as the substrate type, the effect of the chelating agent, and heat treatment, were studied to find the relationship between process parameters and thin film structure. In case of the sputtered ZnO films, the process gas types and their

ratios, heat treatment in situ, and post deposition were investigated. The key results of systematic experiments show that the combined influence of chemical modifiers and substrates in chemical solution deposition have an effect on the crystallographic orientation of the films, which is explained by the phase transformation that occurs from amorphous pyrolyzed film to crystalline film. Sputtered ZnO films do not show a strong dependence on the parameters, possibly indicating a reduced energy barrier for the growth of ZnO film due to plasma energy. Based on an understanding of the relationship between process and thin film structure, the growth mechanism of CSD ZnO is proposed. Under the optimized conditions for AW device applications, the devices are fabricated on 4-inch silicon wafers by a microelectronic fabrication method. The fabrication procedure and the issues relating to device fabrication are discussed, along with film properties.

1.2 Research Objectives and Dissertation Organization

The main objective of this research is to investigate the properties of ZnO and PZT films in order to develop a rapid and selective biosensor to detect pathogenic bacteria. ZnO films were fabricated by CSD and sputtering for a FPW device, and PZT films were fabricated by CSD. Because the piezoelectricity is greatly dependant on the

material properties, such as microstructural texture, crystallinity, and surface roughness of the films, controlling the material properties by tailoring the process parameters is the primary method for achieving better device performance for the AW applications.

The first chapter of this dissertation is the introduction, which includes the motivation and the background of this study, as well as the overall organization of this entire document. In the second chapter is presented a literature review, which consists of the theoretical section, as well as the background of piezoelectric materials and AW devices. The third chapter presents the work related to solution-derived ZnO film, including experimental, results, and discussion sections. This also includes the results of the characterization tools for film properties, as well as explanations and reasons for the phenomena that resulted from this study. The fourth and fifth chapters follow this same format for the sputtered ZnO film and the solution-derived PZT film, respectively. The fabrication of an FPW device using the sputtered ZnO film is shown in the sixth chapter. The seventh chapter is the conclusion and summary for this study, including a plan for future work.

CHAPTER 2

LITERATURE SURVEY OF ZNO AND PZT FILMS AND BACKGROUND OF FPW DEVICE

2.1 Piezoelectric Materials for FPW Device

Piezoelectric ZnO and PZT films have been the materials of choice for FPW devices. There have been numerous studies on piezoelectric ZnO and PZT films as promising materials for acoustic wave device applications of sensors and actuators. Due to their piezoelectric property, the electric signal given by input IDT (Interdigital Transducer) can produce mechanical deformation of the materials that is sufficient to launch the acoustic wave propagating within the membrane of an FPW device, with the shear deformation being converted to an electric signal at the output IDT. Thus, a highly textured structure is necessary for the piezoelectric materials used for the acoustic wave device application. Moreover, large piezoelectric coefficients and electromechanical coupling coefficients are other requirements for better device performance, because these

properties are related to the efficiency with which the RF voltage applied to the IDT couples to the mechanical deformation [20]. Since the acoustic wave is propagating through the membrane, the roughness of the device surface is another factor to be investigated.

2.1.1 ZnO

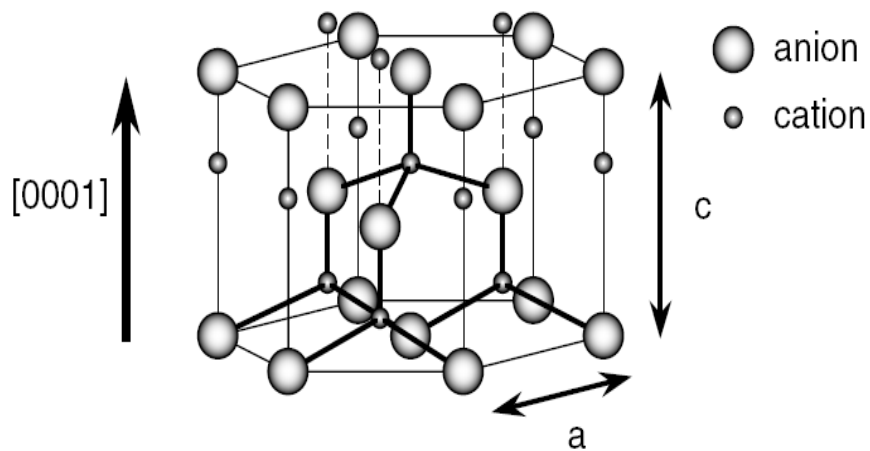


Fig. 2.1 Wurtzite hexagonal structure of ZnO

ZnO films have attracted intensive researcher's interest due to their wide range of applications by their versatile properties and the ease with which these properties may be modified. Methods of fabricating ZnO films include pulsed laser deposition [21, 22], hydrothermal synthesis [23], chemical vapor deposition [24, 25], RF and DC sputtering

[26-28], spray pyrolysis [29, 30], plasma-assisted molecular-beam epitaxy (PMBE) [31, 32] and solution deposition [33-36].

Crystalline ZnO can have one of three structures: wurtzite hexagonal structure, zinc blende cubic structure, and rock salt cubic structure; depending on the fabrication process conditions. The zinc blende cubic structure can only be achieved by fabricating on a cubic substrate [37], and high pressure is needed to stabilize the rock salt cubic structure [38, 39]. Thus, under ordinary fabrication process conditions, the thermodynamically stable (at room temp.) wurtzite hexagonal structure (see fig. 2.1) is usually obtained. In this structure, due to the sp^3 hybridization of the oxygen 2p orbital and the zinc 3d orbital, each atom of one kind is surrounded by 4 corresponding atoms of another kind in the tetrahedron located at the corners. Due to the tetrahedral coordination of the Wurtzite structure, the bonding distance of the nearest neighbored 4 corresponding atoms are the same and the next nearest neighbored 12 same kinds of atoms are also identical. In the ZnO structure, a bi-atomic element composed of one pair of Zn and O atoms is arranged along the $\langle 0001 \rangle$ direction, alternatively. Conventionally, due to the bi-atomic feature, $(000\bar{1})$ plane indicates the basal plane composed with O atoms in a hexagonal unit cell, and (0001) plane with Zn atoms, and the positive z direction in polarity is defined by the direction from the O-plane to Zn-plane. Due to such a crystal

structure with the alternative layers of Zn and O, the dipole is aligned with the c-axis. Thus, the piezoelectric property of ZnO film comes from the alignment of the layers. Under stress, the dipole distance can be changed, thereby producing the piezoelectric effect. Thus, the main concern of ZnO film fabrication is on the set-up of the preferred c-axis and how it is oriented in the film. The Wurtzite hexagonal structure has an ideal ratio of $c/a = \sqrt{8/3} = 1.633$, and belongs to the space group of C_{6v}^4 or $P6_3mc$. However, in real ZnO, the ratio is not the same as the ideal one, $a=3.283 \text{ \AA}$ and $c=5.309 \text{ \AA}$ [40], so that $c/a = 1.617$. The reason for this difference between the ideal and the real ratios may be the lattice stability and ionic character [41], which is dependent on the difference in electronegativity of the constituent atoms.

ZnO is a Group II-VI binary compound semiconductor, which has a wide band gap of 3.3eV [42] at room temperature. Moreover, ZnO has a direct band gap and a large exciton binding energy of 60 meV [43], resulting in a low power threshold for optical pumping such that it can be used for an ultraviolet light emitting diodes (LEDs) [44] and laser diodes (Lds). Because it is transparent due to the wide band gap, its applications can be expanded to transparent conducting electrodes [45] in display devices, photovoltaics, and solar cell windows [44, 46]. The main concept of the transparent conductor is related by its nature to the high conductivity of the film. The high conductivity of ZnO film can

be achieved in two ways. One is to increase intrinsic charge carriers by lattice defects, such as zinc and oxygen vacancies, which are well-known common lattice defects in ZnO [47]. The other is to introduce extrinsic charge carriers by doping. By modifying the doping level, the doped ZnO can possess a metal-like characteristic in its conductivity. ZnO is an n-type semiconductor, and commonly Group-III elements [48], such as Al [49-52], Ga [34, 53, 54], and In [53, 55-57], have been used as the doping elements. For instance, undoped ZnO film has a resistivity of $3.2 \times 10^{-3} \Omega\text{cm}$ [48] due only to intrinsic charge carriers. But a lower resistivity of $1.2 \times 10^{-4} \Omega\text{cm}$ [54] can be achieved by Ga-doping with the CVD method, which is comparable to several metals within one or two orders of magnitude; for example, $0.01712 \times 10^{-4} \Omega\text{cm}$ for Cu, $0.1073 \times 10^{-4} \Omega\text{cm}$ for Pt, and $1.44 \times 10^{-4} \Omega\text{cm}$ for Mn [58]. Even though ZnO is naturally an n-type semiconductor, there has been intensive research to fabricate p-type ZnO, because in LED applications, both n-type and p-type ZnO films are needed. However, it has been reported that the p-type ZnO cannot be easily achieved. One of the reasons is the dopant compensation [59, 60] by native defects, such as zinc interstitials and oxygen vacancies [61]. Doping can not only change the conductivity and the band-gap of ZnO [62], but it can also change ZnO to a ferromagnetic material if transition metals are used, such as Mn, Co, Fe, Cr, and Co

[41, 63]. However, the doping of the transition metals into ZnO is difficult due to their low solubility [64].

In contrast with the applications of the film related to its conductivity, MEMS applications, such as sensors [65, 66], actuators [67], and acoustic wave transducers [68], utilize the high resistivity of the film [69]. This is because a higher degree of electrical conduction in the film can act as an energy drain in such applications. For biosensor applications, candidate materials should be nontoxic, chemically stable, and biocompatible [70]. In addition to those properties, materials for MEMS applications are required to have a high electromechanical coupling coefficient, high dielectric constant, and high piezoelectric coefficient for the better device performance. It has been reported that ZnO films have high piezoelectric constants (e_{33} : 0.89, e_{31} : -0.51 [7]) and high electromechanical coupling coefficients ($k^2 = \sim 7.8\%$ [6], and 9% [71]). As a reference, $k^2 \approx 18\%$ for single crystals.

2.1.2 PZT

According to Jaffe [19], ferroelectricity is defined as the reversibility in the direction of the electric dipole in a polar crystal under an external electric field.

Ferroelectricity was first reported on single crystal Rochelle salt ($\text{KNaC}_4\text{H}_4\text{O}_6 \cdot 4\text{H}_2\text{O}$) by J. Valasek [72]. This is due to its tetragonal structure, which causes this material to be ferroelectric even at room temperature [73]. After the discovery of Barium titanate, the piezoelectric property of Lead zirconate titanate was reported by B. Jaffe in 1954 [74]. Lead zirconia titanate (PZT) film is one of the well-known ferroelectric materials that has a wide range of applications from MEMS to electric components, such as acoustic wave devices [75], and memories [76-78]. This is due to its high piezoelectric constant (PZT film: $e_{33} : \sim 240$ [17], $e_{31} : \sim 32.4$ [18]), high dielectric constant (>1000), and high electromechanical coupling coefficients.

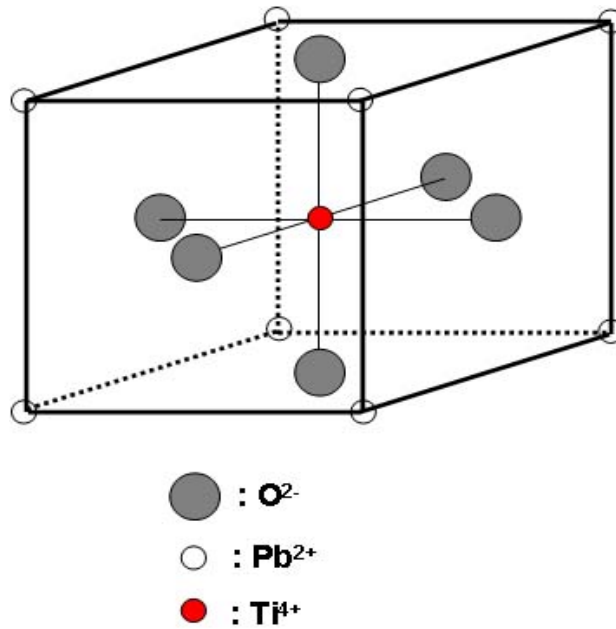


Fig. 2.2 Crystal structure of perovskite PZT

For MEMS applications, the utilization of the ferroelectric material as a piezoelectric results from its crystal asymmetry and high dielectric constant. The high dielectric constant can also be utilized for capacitor applications. For memory applications, ferroelectric materials have attracted a lot of attention by researchers. This is due to several reasons: first, they can be fabricated as a thin and high quality film, which can be switched at low voltage compared with bulk PZT; their large switching polarization which leads to a large read/write cycle; and due to their machinability onto integrated circuits. However, the high processing temperature of this material often makes it incompatible with other components in the integrated circuit, leading to difficulty in its use for these applications.

There is a transition temperature in ferroelectricity, similar to the case of ferromagnetism. It is called the 'Curie point' T_c , which is expressed as $\varepsilon = \frac{C}{(T - T_\theta)}$, where ε is the permittivity, C is the Curie constant, and T_θ is Curie-Weiss temperature, which is near to but not exactly the same as T_c [79]. The permittivity increases with temperature up to a maximum at T_c , then falls off at higher temperatures. This is because, above T_c , ferroelectric materials transform to a centrosymmetric cubic structure. Due to the central symmetry of this cubic structure where all axes are identical through the center of the crystal, the material is no longer ferroelectric or piezoelectric. The crystal

structure of PZT is shown in fig. 2.2, which is a cubic perovskite structure composed of A-sites (Pb^{2+}) at the 8-corners, a B-site at the center (Ti^{4+}), and oxygen ions (O^{2-}) at the 6-faces. Because the Ti^{4+} ion is small relative to the size of the B-site, this cation can move to any face at which an oxygen ion is located. The reduced bonding between Ti^{4+} and O^{2-} by the small size of Ti^{4+} creates the unit cell contraction in the direction perpendicular to the reduced bonding direction. The resultant structure is tetragonal, which does not have centrosymmetry, so that a permanent dipole can exist in the structure. Below T_c , as described earlier, the cubic structure transforms to tetragonal symmetry which has one elongated side. In words, the elongated side also permits the Ti ion to move up and down between the large oxygen atoms according to the external electric field, as shown in fig.

2.3.

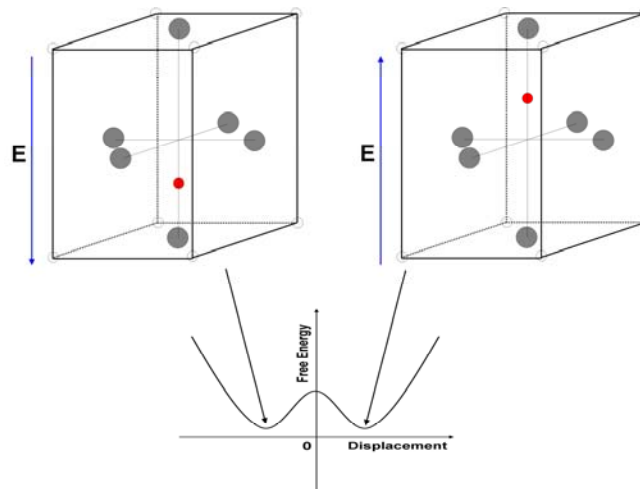


Fig. 2.3 Schematic diagram of B-site ion movement by external electric field

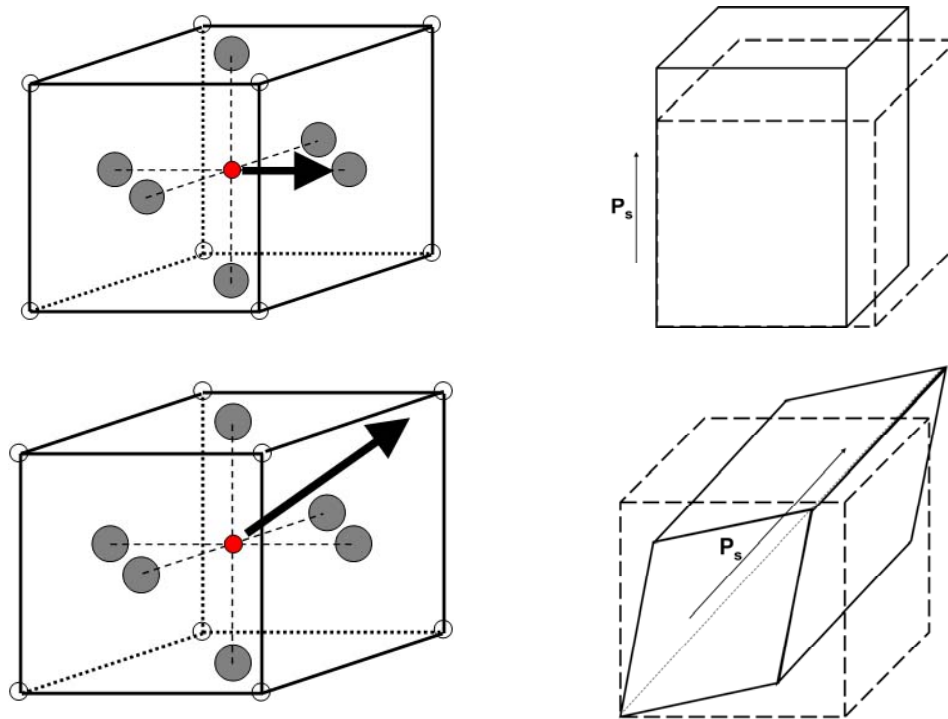


Fig. 2.4 Schematic diagram of
 a) tetragonal polarization in $\langle 100 \rangle$ direction and resultant shape change due to the polarization
 b) rhombohedral polarization in $\langle 111 \rangle$ direction and resultant shape change due to the polarization

The movement of the Ti ion causes charge separation depending on the direction of the movement, and produces an electric dipole behavior and spontaneous polarization. The location of the Ti ion can be determined by a minimum in the free energy term as shown in fig. 2.3. The spontaneous polarization in tetragonal PZT is not limited to the c-axis. All six $\langle 100 \rangle$ directions in the tetragonal structure and all eight $\langle 111 \rangle$ directions in the rhombohedral structure have the same probability to have this polarization, as shown in fig. 2.4. Polarization switching is caused by the shifting of the Ti ion up and down in

the crystal structure causes the polarization switching, and is classified into two categories: Ferroelectric switching, which is due to the application of an external electric field to the crystal that is larger than the coercive field (E_c); and ferroelastic switching, which is generated by the application of a stress to the crystal.

When a uniform alignment of the spontaneous polarization exists in a certain area, the localized dipole region is called a domain, which has a homogeneous and spontaneous polarization. The boundary of the neighboring domains is called a domain wall [80] whose motion is the source of the hysteresis loop and nonlinear piezoelectric property. The neighboring domains have different polarization directions.

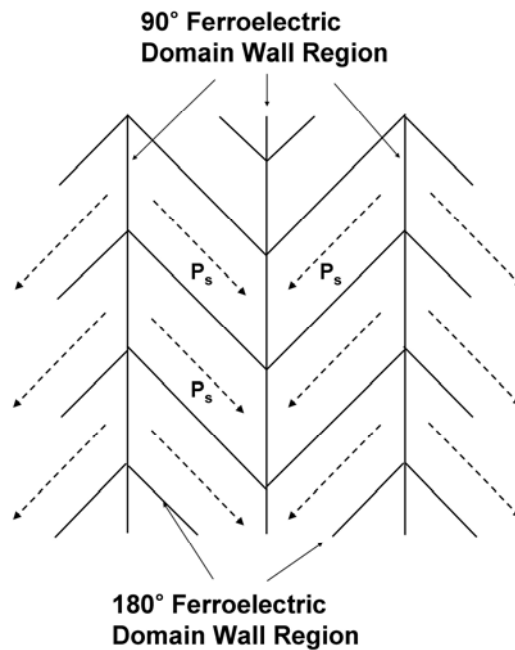


Fig. 2.5 Schematic diagram of 180° and 90° domain walls

The creation of the domains and domain walls are known by the reduction of the total free energy of the material [80, 81]. As for the total energy reduction, the depolarizing energy and elastic energy in the material are the two factors to be considered. The depolarizing energy arises from a non-homogeneous distribution of the spontaneous polarization at the crystal surface, and it has a field direction opposite to that of the spontaneous polarization. There are two ways to reduce the depolarizing energy - domain creation and compensation by electrical conduction [82]. Domains can also be created to reduce the elastic energy from the mechanical restriction of the crystal. In the tetragonal structure, there may be two areas separated by the polarization direction antiparallel or perpendicular to each other, and these are referred to the 180° and 90° domain walls, respectively [82]. Both 180° and 90° domain walls can reduce the depolarizing electric field, while only 90° domain walls may reduce the elastic energy. The schematic diagram of both 180° and 90° domains are shown in fig. 2.5. In the case of the rhombohedral structure, shown in fig. 2.4, the spontaneous polarization direction is diagonal in the eight $\langle 111 \rangle$ directions which provides 180° , 71° , and 109° domain walls.

When the tetragonal structure is deformed, both 180° and 90° domains can be created, while 71° and 109° domain walls can be produced by the deformation of the rhombohedral structure of PZT. 180° domains can reduce the electrostatic energy at the

surface, but non-180° domains can reduce both electrostatic and elastic energies due to their different spontaneous strain directions. Thus, the piezoelectric property of ferroelectric materials is greatly affected by the motion of the non-180° domain walls [83], which is called the extrinsic contribution. The intrinsic contribution to piezoelectricity is the accumulative strain by the polarization reversal from each domain.

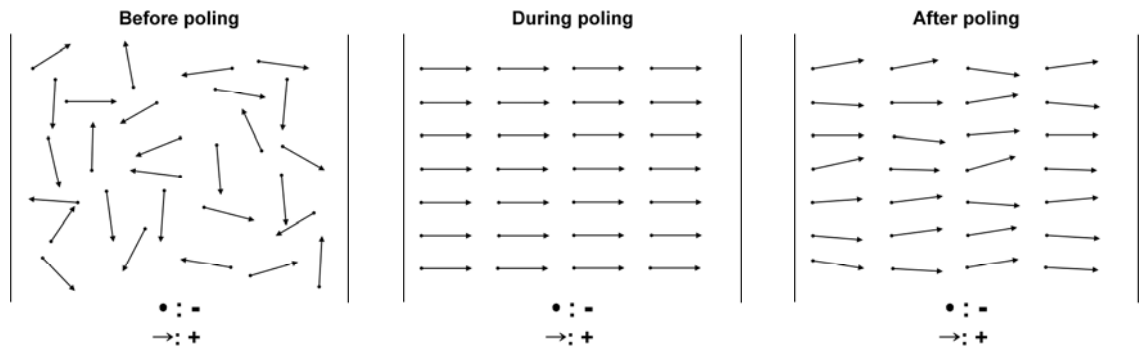


Fig. 2.6 Schematic diagram of poling effect on the electric dipoles

Under a weak and modest electric field, the extrinsic contribution is one of the most important factors to the properties of the ferroelectric material. In the case of the tetragonal structure of PZT oriented in $\langle 100 \rangle$ direction, which generally has 90° domains walls, the motion of a 90° domain wall would be restricted by the ferroelastic effect. This is because much higher energy is needed for 90° domain switching due to the atom movement needed to switch from an a-axis to a c-axis oriented domain [84]. Thus, under

a weak and modest electric field, 90° domain switching may not be active.

In its as-fabricated state, a ferroelectric film may not exhibit ferroelectric behavior, even though it has spontaneous polarization. This is because the electric dipoles are randomly oriented in the PZT film, resulting in an absence of the piezoelectric property due to the zero net polarization, even though each individual grain might be strongly piezoelectric. To achieve the piezoelectric property in PZT films, the electric dipoles should be aligned in one direction [19]. This is done by poling the film, which is usually accomplished by applying an electric field to the films in a range of 2 ~ 10KV/mm at an elevated temperature. The poling effect is shown in fig. 2.6. In the poling process, the random domains are aligned in the direction of the applied electric field by switching the polar axes to the direction which is nearest to that of the electric field and is allowed by crystal symmetry. Once the PZT has been poled, it has a net dipole moment in the crystal and can respond to the external electric field and to the mechanical stress and strain. When the poled PZT is under an electric field that is well below what is needed to switch the polar axis in the crystal, the domains increase their alignment in proportion to the applied voltage, which results in a dimensional change in the film that is linearly proportional to the electric field. When the applied electric field or stress in a direction other than that of the poling direction is high enough, the polar axes of the crystallites

will be realigned due to ferroelectric switching, and nonlinear electromechanical behavior will occur.

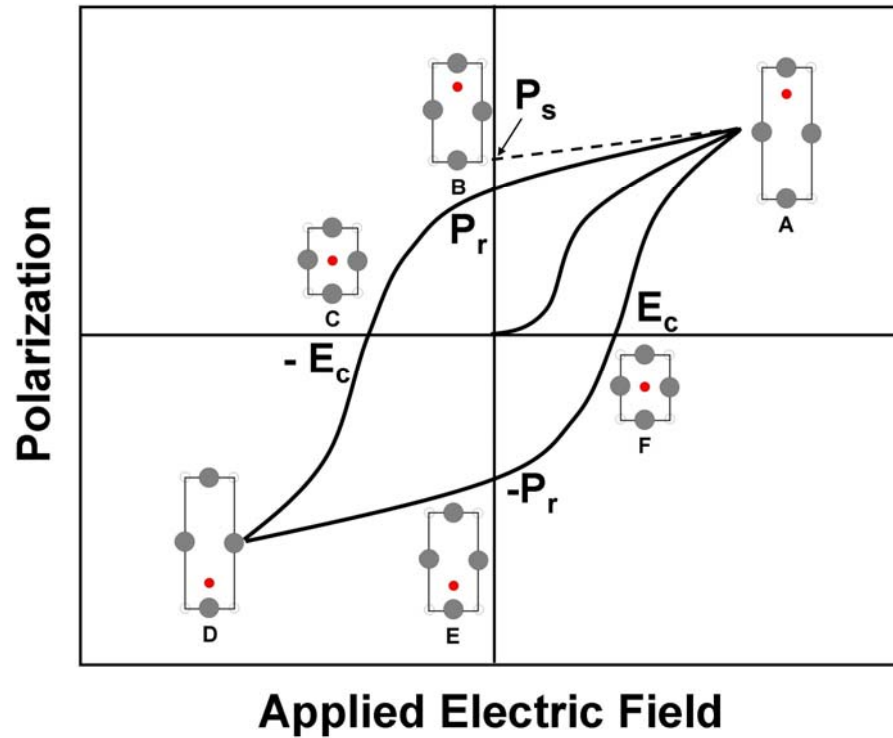


Fig. 2.7 Typical hysteresis loop of ferroelectric materials with schematic diagram of crystal lattice cell

The polarization switching process of ferroelectric materials can be characterized by the hysteresis loop, which shows the nonlinear behavior of the materials due to the domain wall movement. A typical hysteresis loop is shown in fig. 2.7. Even though there is a report [85] that domain switching is actually composed of a two-step process, where 90° domains switch sequentially as opposed to the direct switching of 180° domains, the

figure shows only a simple switching process. Initially, the polarization increases linearly with the electric field. At this stage, the polarizations of the domains start to switch according to the field direction. By increasing the field strength (from zero), the polarization reaches point A, which shows a maximum polarization in the unit cell by a maximum Ti ion displacement. The intercept of the tangential line from point A on the polarization axis is defined as the spontaneous polarization (P_s). When the field is decreased, the polarization decreases. At point B, when the field reaches zero, the polarization will not be zero, and this is defined as the remanent polarization (P_r). Thus, the remanent polarization can be considered as the amount of polarization remaining after removal of the electric field and as the degree of the dipole moment alignment in the ferroelectric material. For the polarization to be zero, a reversed electric field is necessary, and the point at which the polarization becomes zero again is defined as the coercive field (E_c), which can be considered as the amount of electric field needed for polarization reversal. As magnitude of the reverse field is increased, the polarization reaches another maximum in the opposite direction at point D. After that, if the field is again reversed, the polarization can be brought back to the previous maximum point depending on the field strength. Ideally, the positive and negative coercive fields have the same magnitude, as do the positive and negative remanent polarizations. The shape of the loop can be

affected by many factors, such as the presence of defects, film thickness, and heat treatment of the film during fabrication. These factors may also affect the coercive strength and the magnitude of the polarization as well [82].

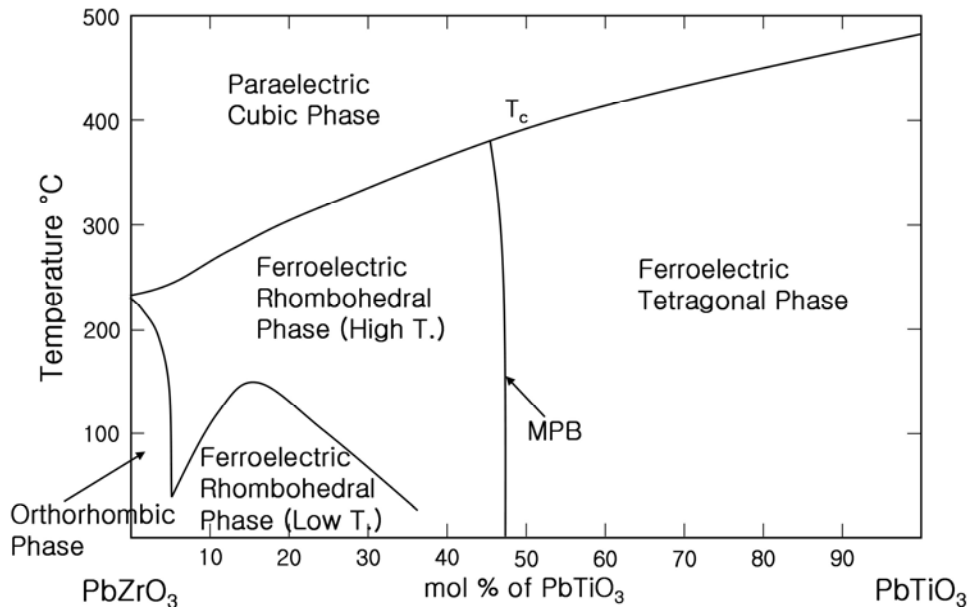


Fig. 2.8 Phase diagram of PbZrO_3 – PbTiO_3 compounds

Because PZT [$\text{Pb}(\text{Zr},\text{Ti})\text{O}_3$], a solid solution of PbZrO_3 and PbTiO_3 , becomes paraelectric cubic beyond the Curie temperature, the Curie temperature is one of the important factors that can determine a limit for device performance in terms of operating temperature. From the phase diagram of PbZrO_3 – PbTiO_3 , shown in fig. 2.8, it is found that, depending on the relative composition of Zr and Ti, PZT can be transformed to a

rhombohedral or tetragonal structure, and the Curie temperature can be range from 230°C to 490°C. The phase boundary around the Zr/Ti composition of 0.52/0.48 is called the morphotropic phase boundary (MPB), and is sensitive to the composition, but not to temperature variation. It has been found that, at the MPB composition, there exists a very large dielectric constant and piezoelectric property, due to the availability of six $\langle 100 \rangle$ polarization directions in the tetragonal structure and eight $\langle 111 \rangle$ directions in the rhombohedral structure. Thus, the MPB composition is desired for the optimum performance of MEMS devices.

2.2 Piezoelectric property

2.2.1 Piezoelectricity

The word *piezo*, comes from the Greek word *piezein*, meaning ‘pressure’. Thus, ‘piezoelectric’ means ‘pressure electric’. The mechanical stress applied to the material can induce polarization in the materials and produce an electric voltage [79]. Thus, the piezoelectric property indicates the ability of materials to produce an electric charge proportional to an applied mechanical stress, which exists in insulators. The criterion to

determine if a material has the piezoelectric effect is a center of symmetry in the crystal structure. If the material has a center of symmetry, then a uniform stress cannot separate the center of gravity of the negative charges and the positive charges, and thus it cannot produce an induced dipole moment necessary for that material to exhibit the piezoelectric effect. If there is no center of symmetry in a material's crystal structure, then it is piezoelectric (with one exception, as discussed below). When an applied stress produces an electric voltage across a material, it is called 'direct' piezoelectricity, and if an applied electric voltage induces a stress in the material, it is called 'converse' piezoelectricity. By considering the crystal symmetry, there are 230 space groups, which can be classified into 32 point groups. Among the 32 point groups of all crystals, 20 of the 21 groups which lack a center of symmetry show piezoelectricity, and one of them (432 point group) does not show the piezoelectric effect due to the presence of other mutual symmetry elements. With the further classification of the crystal symmetry, 10 point groups of the 20 piezoelectric crystal symmetric groups have a unique polar axis and can develop a spontaneous polarization under heating, which is characterized as the pyroelectric effect. Among these 10 groups, the ferroelectric effect occurs only in the 10 subgroups of the pyroelectric crystal symmetric groups, which can be defined by spontaneous and reversible polarization. Therefore, the ferroelectric effect can be

obtained only in the materials which have all three attributes of non-centrosymmetry structure, spontaneous polarization, and reversible polarization. Reversible polarization distinguishes the ferroelectric effect from the piezoelectric and pyroelectric effects. For example, ZnO is a piezoelectric material, but not a ferroelectric material, due to a lack of a spontaneous and reversible polarization. There is another effect, which should be distinguished from the piezoelectric effect, called the electrostrictive effect. The electrostrictive effect is another shape change effect that occurs as the dielectric materials are subjected to an electric voltage. The main difference between the piezoelectric effect and the electrostrictive effect is the reversibility of the strain. When a piezoelectric material is under a reversed electric voltage, the corresponding strain is reversed as well; while in the electrostrictive effect, the corresponding strain is not reversed when the reversed electric voltage is applied to the material. Moreover, the strain due to the electrostrictive effect occurs to some degree in all materials and is usually negligible, while the strain due to the piezoelectric effect is relatively large. The strain/displacement of materials under an applied electric field is shown in fig. 2.9. The displacement of the piezoelectric material is directly proportional to the electric field, while ferroelectric materials show a response in a 'butterfly' shape. Ferroelectric materials can exhibit a

piezoelectric effect, because domain orientation by an electric field in the poling direction produces a piezoelectric response in the material.

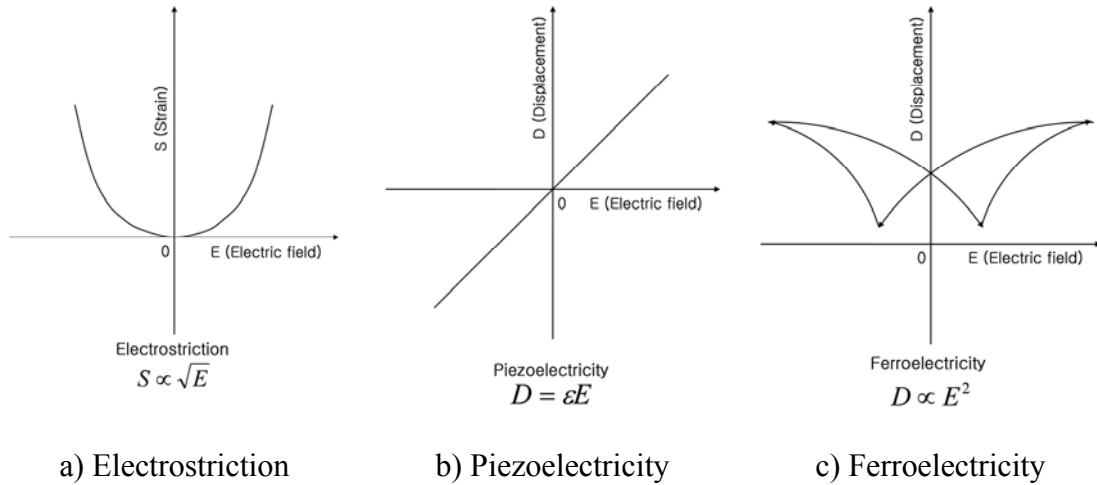


Fig. 2.9 Displacement graphs in respect to electric field

In this study, ZnO and PZT films were used, with ZnO as the piezoelectric material and PZT as the ferroelectric material. For the acoustic wave device application, the materials are under a time-varying electric field during their operation. Due to the ferroelectric polarity in PZT films, the displacement of these films is quite different than ZnO films under the same time-varying electric field, as shown in fig. 2.10. In the case of the piezoelectric material, the displacement is varying directly with the time-varying electric field. The ferroelectric material, however, has a positive displacement regardless

of the direction of the electric field, because the displacement of the material is in proportion to the square of the electric field.

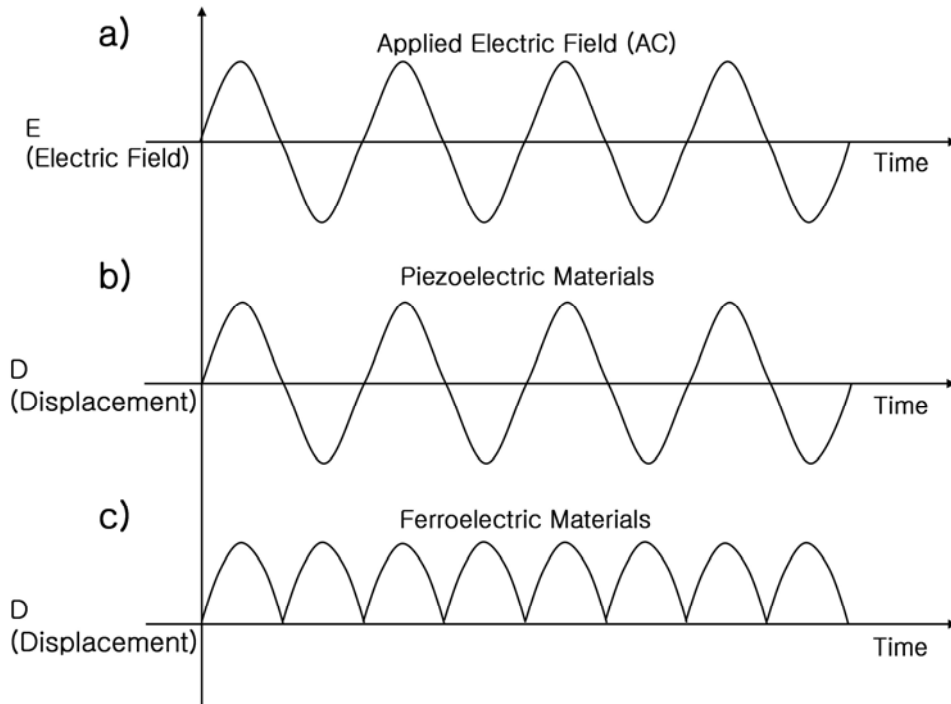


Fig. 2.10 The response of the materials, b) piezoelectric and c) ferroelectric in terms of time according to the applied electric field a)

The interaction between the properties of materials can be described by constitutive equations. For example, the constitutive equation to describe the relation between the electric field and the displacement in isotropic materials is:

$$D = \epsilon E \dots\dots\dots(2.1)$$

where, D and E are the displacement and the electric field, respectively. ϵ is the permittivity, and is expressed by $\epsilon = \epsilon_0(1 + \chi)$, where, ϵ_0 and χ is the permittivity in vacuum and the dielectric susceptibility, respectively. The permittivity ϵ is commonly expressed by the relative value to the permittivity in a vacuum ϵ_0 , and the dielectric constant is $K = \epsilon/\epsilon_0$. As well, the constitutive relation between the stress σ and strain S is:

$$\sigma = cS \dots\dots\dots(2.2)$$

The constant of the relationship c is called the stiffness coefficient, which has a unit of N/m^2 . For reference, there is another proportional constant between the stress and the strain.

$$S = y\sigma \dots\dots\dots(2.3)$$

The equation (2.3) has a proportional constant of the elastic compliance coefficient y , which has a unit of m^2/N . Comparing the units of the coefficients, the relationship between the coefficients can be expressed as $y = 1/c$.

For the piezoelectric materials, the constitutive equations need to consider additional terms, due to their anisotropic characteristics. Because the properties of the piezoelectric materials are commonly dependent on the crystal orientation, tensors should be utilized to describe material properties according to the crystal orientation. Furthermore, because of the coupling between the strain and the electric field in piezoelectric materials, the constitutive equations, (2.1) to (2.3) of non-piezoelectric materials should be modified with the coupling effect.

$$D_i = \varepsilon_{ij}^S E_j + f_{ijk} S_{jk} \dots\dots\dots (2.4)$$

$$(i, j, k = 1, 2, 3)$$

$$\sigma_{ij} = c_{ijkl}^E S_{kl} - g_{ijk} E_k \dots\dots\dots (2.5)$$

$$(i, j, k, l = 1, 2, 3)$$

$$S_{ij} = y_{ijkl}^E \sigma_{kl} + g_{t_{ijk}} E_k \dots\dots\dots (2.6)$$

$$(i, j, k, l = 1, 2, 3)$$

f and g are the piezoelectric stress constant and the piezoelectric strain constant, respectively, and they are third rank tensors. f has a unit of C/m² or N/Vm and g has a unit of C/N or m/V. The transposed piezoelectric strain constant g_t can be identified by interchanging the rows and columns in the matrix. The equations of (2.4) to (2.6) are known as the piezoelectric constitutive relations. From the equations, it is found that the dielectric constant and the elastic constant of the materials have a large effect on the piezoelectric constants and, hence, play an important role in device performance, because the strains induced by the electric field increase as the magnitude of the piezoelectric constants increases. In device performance, high piezoelectric constants can indicate low conversion loss [86]. There can be additional piezoelectric constants depending on the crystal symmetry and, in general, when there is a higher degree of symmetry, the possible number of piezoelectric constants decreases. A crystal with no symmetry can have 18 piezoelectric constants to fully describe its piezoelectric property, while in the case of a cubic crystal, which is the most symmetrical type of crystal, there is only 1 piezoelectric constant. Additionally, the constitutive equations can completely describe the relations between the stress, strain and electric field; the relations between the mechanical variables and the electrical variables are shown fig. 2.11.

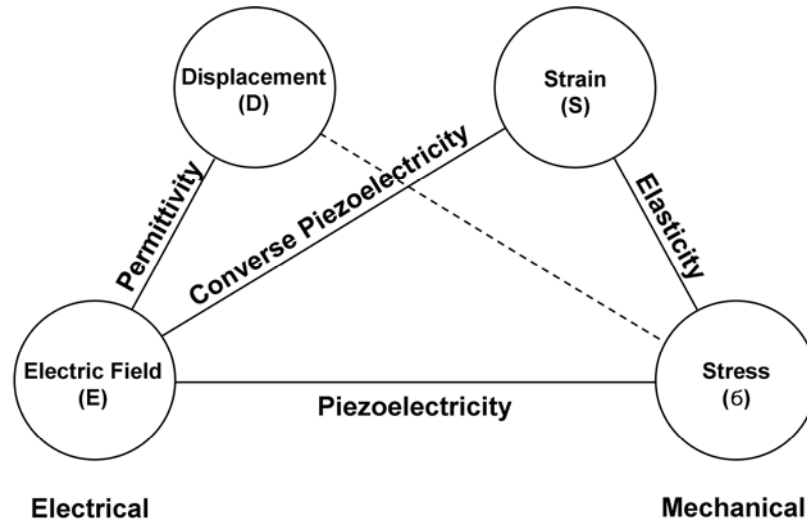


Fig. 2.11 Relations between electrical and mechanical variables

PZT film is a ferroelectric material that has both high dielectric and piezoelectric constants, and so will produce a large strain under an applied electric field. However, due to its ferroelectric piezoelectric property, this material behaves in a nonlinear fashion, which results in the differential form of the equations.

$$\delta D_i = \epsilon_{ij}^S \delta E_j + f_{ijk} \delta S_{jk} \dots\dots\dots (2.7)$$

$$(i, j, k = 1, 2, 3)$$

and

$$\delta \sigma_{ij} = c_{ijkl}^E \delta S_{kl} - g_{ijk} \delta E_k \dots\dots\dots (2.8)$$

$$(i, j, k, l = 1, 2, 3)$$

and

$$\delta S_{ij} = y_{ijkl}^E \delta \sigma_{kl} + g_{ijk} \delta E_k \dots\dots\dots (2.9)$$

$$(i, j, k, l = 1, 2, 3)$$

2.2.2 Electromechanical coupling coefficient

The degree of the piezoelectric property can be readily specified by considering the electromechanical coupling coefficient k^2 , which makes the estimation of the efficiency of the materials possible, because the coefficient is a measure of the ability of piezoelectric transducers to convert electrical energy to mechanical energy, or vice versa.

$$k^2 = \frac{\text{Mechanical (or electrical) energy converted to electrical (or mechanical) energy}}{\text{Mechanical (or electrical) energy put into transducer}}$$

If the coefficient reaches the value of 1 (i.e. 100% efficiency), then that material could be considered to be ideal for MEMS applications, because the input energy can be completely converted to the output energy. The electromechanical coupling coefficient of ZnO is ~7.8%, and for PZT is ~20.25% [6], and these values represent the theoretical

energy conversion ratio. However, if the transducer is not properly tuned (i.e., not operating at its resonance frequency) then the actual efficiency will be lower than these values.

2.3 Acoustic Wave Devices and FPW Device

2.3.1 Acoustic Wave Devices

Acoustic sensing is only possible when the properties of the film are affected by an acoustic wave, such that the film will transduce any physical signal to an electrical signal, or vice versa, in response to the species to be detected. Acoustic wave device sensors are classified into four categories, including thickness shear mode (TSM), surface acoustic wave (SAW), acoustic plate mode (APM), and flexural plate wave (FPW) sensors. A distinction among these acoustic wave devices is how the type of acoustic wave is electronically excited, which can be determined by the crystal orientation, the film thickness, and the geometry of the interdigital transducer (IDT). When the acoustic wave device is sensing the disturbances caused by the measurands (e.g. mass), there is a corresponding change in the oscillation frequency and amplitude of the acoustic wave

due to the change in acoustic wave phase velocity [87], as shown in fig. 2.12. The frequency change is caused by the change in mass attached to the device surface, and the amplitude change by the attenuation due to the acoustic energy dissipated into the measurands. In an acoustic wave device, the sensitivity according to frequency change by mass loading can be expressed as [88]:

$$S_m = \frac{1}{f_0} \frac{df}{dm} \dots\dots\dots(2.10)$$

where, f_0 and f are the frequencies for the unperturbed and perturbed cases, respectively, and m is the mass. From this equation, we can determine the equation for the minimum detectable mass density (MDMD) according to the frequency change:

$$\Delta m_{\min} = \frac{1}{S_m} \frac{\Delta f_{\min}}{f_0} \dots\dots\dots(2.11)$$

When $\Delta f/f = \Delta v/v$ [89] is applied to equation (2.11), then, equation (2.11) becomes

$$\Delta m_{\min} = \frac{1}{S_m} \frac{\Delta v_{\min}}{v_0} \dots\dots\dots(2.12)$$

Δv is the change in the wave velocity, and v_0 is the wave velocity in the unperturbed case.

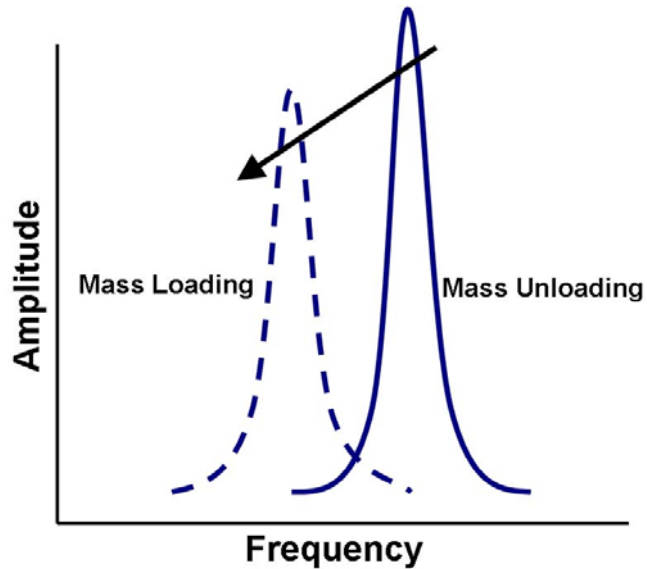


Fig. 2.12 Frequency and amplitude changes by measurands

2.3.2 FPW Device

Much attention has been paid to the FPW device in chemical and biological sensor applications because of its unique properties. FPW devices have a lot of potential for use with various types of measurands, such as vapor and liquid, because the electric circuit of the device can be isolated from the measurands [86, 87]. Additionally, due to low damping in a liquid medium [89], these devices have a great advantage in biological

and chemical sensing applications. Due to their thin membranes, FPW devices have a low operating frequency, resulting in high sensitivity. FPW devices also have low fabrication costs because they can be simply fabricated on silicon wafers by micromachining techniques.

The acoustic wave, also called a Lamb wave (named after Horace Lamb [90]), can propagate in the thin membrane of an FPW device, which has two IDT ports for input and output of the electric signal to launch and receive the acoustic wave. As shown in fig. 2.13, the acoustic wave in the thin membrane has a particle displacement in a retrograde elliptical shape, which has two components, surface normal and surface parallel, similar to a Rayleigh wave in SAW. One of the advantages of an FPW device for use in liquid environments is that it has low damping when immersed in liquid, although it has a surface normal component in the propagating wave. This is one of the unique characteristics of FPW devices that is different from SAW. It is a result of the thin membrane, which produces a low acoustic wave velocity and a low resonance frequency. When the acoustic wave is propagating in liquid, with a velocity that is equal to or less than the compression wave in liquid medium, there is low loss in the acoustic wave energy, resulting in low attenuation. Typical resonance frequency of an FPW device is 2 to 7 MHz, and the sensitivity can be stated as $S_m = -1/2M = -1/2\rho d$, where, M is the

mass per unit area, and ρ and d are the density and the thickness, respectively. Different from the other acoustic sensors, which have a higher mass sensitivity with increasing membrane thickness, the sensitivity of the FPW device increases as the thickness of the membrane is decreased.

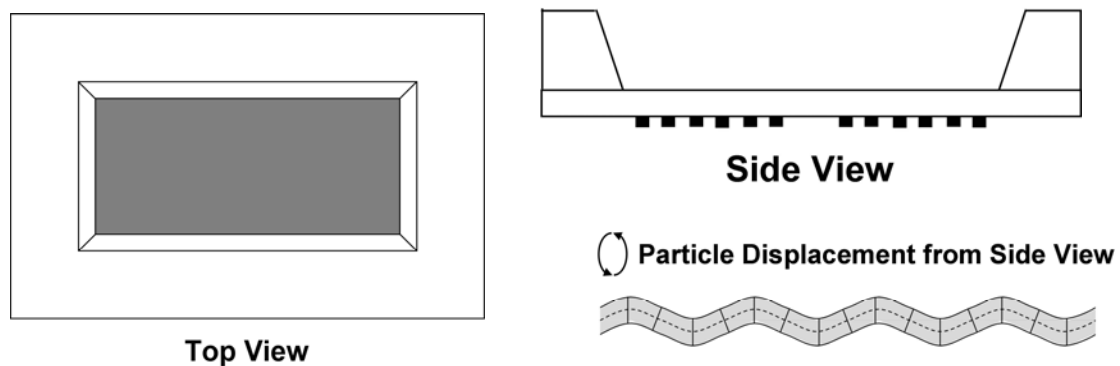


Fig. 2.13 Top, side and particle displacement of FPW device

In addition to the sensor applications, FPW devices can have actuator applications, such as a micro pump [91, 92], and a microfilter. ZnO films have been commonly used for FPW device fabrication for both sensor and actuator applications. The FPW device has some advantages as a micromotor, such as the isolation of the electric circuit from any fluidic medium to prevent a short-circuit, low driving voltage, the possibility of linear motion, and the relatively large surface motion of the membrane of the device [93, 94]. This relatively large surface motion results from the relatively

large amount of the acoustic energy resulting from the energy confinement in the plate, and has been reported for 10nm [95] and 27.5nm [96] FPW membranes composed of ZnO films. As a microfilter, the ZnO film FPW device also has the advantage of a self-cleaning mechanism, which can lessen the filter fouling, and increase filtering volume and device life time [97]. However, for the actuator application, mainly PZT films have been used [98], because they possess higher displacement of the membrane due to high piezoelectric and dielectric constants. This can produce higher wave amplitude and pumping speeds [93], providing higher energy to transport the particle. The higher displacement of PZT films also results from the higher dielectric and piezoelectric constants compared with those of ZnO films. The flow rates of a PZT FPW device were measured to be 0.255 μ l/min [99] and 0.25 μ l/min [100, 101].

CHAPTER 3

ZNO FILMS BY CHEMICAL SOLUTION DEPOSITION (CSD)

3.1 Introduction

Zinc oxide (ZnO) films have attracted much attention because of their unique physical properties, such as transparency in the 0.4 ~ 2 μm optical wavelength range, as well as their fairly good piezoelectric, elasto-optic, electro-optic, and nonlinear optical coefficients. Additionally, they are very stable chemically in reducing environments, non-toxic, and the material itself is widely accessible [55]. Currently, ZnO is being intensively investigated for potential applications including transparent conductive films [102, 103], solar cells [52], sensors [104], optical devices [22], low voltage varistors [105], and acoustic wave devices [106, 107]. In particular, the acoustic wave device application requires ZnO films with a high electromechanical coupling coefficient, temperature stability, high electrical resistivity, and strong *c*-axis orientation. Since the degree of *c*-axis orientation of the films correlates directly with electromechanical coupling, control

of the preferred orientation has been a research focus. To obtain high quality ZnO films, a variety of techniques have been employed such as sputtering [106, 108], chemical vapor deposition [25, 107, 109], pulsed laser deposition [110] and chemical solution deposition [35, 104, 111-114]. Among various deposition techniques, the chemical solution deposition (CSD) method (e.g. the sol-gel process) offers several advantages, such as excellent compositional flexibility, easy control of film thickness, and easy fabrication of a large-area thin film with low cost. There have been reports on the chemical solution deposition of ZnO films. Parameters in the CSD process, such as solution chemistry [114, 115], heat treatment condition [116], and substrate type [117] were reported to affect the crystallization behavior and preferred orientation of ZnO films. Since pyrolyzed films are typically amorphous, film crystallization in solution derived thin films occurs by a nucleation and growth process. Therefore, the substrate, *i.e.* the interface between film and substrate can play an important role in the growth of oriented films. Most studies of crystallization and orientation in CSD ZnO films, however, have focused on films on glass substrates, which limits understanding of the crystallographic relationship between solution derived ZnO films and crystalline substrates during the CSD process.

In this chapter, the crystallization and orientation of CSD ZnO films are studied on different types of silicon-based substrates. Silicon nitride grown on silicon substrates

and platinum coated silicon substrates are prepared to study the effect of substrate crystallinity. Platinum coated silicon substrates having two different orientations are used to investigate the effect of lattice matching between ZnO film and the substrate.

3.2 Detailed Experiment

In CSD, the properties of ZnO films are greatly dependent on the process parameters, such as pyrolysis and annealing temperatures, substrates, and solution chemistry, including solvents and additives. Zinc acetate dehydrate ($\text{Zn}(\text{CH}_3\text{COO})_2 \cdot 2\text{H}_2\text{O}$, Aldrich) and 2-MOE (2-methoxyethanol, $\text{CH}_3\text{OCH}_2\text{CH}_2\text{OH}$, Aldrich) were used as a zinc source and a solvent, respectively. 200°C, 300°C, and 400°C were used for pyrolysis temperatures, and 500°C, 600°C, and 700°C for annealing temperatures. Due to the stability of the solution against the humidity from the surroundings and the increase of the solubility of the solute to the solvent [114, 118], chelating agents are needed as an additive. Additionally, a chelating agent can increase solubility of zinc alkoxide, which is one of major problems with this method [119]. In this experiment, DEA (Diethanolamine, $\text{HN}(\text{CH}_2\text{CH}_2\text{OH})_2$, Aldrich) and MEA (Monoethanolamine, $\text{NH}_2\text{CH}_2\text{CH}_2\text{OH}$, Aldrich) were chosen as chelating agents. Pt(111)- and Pt(200)- layered silicon wafers were the

substrates for characterizing the film on the crystalline substrates with different surface configurations. Amorphous silicon nitride (SiN_x -) and silicon oxide (SiO_x -) layered silicon wafers were used for characterizing the film properties on amorphous substrates. The precursor solution consisted of zinc acetate dehydrate, 2-MOE, and the chelating agent. All chemicals were mixed, stirred at 80°C for 1 hour, then cooled to room temperature, and aged for at least 72 hours. The aged solution was applied to the substrates such that all of the substrate surfaces were covered, and then spin-coated at 3000rpm for 30 seconds. The solution concentrations used were 0.1M, 0.3M, 0.5M, and 0.7M. The thickness, depending on the molar concentration of the precursors, was measured as 5nm, 15 nm, 28nm, and 35nm per each layer. For the heat treatment of each coating, pyrolysis was performed for 10min. After 5 coatings, the pyrolyzed films were put into the furnace set to the annealing temperature for 1 hour for crystallization. For thicker films, after every 5 coatings, additional heat treatment at the annealing temperature was performed for 10min, and after the desired thickness, a final annealing step was performed for 1 hour. The schematic diagram of the experimental procedure for the fabrication of ZnO films with 0.7M DEA- and MEA- chelated solution to reach 700nm with 20 layers is shown in fig. 3.1.

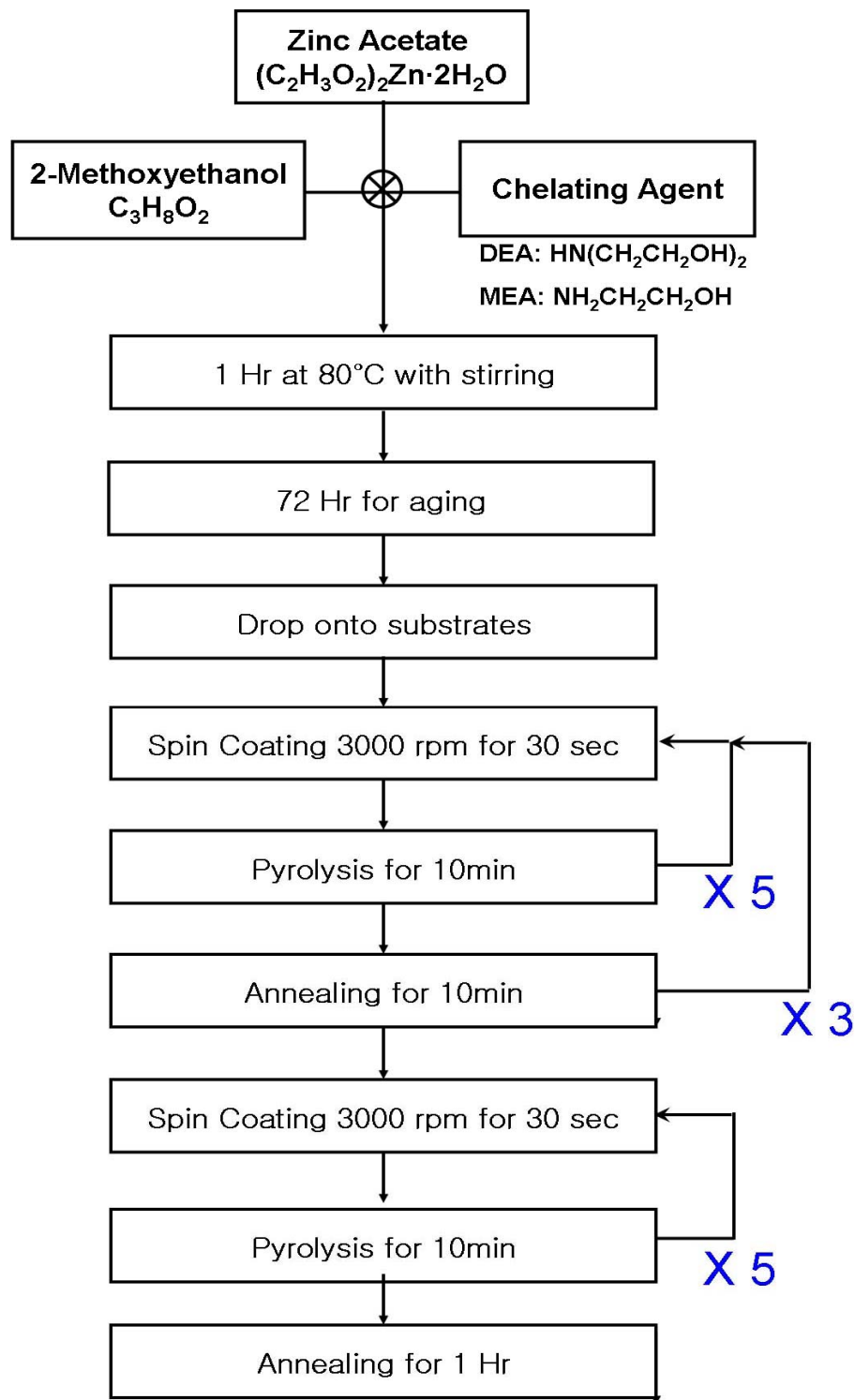


Fig. 3.1 Experimental procedure of ZnO film fabrication by sol-gel method, which shows 20 coatings to reach over 600nm thickness with 0.7M solution

Film crystallinity and orientation were assessed by X-ray diffraction (Rigaku D/MAX B) utilizing $\text{CuK}\alpha$ radiation. The scan range was 20° to 80° in 2 theta angle measurements. The operating condition of XRD was 40KV and 40mA. Scan speed was 5° per min in 2 theta angle measurements, and the scan step was 0.05° . A monochromatic filter was used for the x-ray measurement. However, for the detailed investigation of the XRD peaks, only the angle range desired to be investigated was chosen as XRD data. The thermal properties of the gel powders were analyzed using differential scanning calorimeter/thermo-gravimetric analysis (DSC/TG, Rheometric Scientific STA1500), with a heating rate of $10^\circ\text{C}/\text{min}$. The precursors, previously aged for 72 hours, were heated up to 100°C and kept for over 24 hours. The heating range was RT to 750°C . Since FTIR (Fourier Transform Infra-Red spectroscopy) provides a fingerprint of the chemical presence in a solution, the chemical bonding in the precursor can be indentified using an FTIR (Perkin Elmer 2000) measurement with a frequency range between 400cm^{-1} and 4000cm^{-1} . The surface morphology and roughness of the films were characterized by scanning electron microscope (SEM, JEOL JSM-7000F) and scanning probe microscope (SPM, JEOL JSM-700F). Raman spectroscopy was also applied to the samples, because it can offer a fast and simple technique to provide the film orientation and crystallinity. For the Raman experiment, an He-Cd laser (Kimmon Electric) with 441.6nm of

wavelength was used. The nominal power of the laser beam was 80mW. Optical microscopy (Zeiss AxioTech) was used to focus a spot of about 5 μ m in diameter. A thermoelectrically cooled charged coupled device (CCD) was used as a detector. Backscattering geometry was used and the polarization state of the laser beam was not analyzed for the incident and scattered light. Spectral resolution of the grating used was about 0.2cm⁻¹.

3.3 Parametric Study of Precursors

The properties of ZnO films derived by the CSD method depend greatly on the process parameters. Among these, the substrate type, the heat treatment, and the chelating agent effects on the film properties were investigated. The film properties and orientation depend on the solution chemistry, with the solvent and the additives being key variables in CSD film fabrication, although chelating agents have been utilized for solution stability and solute solubility. 2-MOE (Methoxyethanol) was used for the solvent, because a solvent with a low boiling point may hinder the preferred crystal growth [120] due to a lack of structural relaxation [121]. The two chelating agents that were used for ZnO film fabrication were DEA and MEA. The precursors with the DEA and MEA each

were characterized by FTIR to find the bonding characteristics in the solutions, as shown in fig. 3.2.

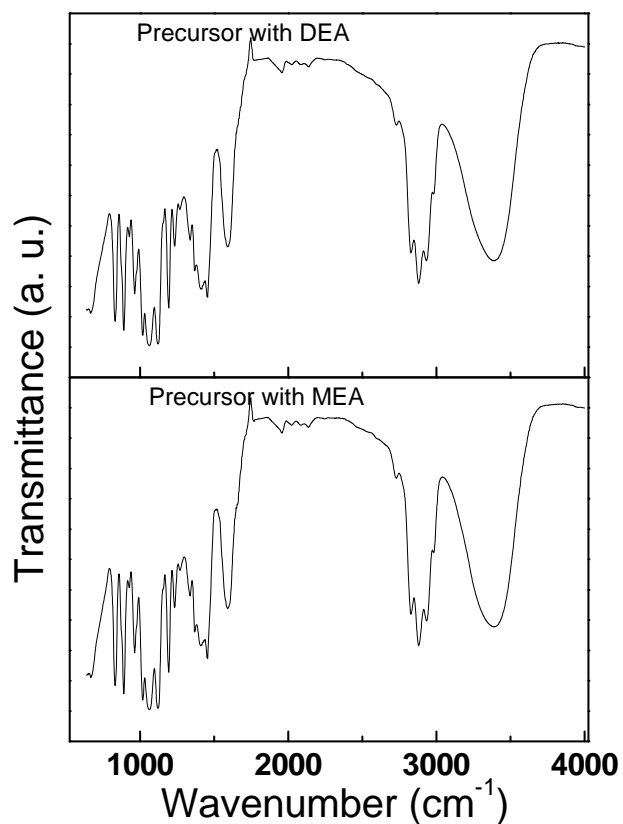
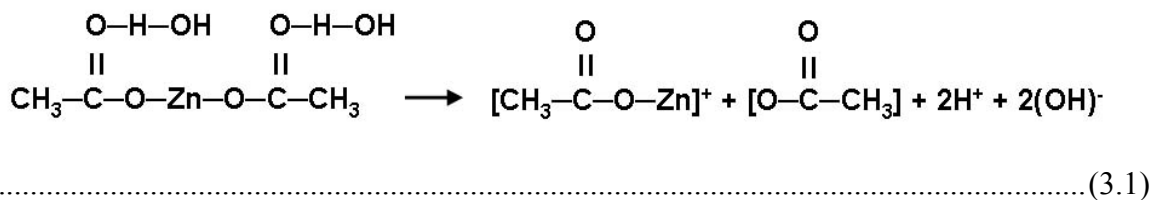


Fig. 3.2 FTIR of the precursor at 0.5M concentration with different chelating agents

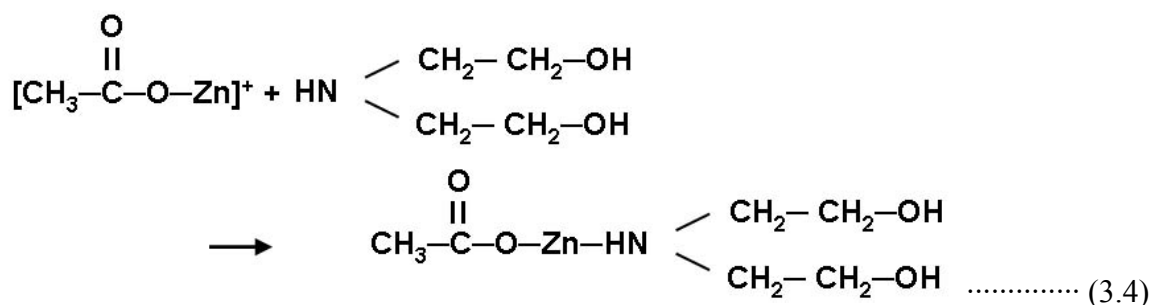
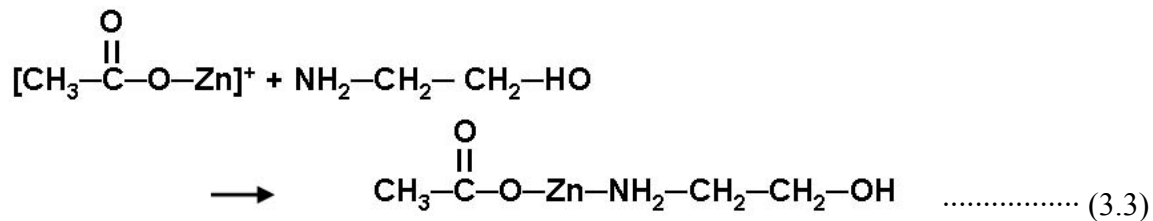
When zinc acetate is immersed into the solvent, 2-MOE, the dissolution of the zinc acetate occurs as follows:



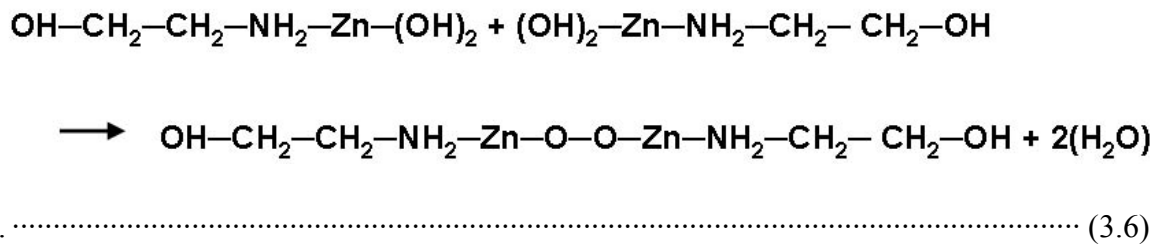
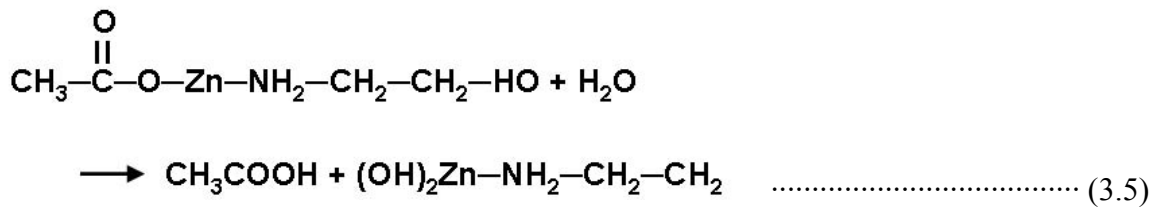
The resulting products are zinc mono-acetate, $[\text{CH}_3\text{-C(=O)-O-Zn}]^+$ [122] and acetic acid as a by-product.



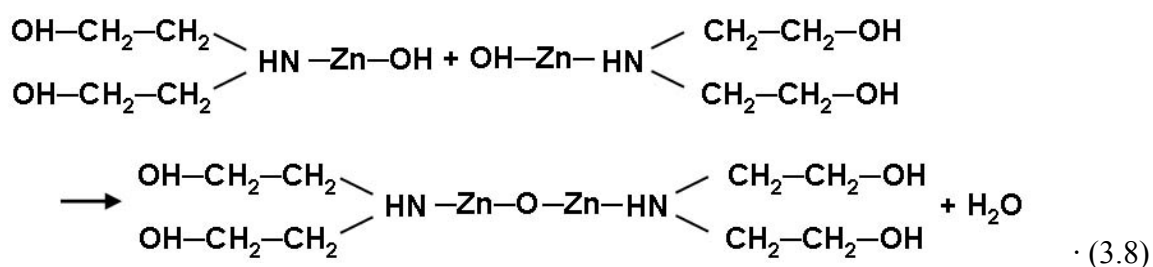
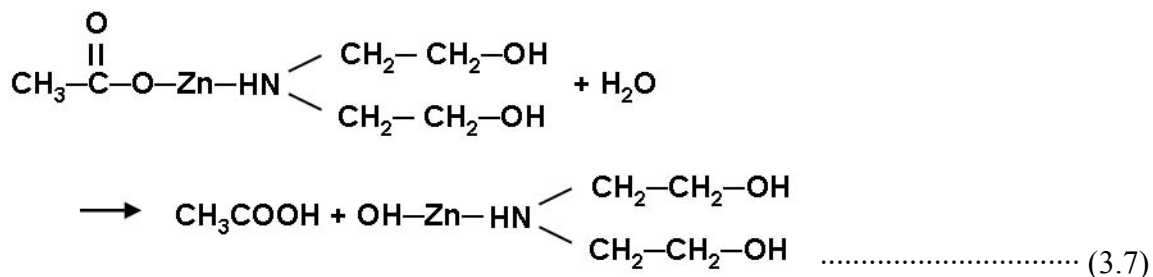
The chelating agents can make complexes with the zinc mono-acetate, which makes the zinc acetate stable against its surroundings.



Eq. (3.3) and (3.4) indicates the chelated complexes with zinc acetate and the chelating agents, MEA and DEA, respectively. Zinc acetate is an ester, and the chemical reactions within the solution can be determined by hydrolysis and condensation, which are fundamental steps in sol-gel deposition method.



Eq. (3.5) and (3.6) are the reactions of hydrolysis and condensation in the precursor chelated with MEA, respectively, and the reactions for the precursor chelated with DEA are shown below:



Eq. (3.7) and (3.8) are the reactions of hydrolysis and condensation in the DEA-chelated precursor.

With these equations, the peaks in the fig. 3.2 can be identified. A frequency of 3400cm^{-1} can be attributed to the O-H stretching vibration in Zinc acetate [123, 124] for both precursors chelated with MEA and DEA. At 2930cm^{-1} and 2879cm^{-1} , the frequencies for asymmetric and symmetric vibrations of C-H bonding, respectively, can be seen in the precursor chelated with MEA [124] and DEA [123, 125, 126]. From the above equations, the acetate group composes the complex with Zinc metal with C-O and C=O stretching bonding, and typically the bonding structures are of the unidentate, bidentate, and bridging types [127]. The frequencies of the different bonding types might

not be able to be resolved because of the small differences between them [128]. However, fig. 3.2 shows the bonding structures in FTIR spectrum. The peaks at 1590cm^{-1} and 1420cm^{-1} indicate the bridging bonding of the asymmetric and symmetric vibration of C=O [115, 125, 128], and the peak at 1454cm^{-1} represents the bidentate bonding of C-O bonding [127] in the zinc mono-acetate complex of both precursors. These peaks confirm that both precursors are chelated by MEA and DEA. The asymmetric CH_2 bonding vibration in MEA and DEA was found at 1454cm^{-1} [126], and the carboxylate group (COO^-) was found at 1407cm^{-1} . Furthermore, the peaks at 1061cm^{-1} and 1018cm^{-1} indicate C-C bonding of zinc acetate [129]. From fig. 3.2, it was found that the precursors chelated with MEA and DEA do not show any difference between them. This may be a reasonable result because both additives have the same amino group (NH) and alcohol group, but in different numbers, which causes the difference in molecular weight.

The crystallinity of ZnO films on crystalline and amorphous surface configurations was determined with XRD data. ZnO films were fabricated with DEA-chelated solution at a 0.1M concentration, and the substrates used were Pt(111)- and Pt(200)-textured-layered and SiN-amorphous-layered silicon wafers. A TG/DSC curve was obtained to determine the heat treatment condition. The result shown in fig. 3.3 was obtained as follows: First, for a background measurement, an empty crucible was placed

onto the chuck, and heated from RT to 650°C. Then, the same kind of crucible was used for each precursor and the experiment was repeated to get the raw data. The raw data was then corrected using the background data from the empty crucible experiment. Then, the final curves of TG and DSC for each solution were determined.

The DSC curve of the MEA chelated precursor in fig. 3.3 a) shows endothermic peaks around 115°C, 235°C, and 305°C, corresponding to the evaporation of water molecules, solvent and acetic acid, and strongly bound organic compounds remaining in the precursor, respectively. Total weight loss of the MEA chelated precursor was about 65%, and most weight loss occurred below 300°C.

In the case of the DEA chelated precursor, peaks of the DSC curve appeared at 130°C, 250°C, and 335°C, which are associated with the evaporation of water, solvents and acetic acid, and other organic compounds, respectively. Total weight loss for this solution was approximately 60% and occurred until 420°C. As seen in fig. 3.3, the precursor chelated with DEA has a higher crystallization temperature than that with MEA, and the precursor chelated with MEA has higher loss in weight than that with DEA. The difference may be caused by the bonding strength between the chelating agents.

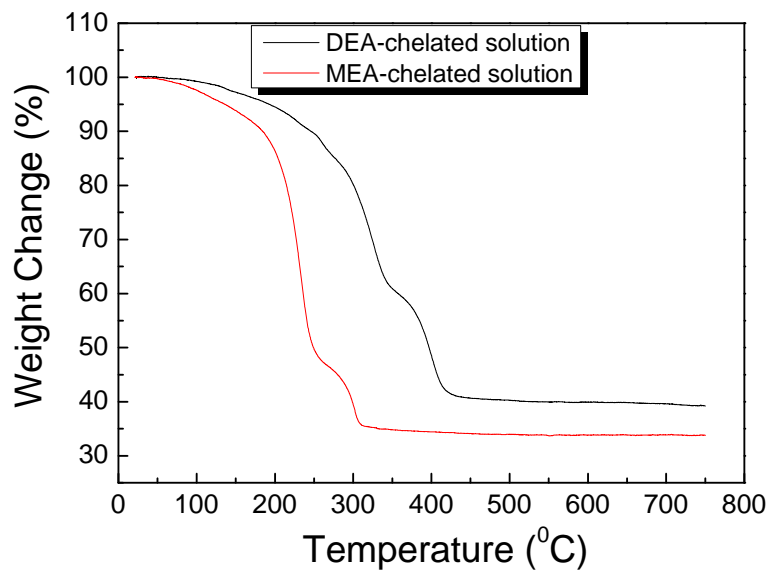
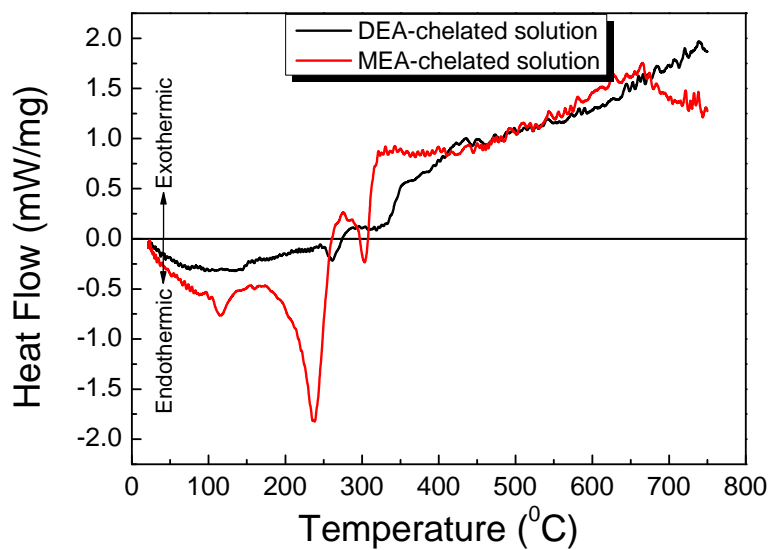


Fig. 3.3 Results of TG/DSC for DEA- and MEA-chelated precursor for the fabrication of ZnO films by Sol-Gel method

- a) DSC graph
- b) TG graph

In the case of DEA, there are two hydroxyl groups in each molecule, while MEA has one hydroxyl group in each molecule. Additionally, DEA has a higher boiling point than MEA (DEA: 270°C and MEA: 170°C), meaning that there is a higher bonding strength in DEA than in MEA. From this data, it was determined that 200°C, 300°C, and 400°C would be the pyrolysis temperatures, and 500°C, 600°C, and 700°C would be the annealing temperatures to evaluate the heat treatment effect on the properties of ZnO films.

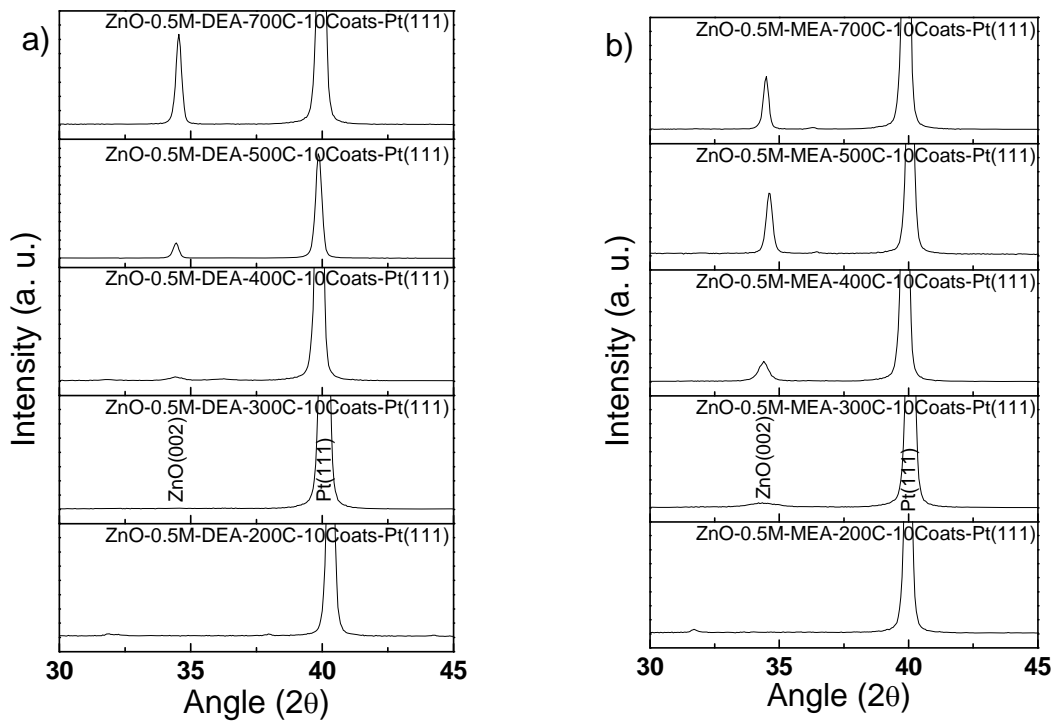


Fig. 3.4 XRD results for DEA- and MEA-chelated precursor for the fabrication of 10 layers of ZnO films by Sol-Gel method on Pt(111) oriented layered silicon wafer from 200 to 700°C temperature range in one step heat treatment scheme

- a) ZnO films with DEA chelated precursor
- b) ZnO films with MEA chelated precursor

The chelating agent effect can be seen in the XRD result of fig. 3.4 as well. The two kinds of precursors, with DEA and MEA separately, were dropped onto Pt(111) oriented layered silicon wafers and put into the furnace, adjusted to the desired temperature. By repeating this process 10 times, 10 layered ZnO films with only a one-step heat treatment were obtained.

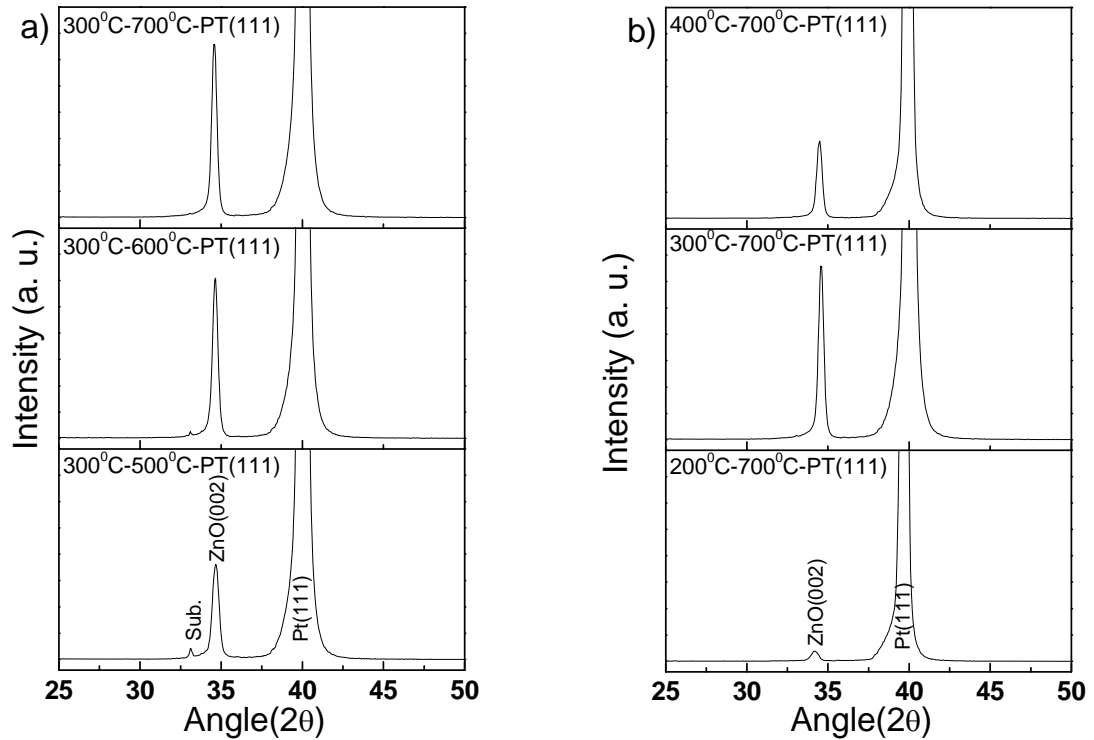


Fig. 3.5 XRD results of 5 coatings ZnO films fabricated by DEA-chelated 0.1M solution concentration with the variation of:
 a) Annealing temperature from 500°C to 700°C
 b) Pyrolysis temperature from 200°C to 400°C

At heat treatments up to 400°C, ZnO films with DEA chelated precursor were not crystallized, as can be seen from the lack of a recognizable peak intensity for ZnO(002). At the 500°C heat treatment, ZnO film derived from the DEA chelated precursor began to crystallize. Comparing fig. 3.4 (a) and (b), those with the MEA chelated precursor started to crystallize at a heat treatment of 400°C. Thus, the precursor chelated with DEA needs higher temperature for film crystallization than that chelated with MEA. Additionally, the effect of heat treatment temperatures was investigated by observing XRD data in detail. All films show a well-crystallized state, even those made with the precursor chelated with DEA, meaning that heat treatment above 500°C can crystallize all of the films, which is in good agreement with the results of the TG/DSC data in fig.3.2.

When the annealing temperature was varied between 500°C and 700°C, as shown in fig. 3.5 (a), it was found that the annealed ZnO film at 700°C showed the highest crystallinity. From the variation of the pyrolysis temperatures between 200°C and 400°C, with the 700°C annealing temperature, the pyrolyzed ZnO film at 300°C exhibited the highest crystallinity. Thus, the optimum condition using DEA-chelated precursor for ZnO film, which should have a strong c-axis textured orientation, was a pyrolysis temperature of 300°C and an annealing temperature of 700°C. Commonly, the solution system for

ZnO film fabrication is composed of the source material, a solvent, and additives. Even though the heat treatment condition will be varied in accordance with which type of chemicals are used, there exists an optimum temperature for each solution system because of the degree of chelating and the boiling points of the chemicals. One of the examples is shown in the study by M. Ohyama [112]. There are three factors used to evaluate the heat treatment condition: the solvent vaporization, the acetate decomposition, and the crystallization of ZnO in the film. If the temperature is below the optimum temperature, and the vaporization and decomposition which was not completed during the pyrolysis step occurs instead at the annealing step over 500°C concurrent with the crystallization, the preferred orientation may be perturbed. If the temperature is over the optimum temperature, then these three factors will occur simultaneously and disturb the preferred orientation. This could be a possible reason for the existence of the optimum temperature.

3.4 Nucleation and Growth Mechanism of CSD ZnO Film

In the CSD method, the substrate is one of the important factors in determining the preferred orientation, because the substrate provides the nucleation site in the film

formation, greatly influencing the film texture. Pt(111)- and Pt(200)-layered silicon wafers and silicon dioxide- and silicon nitride-layered silicon wafers were used as substrates. The Pt(111) and Pt(200) layers represent crystalline surface configuration, while the silicon dioxide and silicon nitride layers represent amorphous surface configuration.

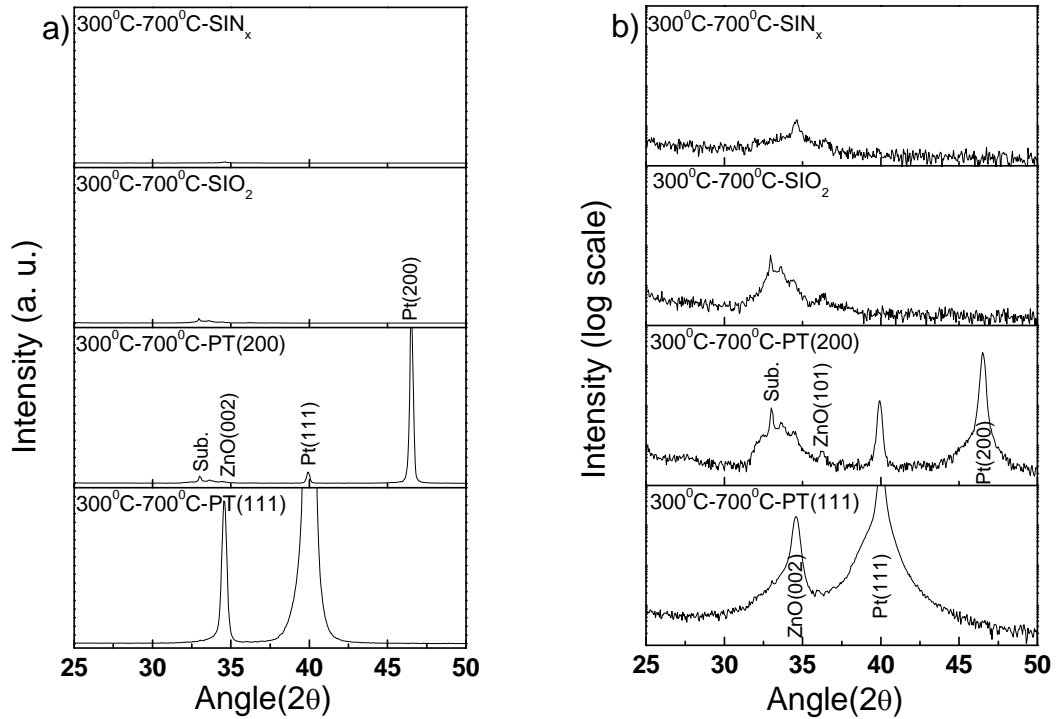


Fig. 3.6 XRD data of 5 coated ZnO films deposited onto various substrates with same heat treatment of 300°C pyrolysis and 700°C annealing condition with DEA chelated solution of 0.1M solution concentration in:

- a) Linear scale
- b) Log scale

Fig. 3.6 shows ZnO films prepared in the identical heat treatment condition of 300°C pyrolysis and 700°C annealing. From fig. 3.6 (a), the ZnO(002) peak was significantly affected by the surface configuration of the substrates. Only the ZnO film on Pt(111) shows strong (002) textured structure, while ZnO films on other substrates show no textured structure. The identity of the ZnO films was able to be recognized using a logarithmic scale (fig. 3.6 b). This substrate dependency of ZnO films was found in other ZnO films heat-treated in different pyrolysis and annealing temperatures. It is believed that the different preferred orientation observed between Pt(111)- and Pt(002)-layered silicon substrates is due to lattice mismatch between the ZnO film and the Pt substrate, which also can influence the growth behavior of ZnO films.

The pyrolyzed ZnO films are amorphous and film crystallization occurs by a nucleation and growth process which is analogous to that used to describe crystallization in traditional glasses. The main driving force for nucleation is related to the reduction of free energy due to a phase transformation from the amorphous to the crystalline state. In films, nucleation can be facilitated by the presence of the substrate, which constitutes a site for heterogeneous nucleation. In the case of the Pt(111)-layered silicon substrate, the (002) plane of the wurtzite ZnO structure and the (111) plane of FCC Pt have similar atomic configurations and thus smaller lattice mismatch in comparison with other

substrates. The crystallographic relationship between ZnO and platinum substrates along the *c*-axis is illustrated schematically in fig. 3.7, which shows better lattice matching of (002) ZnO on a Pt(111)-layered silicon wafer over (002) ZnO on a Pt(002)-layered silicon wafer. Therefore, smaller lattice mismatching between ZnO and the substrate seems to facilitate (002)-oriented nuclei, and thereby promote growth in this orientation.

The observed results can be explained in terms of a nucleation and growth process. From a thermodynamic perspective, it has been demonstrated that the driving forces that govern the transformation from the amorphous (pyrolyzed) film to the crystalline film can play a significant role in defining the active nucleation events and, thereby, film orientation and microstructure. The homogeneous nucleation of a spherical crystallite in an amorphous film can be given by means of the Gibbs free energy change [130].

$$\Delta G_{\text{hom}} = V(\Delta G_v + \Delta G_e) + A\gamma \dots\dots\dots (3.9)$$

where *V*, *A*, *G_v*, *G_e*, and *r* are, the nuclei volume, the interfacial area between the nuclei and the parent amorphous phase, the difference in volume free energy, the elastic strain energy, and the interfacial energy of the newly formed interface. From

differentiation of Eq. (3.9), the energy barrier for a homogeneous nucleation can be derived as:

$$\Delta G_{\text{hom}}^* = \frac{16\pi\gamma^3}{3(\Delta G_V + \Delta G_e)^2} \dots\dots\dots (3.10)$$

In heterogeneous nucleation, which happens commonly at the interface of film and the substrate, the energy barrier for the nucleation can be expressed as:

$$\Delta G_{\text{hetero}}^* = \frac{16\pi\gamma^3}{3(\Delta G_V + \Delta G_e)^2} \cdot f(\theta) \dots\dots\dots (3.11)$$

where $f(\theta)$ is a factor that can be determined by the surface energies of the film and the substrate. The energy barrier of ΔG_{hom}^* will change depending on the elastic strain energy resulting from the lattice mismatch between ZnO and the substrate. Since ΔG_V is negative and ΔG_e is positive, the lattice mismatch leads to a difficult nucleation and growth process. Therefore, the crystallinity may not be well developed on the amorphous substrate as shown in fig. 3.7.

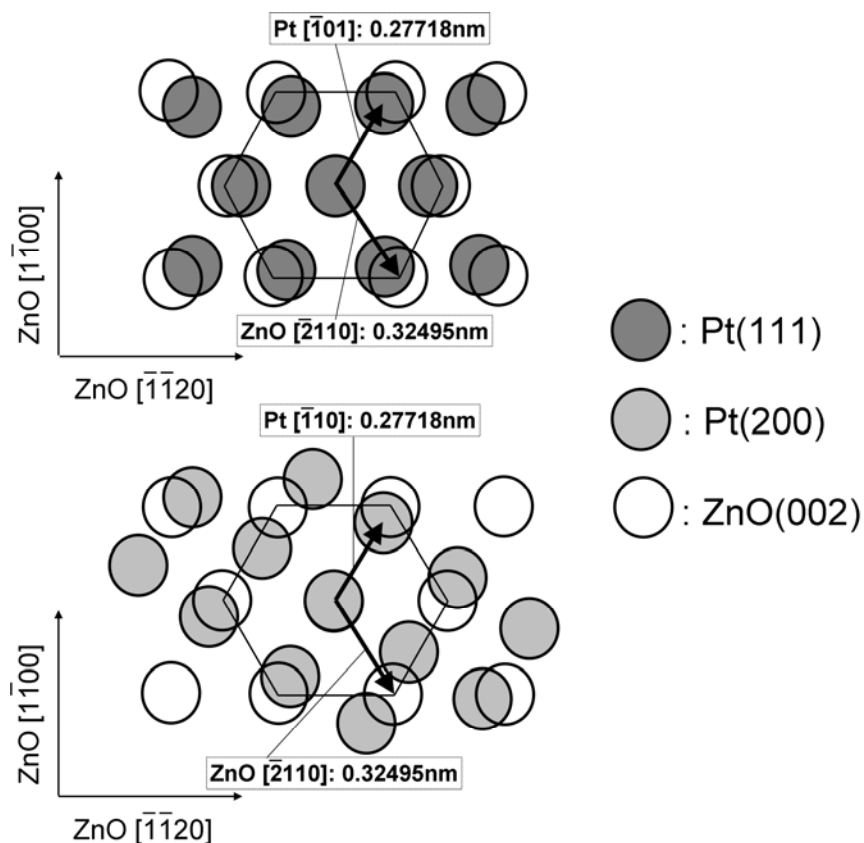


Fig. 3.7 Schematic diagram of crystallographic surface configuration between ZnO(002) and Pt(111) and Pt(200)

When comparing CSD ZnO solution systems with different solution chemistry, it is believed that a stronger dependence of the substrate on the growth behavior of our CSD ZnO films may be correlated with the modification of the molecular scale structure of solution. It is known that aminoethanols, such as monoethanolamine (MEA) and diethanolamine (DEA), act as bidentate ligands to Zn^{2+} , making the solution stable against any precipitate by forming stronger bonds[131]. In addition, the chelating agent plays a role in the preferred orientation of the films. To appraise the role of the chelating

agent, DEA (Diethanolamine) and MEA (Monoethanolamine) with a fixed concentration of 1:1 to zinc acetate were used.

The crystallization behavior of ZnO films, as affected by different precursor solutions and substrates, was characterized by XRD analysis as shown in fig. 3.8. ZnO films derived by MEA chelating have a strong ZnO(002) peak intensity on both polycrystalline Pt(111)/Si and amorphous SiN_x/Si substrates. ZnO films prepared by DEA chelated solution possesses a very high degree of (002) peak on Pt(111)/Si substrate, while the film grown on SiN_x/Si did not show a clear ZnO(002) peak. Peaks of ZnO were only observed when a logarithmic scale of the intensity was used, as shown in fig. 3.8. This feature was very similar irrespective of pyrolysis temperature ranging from 200 to 400°C, and regardless of solution concentration ranging from 0.1 – 0.5 Mol. This suggests that the type of chelating agent strongly influences the crystallization of ZnO films. DEA, which has a boiling point of 270°C, may promote higher degree of polymerization compared with MEA (b.p. = 170°C). Different degrees of polymerization due to the molecules of the chelating agent can affect the crystallization process, which is the transformation of gels or of the amorphous pyrolyzed state to crystalline piezoelectric materials.

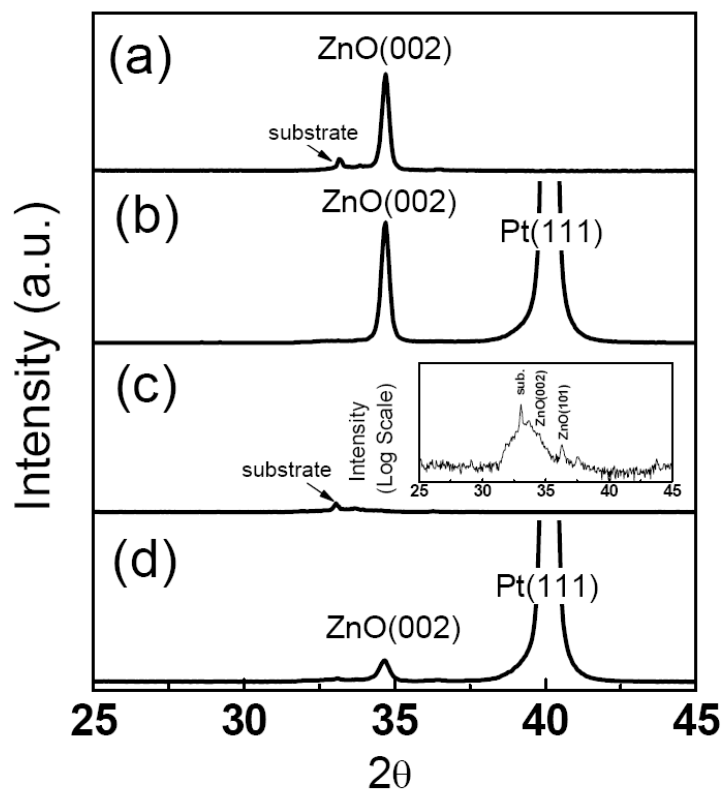


Fig. 3.8 X-ray diffraction patterns of ZnO films grown on different substrates from sol-gel solutions modified by two different chelating agents of 0.5M solution concentration, pyrolyzed at 300°C for 10min and annealed at 700°C for 1hr

- (a) with MEA chelated solution on SiNx/Si substrate
- (b) with MEA chelated solution on Pt(111)/Si substrate
- (c) with DEA chelated solution on SiNx/Si substrate
- (d) with DEA chelated solution on Pt(111)/Si substrate.

This can be explained in terms of a nucleation and growth process. The addition of chelating agents increases the bonding force of the gel, which can increase the energy barrier for nucleation and growth and, hence, the energy barrier for crystallization. Since DEA forms stronger bonds compared with that of MEA in a gel and/or pyrolyzed structure, the crystallization from a DEA chelated precursor solution may involve a

higher nucleation barrier as shown in fig. 3.9. the lower energy barrier for a MEA solution system may facilitate the c-axis growth of ZnO, which is the lowest energy direction of ZnO. On the contrary, the crystallization of ZnO films from DEA chelated precursor solution can be hindered by the higher energy barrier for crystallization. Therefore, crystallization can be promoted only when the lattice between the ZnO film and the substrate matches by reducing the elastic strain energy attributable to the energy barrier. This result can explain prior reports as to why ZnO films prepared by a MEA chelated solution system show such a strong degree of c-axis orientation on glass substrates [35, 112, 132], while DEA systems do not show c-axis orientation [131].

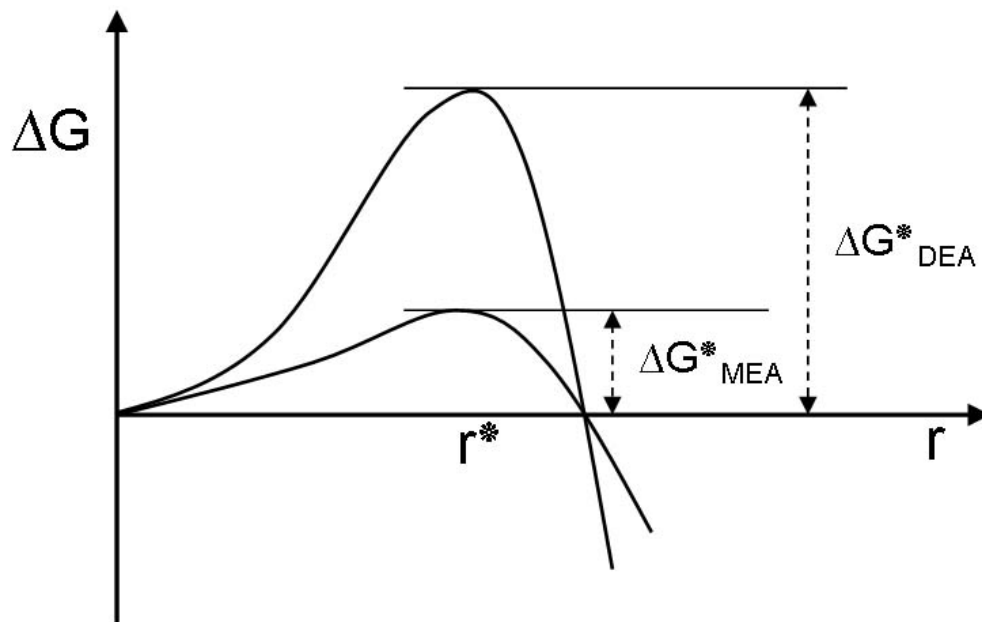


Fig. 3.9 Schematic diagram of energy barriers of DEA- and MEA-chelated solutions

Another explanation of the chelating agent effect on the film orientation is related to the gel viscosity change caused by the additive [133]. MEA chelated solutions have low gel viscosity, which facilitates the re-arrangement of the grains, potentially enhancing the film orientation. In any case, modification of the molecular scale structure in the chemical solution is a factor that can have an influence on the crystallization behavior.

3.5 Raman Characterization on Thin Film Structure

The crystallinity, stress state, and free carrier concentration of solution-derived ZnO films were investigated by Raman Spectroscopy, since these properties are strongly related to the final performance of the acoustic wave device. The crystallinity is related to the piezoelectric property, the stress state to the acoustic wave propagation through the film material, and the free carrier concentration to the energy loss. For the Raman experiment, ZnO films with 20 layers at a thickness of 650nm were fabricated using a 0.7M concentration of the precursor (as shown in fig. 3.1), because of better results with thicker films.

ZnO has a Wurtzite crystal structure with 6-fold symmetry, which belongs to space group C_{6v} ⁴. By group theory, ZnO can have A_1 , $2B_2$, E_1 , and $2E_2$ modes. A_1 and E_1 modes are polar, and can be split to Longitudinal Optical (LO) and Transverse Optical (TO) modes. The typical mode frequencies of ZnO for the A_1 (TO) mode, A_1 (LO) mode, E_1 (LO) mode, and E_1 (TO) mode are 381cm^{-1} , 574cm^{-1} , 585cm^{-1} , and 408cm^{-1} , respectively. $2B_1$ modes are silent. $2E_2$ modes are non-polar, and can have E_2 (high) and E_2 (low). Their frequencies are 437cm^{-1} and 101cm^{-1} for E_2 (high) and E_2 (low) modes, respectively. Peak positions of the A_1 (LO) and E_1 (LO) modes shift as a function of the charge carrier concentration, as well as the stress in the film. However, the E_2 mode shifts as a function of the stress only, and can therefore be used for stress analysis. In the case of fully c-axis oriented ZnO, which is unusual, the E_1 (LO) mode cannot be detected under backscattering geometry. Thus, ZnO that is not fully c-axis oriented can have an E_1 (LO) mode, but, due to the small frequency difference between the A_1 (LO) and E_1 (LO) modes, these two frequencies are not easily resolved. Usually, the two modes combine to form one peak in the range between the true A_1 (LO) and E_1 (LO) frequencies, which includes the information of both the A_1 (LO) and E_1 (LO) modes. This is called the Quasi-LO mode (QLO), and is also frequently found in other hexagonal structures. Additionally,

other modes at 331cm^{-1} , 540cm^{-1} , and 661cm^{-1} are present due to a multi-phonon scattering process.

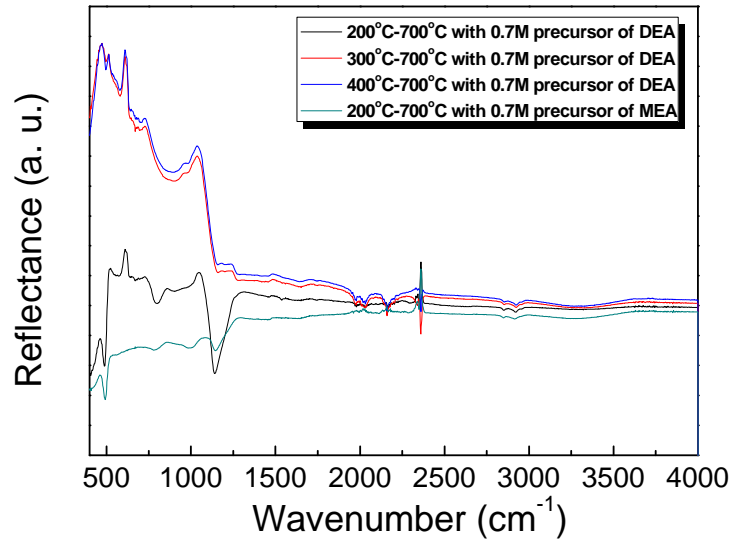


Fig. 3.10 FTIR spectrum of CSD ZnO films with 0.7M precursors

Upon analysis of the Raman spectrum data of the CSD ZnO films, the ZnO film fabricated with the DEA-chelated precursor, pyrolyzed at 200°C , and annealed at 700°C was found to be not fully crystallized. ZnO films with different pyrolysis temperatures on the Pt(111) substrate were analyzed using FTIR (see fig. 3.10), since this measurement can provide a fingerprint of the chemical bonding presence in the films. A prominent peak for the above DEA-chelated precursor film is found at 1139cm^{-1} , while, in the case

of the film made with the MEA-chelated precursor, a small peak is found at 1141cm^{-1} . These peaks correspond to the C-N bonding that results from DEA [123] and MEA [115]. In the case of the precursor with MEA, most of the organics were evaporated, while in the precursor with DEA, much of the organics remain in the film. The reason for the existence of these peaks might be that the pyrolysis temperature of 200°C does not provide enough energy to evaporate the organics in the precursor, even though the film undergoes the annealing step at 700°C immediately after pyrolysis. The residual organics might still be trapped in the film even after annealing, causing the film to be not fully crystallized. Thus, the film fabricated by the DEA-chelated precursor followed by 200°C pyrolysis and 700°C annealing cannot be considered for stress analysis due to the not fully-crystallized state of the film.

For the analysis of Raman spectroscopy, it is worthwhile to investigate the QLO and $E_2(\text{high})$ modes because, among Raman modes, the QLO mode shifts as a function of both the charge carrier concentration and the stress state, while the E_2 mode shifts as a function of the film stress only. For the effect of the heat treatment temperatures on the film properties, data was obtained from Raman spectroscopy to assess the QLO mode. As shown in fig. 3.11 (a), ZnO films from the DEA-chelated precursor, pyrolyzed at 200°C , and annealed at 700°C have a tendency to be amorphous. Comparing the ZnO films

shown in fig. 3.11 (a) and (b), it can be seen that the intensity of the QLO peak decreases as the pyrolysis temperature is increased. The effect of annealing temperature was also examined. From fig. 3.11 (c) and (d), it was found that ZnO film from the DEA-chelated precursor that was pyrolyzed at 300°C and annealed at 500°C has low crystallinity, while ZnO film made from the MEA-chelated precursor has high crystallinity. This also shows the difference between the chelating agents. Even though the results of TG/DSC (fig. 3.3) show that crystallization can occur above 425°C with the DEA-chelated precursor, it may be that annealing at 500°C for 1hr is still not able to provide enough energy for crystallization in such a thick and concentrated gel. However, ZnO films with the MEA-chelated precursor can be crystallized by annealing at 500 °C for 1 hour. Other ZnO films show the fully crystallized state and confirm that the peak intensity of QLO mode decreases with increasing annealing temperature.

There exist two possible reasons to explain the decrease in the peak intensity of the QLO mode. As previously mentioned, this mode includes the information of two proper modes, $A_1(\text{LO})$ and $E_1(\text{LO})$, which are related to the free carrier concentration, and, in case of the $E_1(\text{LO})$ mode, the peak intensity is related to the atomic ratio between Zn and O. When the ratio is close to 1, the peak intensity decreases [134]. It was found that the intensity of the $E_1(\text{LO})$ mode is due to excess zinc in ZnO [135]. So,

at elevated annealing temperatures, the atomic ratio approaches 1 as oxygen is absorbed from the surroundings, decreasing the peak intensity of QLO. Another possible explanation is scattering by Raman active phonons [134, 136]. The elevated annealing temperature can increase grain size in the ZnO film, which will reduce the grain boundary region. This can lead to a reduction in the influence of built-in electric fields by the grain boundaries, thus reducing the scattering by Raman active phonons.

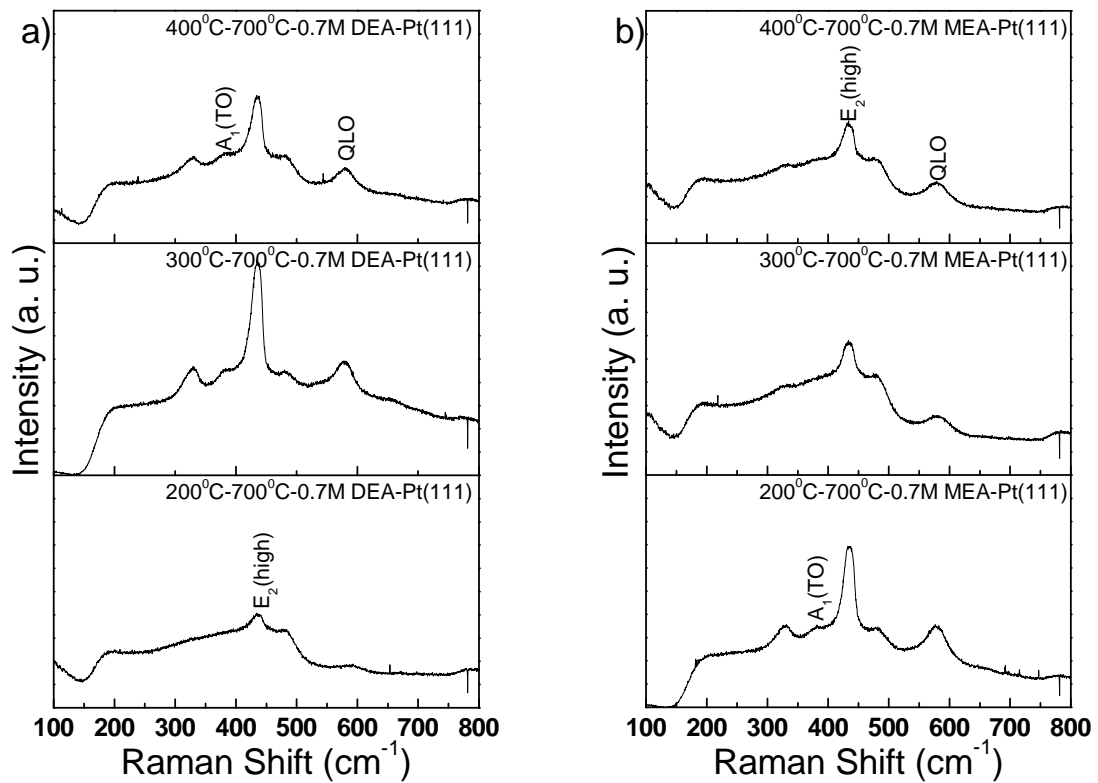


Fig. 3.11 Raman data for the study of the pyrolysis temperature effect on 20 coated ZnO film with 0.7M solution concentration

- ZnO films derived by DEA-chelated precursor annealed at 700°C with different pyrolysis temperature
- ZnO films derived by MEA-chelated precursor annealed at 700°C with different pyrolysis temperature

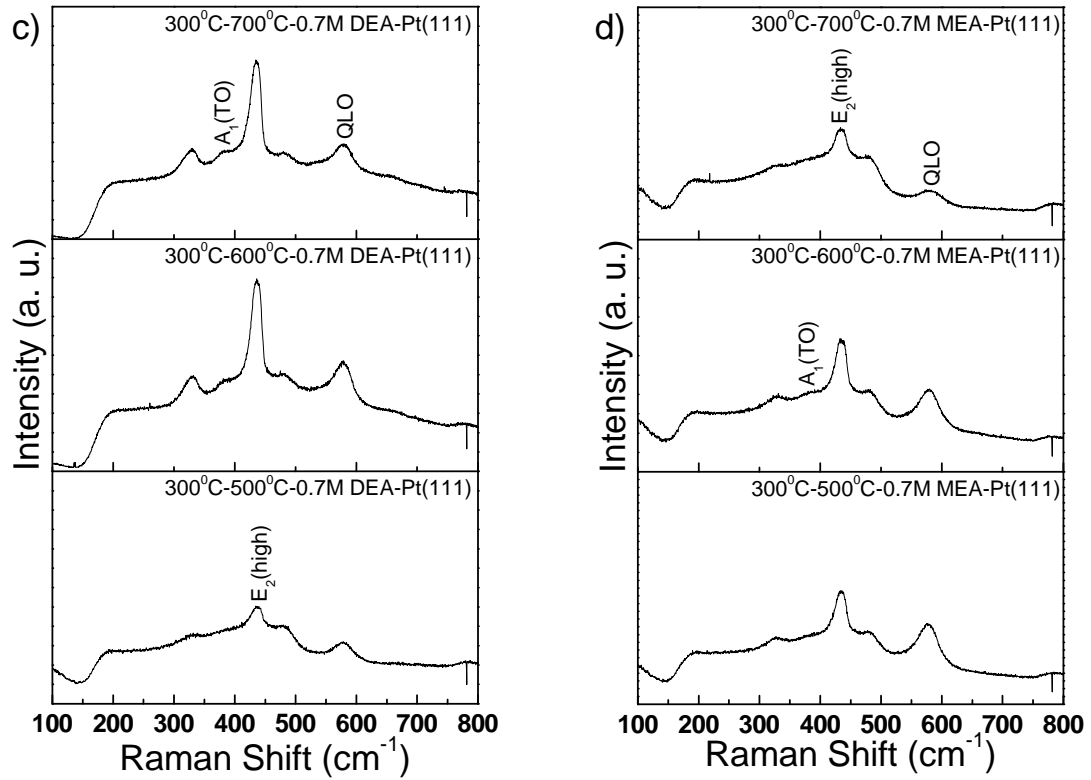


Fig. 3.11 Continued

- c) ZnO films derived by DEA-chelated precursor pyrolyzed at 300°C with different annealing temperature
- d) ZnO films derived by MEA-chelated precursor pyrolyzed at 300°C with different annealing temperature

The E_2 mode of the Raman spectrum was assessed to estimate the stress state in the films by comparing the measured peak position with the standard reference peak position. A decrease or increase in the E_2 mode frequency is attributed to tensile stress or compressive stress in the films, respectively [137]. Because several peak positions of the E_2 mode can be found in the literature (e.g. at 437 cm^{-1} [134, 138, 139], 436.2 cm^{-1} [140], 436 cm^{-1} [141], and 435 cm^{-1} [137]), the mode frequency in wavenumber needed to be

measured using a ZnO single crystal (Eagle Pitcher Inc.) by Raman spectroscopy and was determined to be 434.8 cm^{-1} (fig. 3.12).

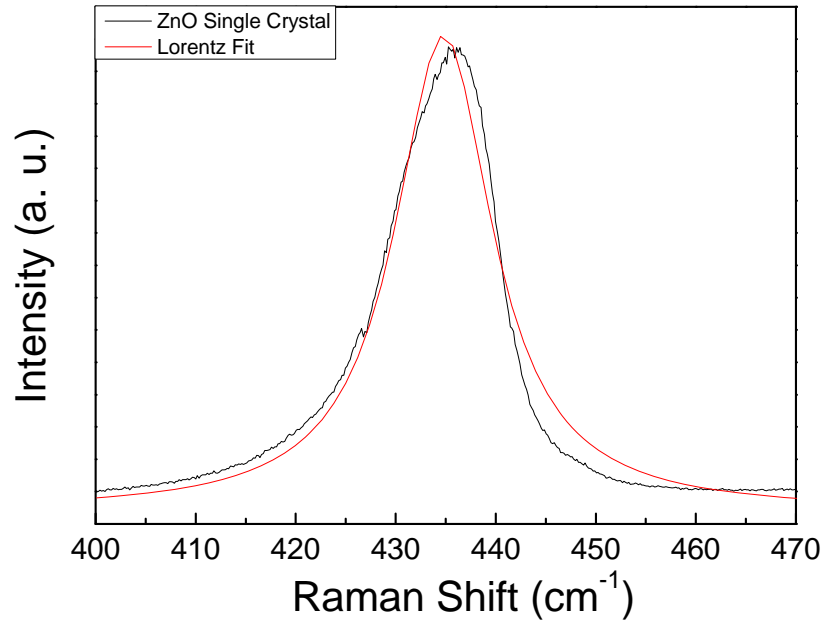


Fig. 3.12 E_2 mode of ZnO single crystal by Raman experiment

A Lorentzian function was used for fitting the raw data of Raman experiment. After obtaining the data, baselines were drawn and subtracted from the background. Then, the Lorentzian function was used to find the peak position. The graphs of Raman data in this experiment were obtained by the same procedure as detailed above. To evaluate the internal stress state in the films, the E_2 mode was enlarged, with the results shown in fig.

3.13. As already mentioned, ZnO films with 200°C pyrolysis and 700°C annealing, and with 300°C pyrolysis and 500°C annealing show an amorphous tendency and were not included for the peak analysis. However, the peak positions of the E₂ mode are summarized in Table 3.1.

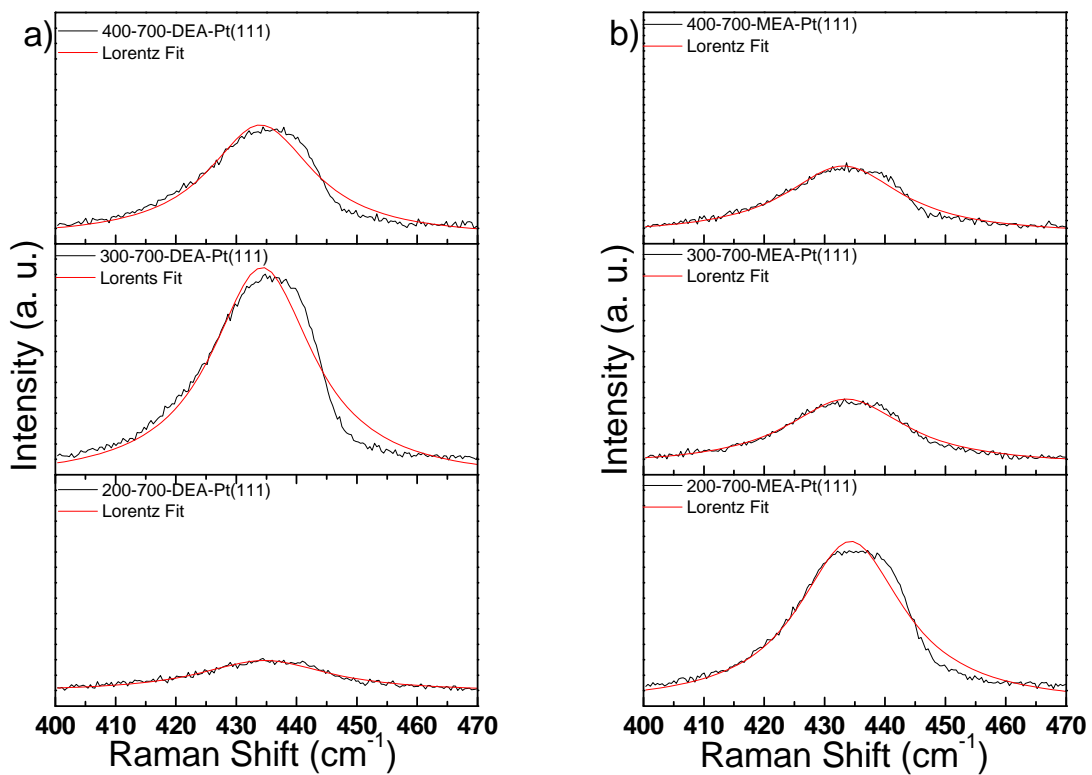


Fig. 3.13 Raman data of E₂ mode in ZnO films on Pt(111)/Si substrate with different chelating agent and different heat treatment by 0.7M solution concentration
a) with DEA-chelated precursor with 200°C - 400°C pyrolysis and 700°C annealing
b) with MEA-chelated precursor with 200°C - 400°C pyrolysis and 700°C annealing

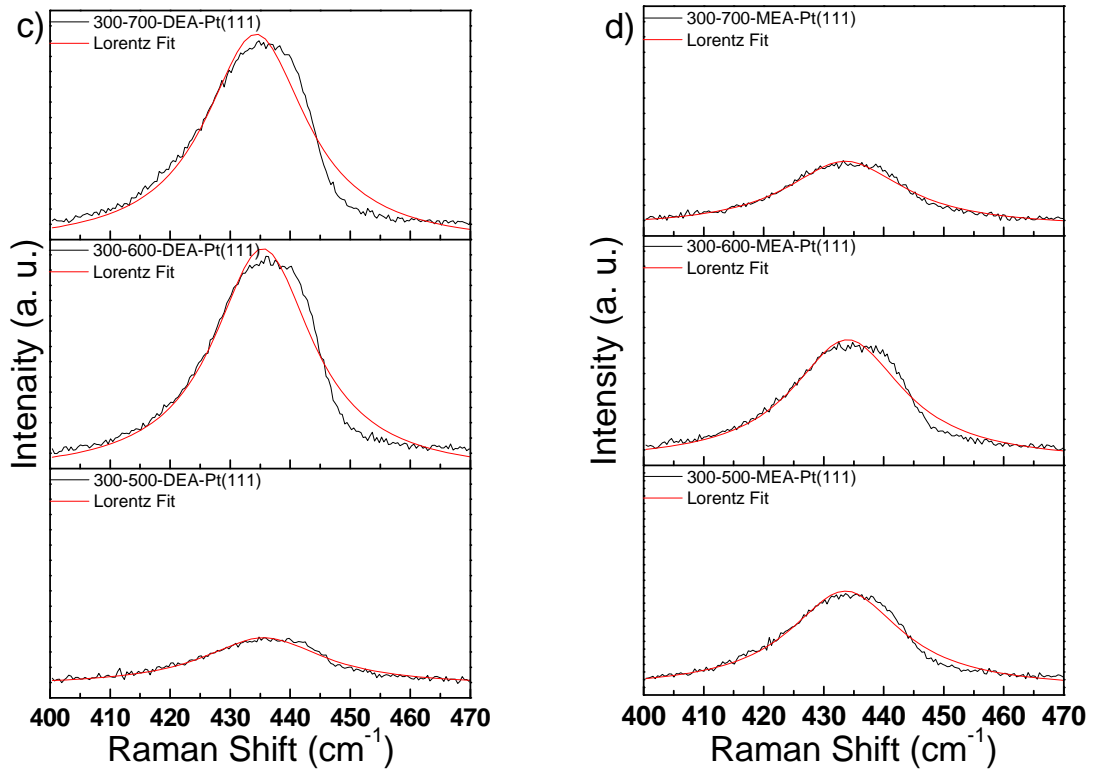


Fig. 3.13 Continued

- c) with DEA-chelated precursor with 500°C - 700°C annealing and 300°C pyrolysis
- d) with MEA-chelated precursor with 500°C - 700°C annealing and 300°C pyrolysis

Comparing the peak positions of the E_2 mode in Table 3.1 with the positions of 437 cm^{-1} from literature and 434.80 cm^{-1} from the ZnO single crystal measurement, most films show tensile stress. This result is comparable to that of sputtered ZnO films, which show compressive or tensile stress depending on the sputtering gas pressure and its ratio.

Table 3.1 Summary of Raman data with 20 coated ZnO films on Pt(111)/Si substrate with different chelating agent and different heat treatment by 0.7M solution concentration

DEA			MEA		
Heat Treatment	Peak Position (cm ⁻¹)		Heat Treatment	Peak Position (cm ⁻¹)	
	Pt(111)	SiNx		Pt(111)	SiNx
200°C -700°C	Not fully crystallized		200°C -700°C	434.3	434.3
300°C -700°C	434.3	434.2	300°C -700°C	433.6	433.8
400°C -700°C	434.0	433.4	400°C -700°C	433.1	434.1
300°C -500°C	435.6	435.1	300°C -500°C	433.6	433.5
300°C -600°C	435.4	435.3	300°C -600°C	434.0	433.3
300°C -700°C	434.3	434.2	300°C -700°C	433.6	433.8

The difference of the resulting stress states may be due to the differences in the deposition methods. In the CSD method, the deposited films commonly show a tensile internal stress. This is because the stress built up by the contraction of the film during the annealing step transforms the amorphous film into a crystallized state. And, as the temperatures of pyrolysis and annealing are increased, the films show more tensile stress, which may be due to the high contraction of the films under the higher temperatures. This study revealed that ZnO films derived by MEA-chelated solutions have more tensile

stress, and, additionally, ZnO films on SiN_x substrates show slightly more tensile stress than those on Pt(111). This is probably due to two factors – thermal mismatch and lattice mismatch. Thermal mismatch results from the different thermal expansion coefficients of the materials. The thermal coefficients of Si₃N₄, Si, and Pt have been reported to be 3.3 ppm/°C, 8.9 ppm/°C, and 4.93 ppm/°C [142], respectively. In the case of anisotropic ZnO, the coefficients along the a-axis and c-axis were experimentally measured to be 3.98 and 6.70 ppm/°C, respectively, in the temperature range of 300-900 °K [143]. Lattice mismatch comes from the difference of the surface configuration between substrate and film. From fig. 3.7, it can be easily understood that the (002) plane of ZnO and the Pt(111) plane have the same configuration as each other, but with different lattice constants. The Pt(111) plane can match well with the (002) plane of ZnO, with the lattice mismatch calculated to be 17%. However, due to the lack of information on the mismatch between the (002) plane of ZnO and the amorphous surface, the stress caused by any mismatch in this case cannot be easily estimated. Thus, it cannot be exactly determined which case is more effective in alleviating the internal stress due to lattice mismatch.

3.6 Evolution of Morphology and Surface Topograph

The solution derived ZnO films were examined by SEM and AFM to investigate their microstructure and surface roughness. These attributes can affect the propagation of the acoustic wave through the material, and the characteristics of the nucleation and growth process are known to affect the resulting microstructure of CSD films. Fig. 3.14 shows ZnO films on different substrates and at different annealing temperatures. All ZnO films in fig. 3.14 were pyrolyzed at 300°C, with annealing temperatures of either 500 or 700°C. Films annealed at 500°C show a similar microstructure consisting of small grains for all three different types of substrates. Grain sizes of ZnO films become larger with increasing annealing temperature. ZnO film on Pt(111)/Si shows a microstructure consisting of larger grains in comparison with ZnO film on Pt(200)/Si and amorphous SiN_x/Si substrates. Enhanced grain growth of solution-derived ZnO film is clearly observed on the Pt(111)/Si substrate. The surface roughness values of ZnO films on the three substrates are measured to be around 1.5 – 3.5 nm. When compared with the roughness of ZnO films prepared at 300°C pyrolysis and 700°C annealing, the RMS value of ZnO on the (111)-oriented Pt/SiO₂/Si substrate (3.5 nm) is slightly larger than that of ZnO on the SiN_x-coated Si substrate (3.0 nm), as shown in fig. 3.15. This result can also

be contributed to the enhanced grain growth originating from better lattice matching between film and substrate.

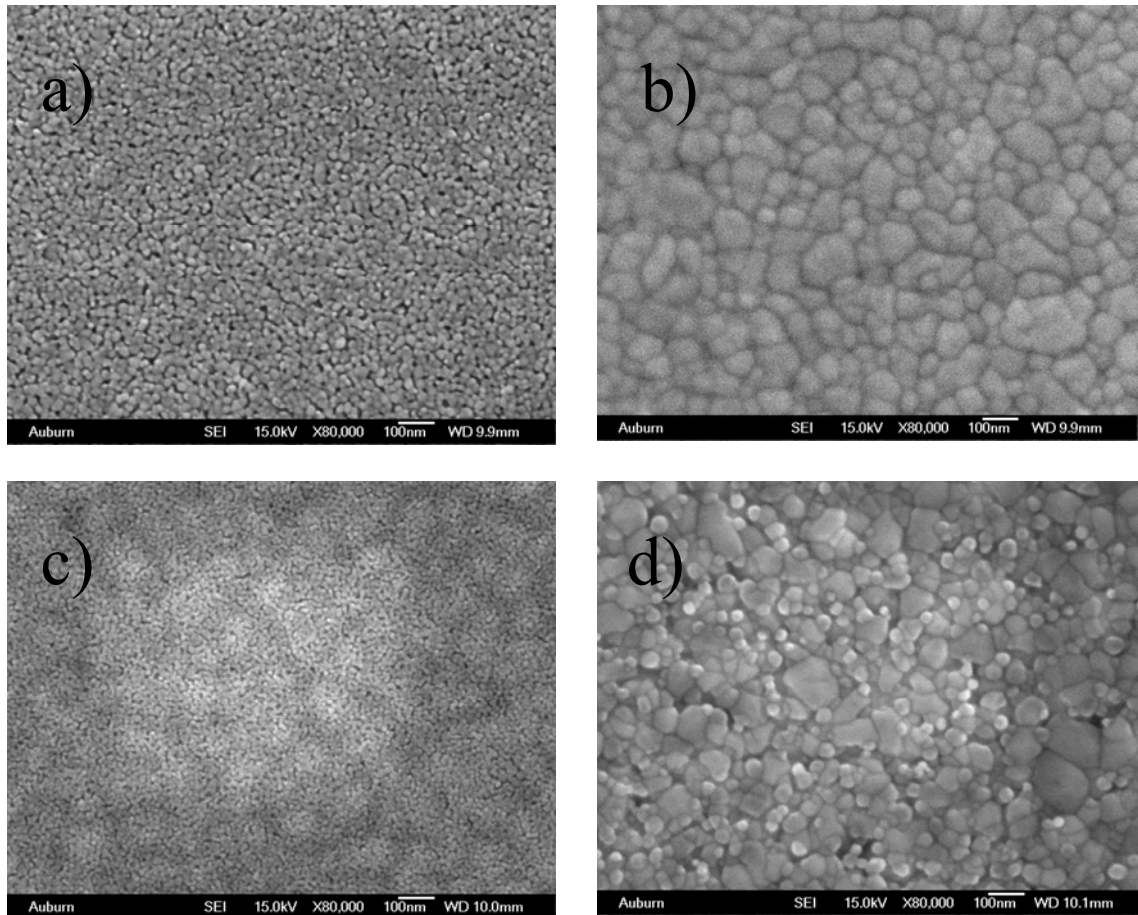


Fig. 3.14 SEM images of ZnO films prepared at different conditions by 0.1M DEA chelated precursor

- a) pyrolyzed at 300°C and annealed at 500°C on Pt(111)/Si
- b) pyrolyzed at 300°C and annealed at 700°C on Pt(111)/Si
- c) pyrolyzed at 300°C and annealed at 500°C on Pt(002)/Si
- d) pyrolyzed at 300°C and annealed at 700°C on Pt(002)/Si

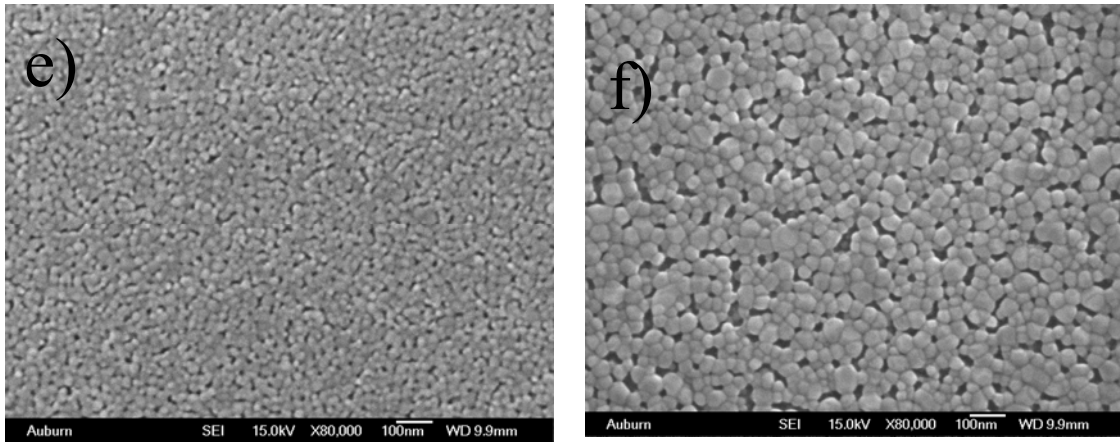


Fig. 3.14 Continued

- e) pyrolyzed at 300°C and annealed at 500°C on amorphous SiN_x/Si
- f) pyrolyzed at 300°C and annealed at 700°C on amorphous SiN_x/Si

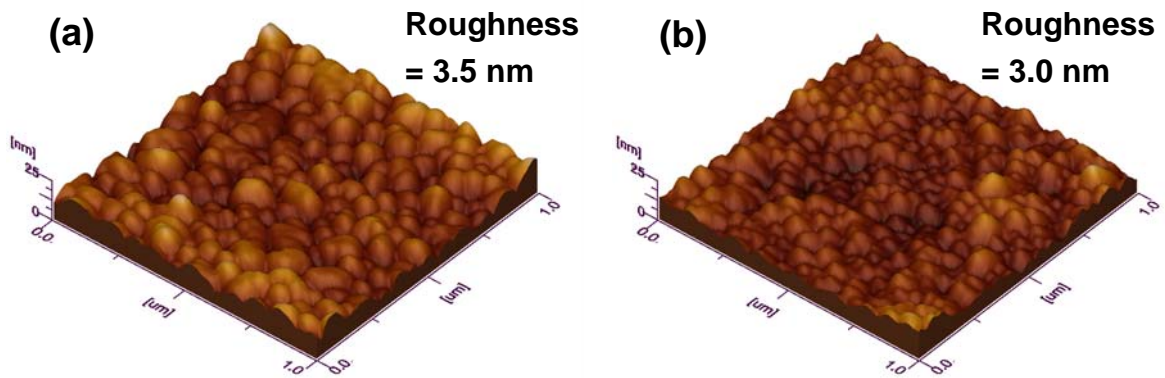


Fig. 3.15 AFM surface morphology of ZnO films grown on Pt(111)/Si and amorphous SiN_x/Si substrates (pyrolysis = 300°C, annealing = 700°C, film thickness = 360 nm)

3.7 Conclusion

Solution-derived ZnO films were investigated for application in acoustic wave devices. The texture of the films was controlled by heat treatment, and the optimum heat treatment condition was found to be 300°C for pyrolysis, and 700°C for annealing. The

substrate was another factor in determining the film texture, because the surface configuration of the substrate can affect the nucleation and the growth of the films due to the lattice match. However, the lattice match was influenced not only by the substrate effect, but by the chelating agents, DEA and MEA, which were used for the stabilization of the gel and for increasing the solubility of the source chemical in the solvent. The additives affect the solution chemistry, which can modify the crystallinity, the stress state, and the preferred orientation of the films. While ZnO films with the MEA chelated precursor had a strong c-axis textured structure, regardless of the surface configuration of substrates, those with the DEA-chelated precursor had no such textured structure on the amorphous silicon nitride surface, due to high energy barrier for nucleation and growth. To obtain the c-axis textured ZnO film with the DEA-chelated precursor, it was found that the configuration of the substrate was an important factor. In the Raman spectroscopy experiment, the intensity of the QLO mode decreased with increasing pyrolysis and annealing temperatures. Most ZnO films were in a state of tensile stress, with more tensile stress being found in ZnO films with the MEA-chelated solution, with higher pyrolysis and annealing temperatures, and on amorphous SiN_x substrates. The stress formed in the films was due to a different thermal expansion and interfacial lattice match between the films and the substrates. From SEM analysis, a denser structure of

ZnO film was found with the MEA-chelated precursor, with very little difference in microstructure between ZnO films on Pt(111) and SiN_x substrates. The roughness of the films was low enough for this application, since the RMS values were in the range of 3-4 nm as measured by AFM. In summary, it was found that the c-axis preferred orientation and the crystallinity of ZnO films can be modulated by controlling the process parameters, such as heat treatment temperatures, substrates, and additives.

CHAPTER 4

ZNO FILM DEPOSITION BY SPUTTERING METHOD

4.1 Introduction

The properties of ZnO films by CSD were investigated in an earlier chapter. However, since CSD is a batch process, it may not be feasible for the mass production of the film. Compared with CSD, deposition by sputtering can be considered to be a practical method for mass production, since it can be performed as a continuous process in the fabrication of piezoelectric films with scalability for large areas. Compared to other deposition processes, such as chemical vapor deposition[25], spray pyrolysis[30], pulsed laser ablation[21, 144] [3, 4], hydrothermal synthesis[23] and chemical solution deposition[104], sputtering has several advantages in the preparation of ZnO films. It can provide low deposition temperature, good adhesion to the substrate, high deposition rate, good process controllability, long-term process stability, and it is easy to deposit films with many components by reacting with rare and reactive gas mixtures [145].

For sputtering deposition, primarily two types of targets have been used: a ceramic ZnO target with RF power, or a metal Zn target with DC power. The Zn target has several advantages over the ZnO target [108, 145-148]. The metal Zn target is much less expensive than ZnO target, due to its easy machinability. Because of its high thermal conductivity, it can be more efficiently cooled. High deposition rates can be achieved by using a DC power supply, which is also less expensive than a typical RF power supply. By using high purity Zn and oxygen, a ZnO film can be deposited that is more pure than that deposited with a ZnO target. Therefore, using a metal Zn target can help avoid the effects of unwanted impurities possibly present in ZnO targets at levels which can influence the resistivity of the deposited ZnO film. However, the zinc-metal/oxygen-gas process is more complicated and difficult to control because the desired film properties may be achieved only in a very narrow process parameter range [145]. Also, in terms of the piezoelectric properties, the best results for ZnO films has been obtained by using a ZnO ceramic target [149]. A sintered, stoichiometric, ZnO ceramic target was used for this study, because of the ease of process parameter control. A comparison between RF and DC sputtering can be found elsewhere [145, 150].

When a stoichiometric ceramic ZnO target is used for ZnO films with pure Ar, a conductive, Zn-rich film is obtained [151, 152]. Thus, partial oxygen pressure in the

sputtering process is needed to attain high resistivity stoichiometric ZnO films [28], because resistivity in at least the M Ω -cm range is necessary to achieve the piezoelectric property in ZnO. The need of oxygen partial pressure is explained by the difference in sputter yield between Zn and oxygen and the vacuum system in the sputtering process. The sputtering yield of Zn is higher than that of oxygen [153], and if a ceramic ZnO target is used under only an Ar atmosphere, non-stoichiometric Zn-rich in will be produced [154]. Another reason is that, during the sputtering process, some of the oxygen from the ceramic target will not arrive at the substrate and end up being pumped out by the vacuum system [155]. Thus, oxygen partial pressure is one of the important process parameters in controlling the properties of ZnO film.

In addition to the oxygen partial pressure, several other process parameters have been investigated and were found to modify the crystal orientation, crystallinity, and other film properties of sputtered ZnO films [156]. These include substrate type [157], sputtering power, sputter temperature and post deposition temperatures, sputtering gases and their ratio, sputtering pressure [158], and target-substrate distance. Among those parameters, the selection of the substrate is an especially critical issue to attain a well-oriented ZnO film. This is because, at the interface between the film and the substrate surface, the difference in lattice parameters, the crystallinity of the substrate [159], and

the surface roughness [160] of the substrate can influence film properties from the initial stage of the nucleation and growth process. Sapphire [161-164], glass [163], quartz [147], Si [28, 165], Al [27], diamond [166], SiO₂, and Pt are the substrates commonly used for ZnO film deposition. Lodder et al. [167] found a well-oriented initial layer on a crystalline substrate surface, but a poorly oriented initial layer on an amorphous substrate surface. Epitaxial ZnO films have been prepared on R-plane sapphire substrates [168]. However, according to Kasuga, it could also be possible that the orientation of the epitaxial films on the same sapphire substrates can be altered by controlling other parameters, such as substrate temperature, vapor pressure, and pretreatment [164].

The crystallinity and the defect state in ZnO films have been significantly improved by heat treatments, such as substrate temperature [147] and post-annealing [163] at an elevated temperature. The enhancement of film crystallinity can be explained by the thermal energy of the atoms in the film. Adatoms with enough thermal energy to diffuse from the surface can move to stable sites, increasing the crystallinity [161] and releasing the strain in the films [169]. Another possible reason is the improvement of stoichiometry in the film, which is related to the defects in ZnO films. Zn interstitials and oxygen vacancies are considered to be native defects in ZnO [61] because their formation enthalpies are lower than other defects [170] possibly present in the films. When the heat

treatments are performed under an environment containing oxygen partial pressure, oxygen can be incorporated into the film [162, 165] and oxidize the uncombined Zn interstitials. Thus, the film crystallinity can be enhanced with the annealing process by reducing the defects in the film [169, 171].

For the acoustic wave device application, the high resistivity of a stoichiometric film is necessary for generating the piezoelectric effect, because electrical conduction in the film can cause electric loss. Additionally, the surface roughness is another important factor for this application, and it was reported that films with smooth surface will have better piezoelectric and high coupling properties [69].

4.2 Detailed Experiment

ZnO films were prepared by sputtering because of its advantage over CSD, as already mentioned. The process parameters investigated in this study include sputtering power, the type of gas and its ratio, sputtering pressure, base pressure, substrate temperature, annealing temperature, and substrate type, which are all known to seriously affect the film properties. The sputter system used in this experiment was a Discovery 18 (Denton Vacuum), which has two cathodes connected to RF and DC power supplies. It

has a confocal configuration of the targets, which are aimed at an angle (i.e. not perpendicular) to the substrate holder. This configuration reduces the bombardment effect and the excessive heat radiation from energetic particles [148] and improves the crystallinity of the film. The substrate holder is located at a distance of 10cm from the target, as shown in fig. 4.1. The substrate holder was also rotated during sputtering to improve the film uniformity. For ZnO film deposition, sputtering power was fixed at 200W ($4.4\text{W}/\text{cm}^2$) RF. Ar and O_2 were used for the sputtering gas, and their ratios were varied to 1:0, 1:1, 1:2, 2:1, and 3:1 with a predetermined sputtering pressure of 8 mTorr.

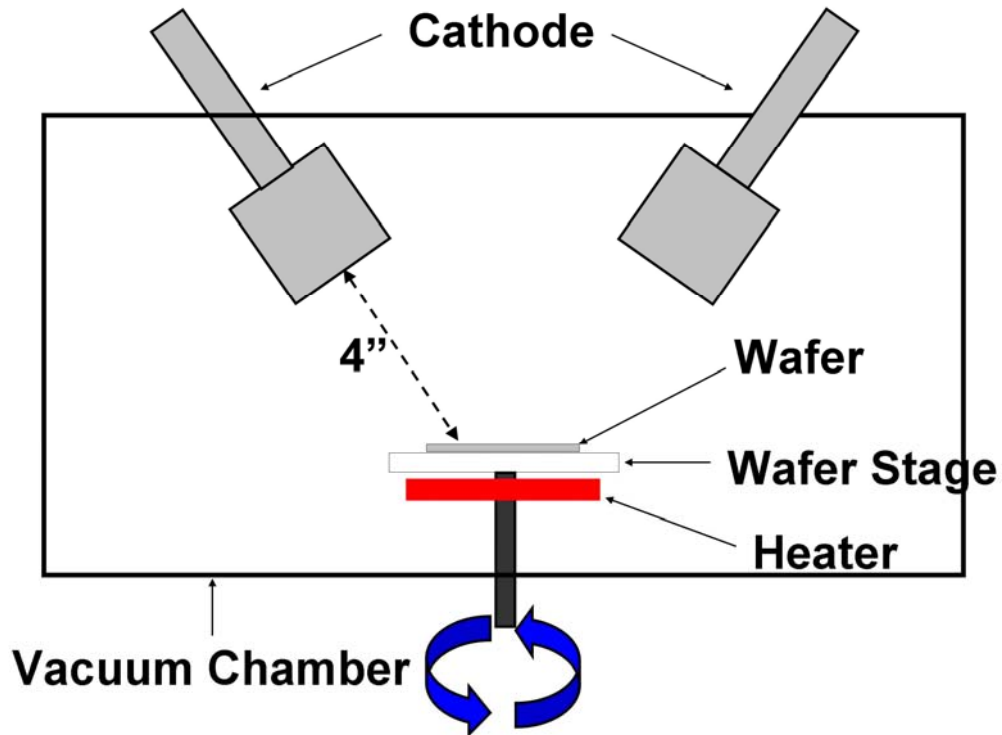


Fig. 4.1 Schematic diagram of the sputtering system configuration.

The sputter chamber was pumped down to a base pressure of 5×10^{-7} Torr. The heat treatment scheme is varied between room temperature and 300°C for the deposition temperature, and with/without an annealing treatment of 600°C . In order to assess the substrate type on the film orientation control, Pt(111)- and Pt(200)- layered silicon wafers were used for the crystalline surface configuration, and silicon oxide- and silicon nitride-layered silicon wafers were used for the amorphous surface configuration.

4.3 High Crystallinity and Morphology Evolution of Sputtered ZnO films through the modification of Substrate and Heat Treatment

The preferred c-axis orientation of ZnO films is considered to be an important factor on the film quality, because the dielectric constant and dissipation factor can be improved as c-axis orientation improves [172]. Similar to solution derived ZnO films, the crystallinity of sputtered ZnO films were also dependent on the interface structure, which is derived from the lattice mismatch and the crystallinity of the substrate surface, shown in fig. 4.2. Pt(111), which has a similar surface configuration to ZnO(002) even though it has different lattice parameters than ZnO, shows excellent textured orientation, while Pt(002) and amorphous SiN_x exhibit a less c-oriented crystal structure. W.T. Lim et al.

[173] compared the crystallinity of sputtered ZnO films on Ru/Si and Al/Si, and found that ZnO films on Ru/Si had more crystallinity, a denser structure, and less biaxial stress in the films than those on Al/Si. It was explained that the Ru/Si substrate has a well-matched structure (HCP) with ZnO. B.T. Khuri-Yakub found better quality ZnO films on the substrates which have a similar crystal symmetry to ZnO [146, 174]. Thus, it is believed that the crystallographic orientation of ZnO film depends on the surface configuration of its nucleating surface [49, 157].

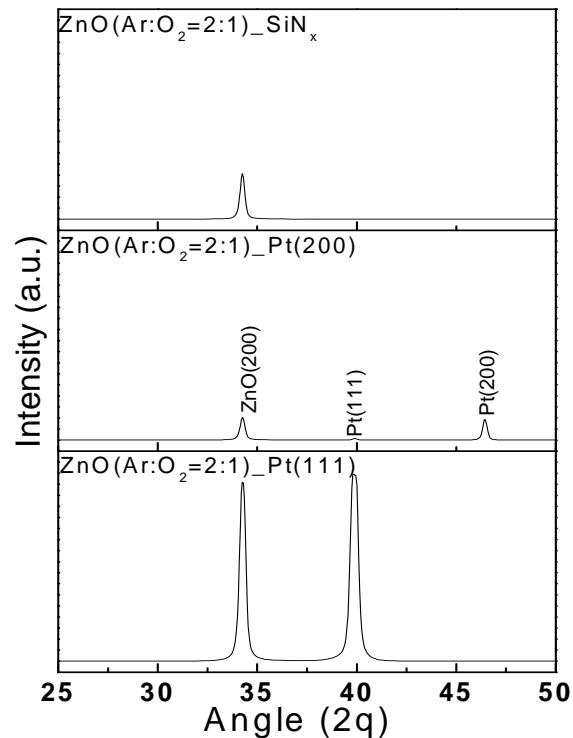


Fig. 4.2 XRD patterns of the sputtered ZnO films deposited at RT on different substrates.

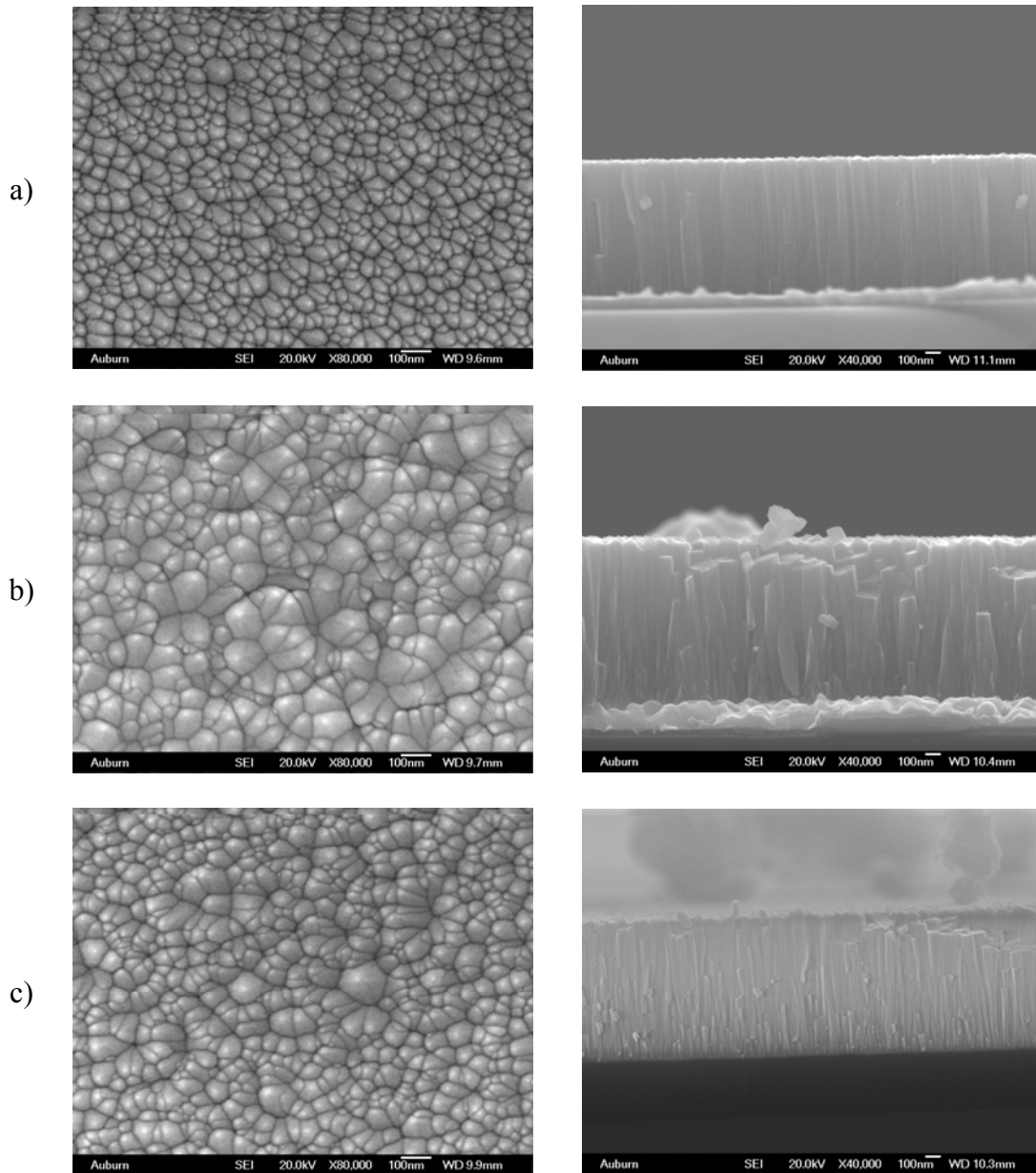


Fig. 4.3 SEM images of 1 μm thick ZnO films prepared by sputtering on different substrates. The gas ratio is $\text{Ar}:\text{O}_2=3:1$. All films were deposited at room temperature.
 a. Pt(111)/Si b. Pt(200)/Si c. Si₃N₄/Si

SEM images of the sputtered films on the different substrates are in fig. 4.3, showing the dependency of the grain size on the substrate type. The smallest grain size of the sputtered ZnO film was found on the Pt(111)-oriented layered silicon wafer, while ZnO films on the mismatched substrates, such as silicon nitride and Pt(200)-oriented layered silicon wafers, demonstrate larger grain sizes. From the side view of the films, the microstructural difference of the films on the different substrates was clearly revealed, as shown in fig. 4.3. The ZnO film on the Pt(111) substrate, which is well-matched with the ZnO(002) plane, appears to have a well-defined and very forthright columnar structure, while the microstructure of ZnO films on the mismatched substrates is less-straight and less-defined.

F.C.M. van de Pol et al. [67] reported a similar trend of small ZnO grain sizes on crystalline substrates and broad grain sizes on amorphous substrates. Moreover, the ZnO film on the Pt(111) layered silicon wafer has a smaller grain size than that on the Pt(200) layered silicon wafer, even though both substrates have a crystalline surface. This may be explained by higher nucleation rate on Pt(111) than on Pt(200). R.J.H. Voorhoeve et al. [175] investigated the adsorption energies of Cadmium on Germanium crystal faces (100), (110), (111), (211) and (331), and found that the (111) face had higher saturation adsorption energy than the (100) surface. The higher saturation adsorption energy of the

(111) face was enough for Cadmium to cover the Germanium surface completely, making a Cadmium-rich surface on Ge(111). This resulted directly from the higher nucleation of Cd on Ge(111) than on Ge(100). Thus, compared with the Pt(200) plane, the Pt(111) plane may supply a higher number of nucleation sites, and this may lead to the smaller grains in the film due to the dominant nucleation process on this plane.

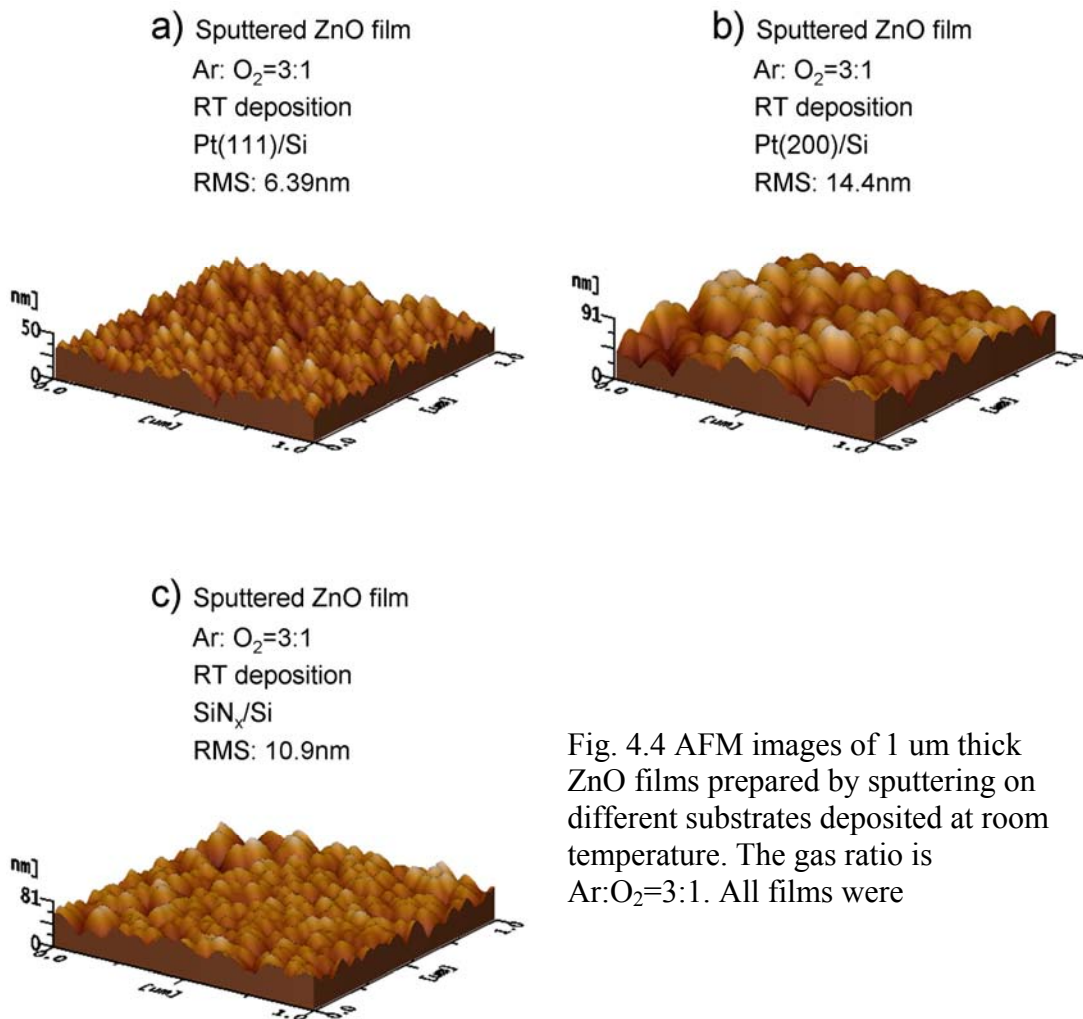


Fig. 4.4 AFM images of 1 μm thick ZnO films prepared by sputtering on different substrates deposited at room temperature. The gas ratio is Ar:O₂=3:1. All films were

The surface roughness was characterized by AFM in non-contact mode, and the area scanned was $1\mu\text{m} \times 1\mu\text{m}$. Under the same deposition conditions, the lowest RMS value was found in the ZnO film on the Pt(111) oriented layered silicon wafer, where the substrate plane matched well with the ZnO (002) plane. Comparing the SEM and AFM results, the smaller RMS value of ZnO film on Pt(111) layered silicon wafer appears to correlate with the smaller grain size. The smooth surface of ZnO film on Pt(111) layered silicon wafer indicates a much more well-oriented film [176] than those on the other substrates. Because a smooth surface and dense structure contribute to a high coupling coefficient and good piezoelectric property of ZnO films [156], the ZnO film on the Pt(111) layered silicon wafer can be expected to possess these attributes.

It has been accepted that the orientation of nuclei may be determined by the tendency of the atoms to pack into the most dense crystal plane [167], and that plane will have the highest surface energy. In the case of ZnO, it is the (002) plane. It is believed that the nuclei will be orientated and grow in the $\langle 002 \rangle$ because it is the fastest growing axis [177]. Yoshino et al. [178] investigated the growth characteristics of ZnO films on various substrates and found that the growth is greatly dependent on the strong interaction between the film and the substrate. The presence of an amorphous ZnO layer and polycrystalline ZnO layer between a c-oriented ZnO film and the substrate was

confirmed by TEM results, lowering crystallinity of ZnO film on the amorphous substrates in some degree. In contrast, a c-oriented ZnO film was produced immediately from the crystalline substrates, as if there was no nucleation barrier due to the strain energy generated from the mismatched substrates. Therefore, it may be believed that the effect of lattice match begins from the initial nucleation stage. In the initial nuclei formation, the strain energy generated from the mismatched substrates (Eq. 3-11) may hinder the nucleation event of $\langle 002 \rangle$ oriented nuclei perpendicular to the surface, and randomly oriented nuclei may grow in a direction perpendicular to the substrate, producing a polycrystalline ZnO layer. On the polycrystalline ZnO, after releasing the strain energy, $\langle 002 \rangle$ oriented ZnO nuclei may be grown in random directions. The randomly growing nuclei can interrupt each other during the growth stage and can be coalesced into a large grain. This is illustrated in fig. 4.5.

The same explanation can be applied to the sputtered ZnO films in this study. Assuming that RF 200W (4.4 W/cm^2) is enough for sputtered ZnO particles to diffuse on the surface, the particles will diffuse to the high energy sites to reduce the surface energy. Since the ZnO(002) plane is the lowest energy plane, ZnO nuclei (crystallites) oriented to $\langle 002 \rangle$ are preferred to nucleate on the substrates. At the initial stage of nucleation and growth, ZnO nuclei on Pt(111) are believed to have $\langle 002 \rangle$ direction normal to the

substrate, while ZnO nuclei on other substrates have more random directions to the substrate due to lattice mismatch. The effect of lattice mismatch can be estimated from lattice constants of these materials. A smaller misfit between ZnO(002) nuclei and the substrate may promote c-orientation of ZnO film. A smaller lattice mismatch (14.7 %) between ZnO(002) ($a=0.32495\text{nm}$ and $c=0.52069\text{nm}$) and Pt(111) ($a=0.3920\text{nm}$) can be calculated compared to that of ZnO(002) (17.1 %) and Pt(200) or amorphous substrates. At the growth stage, ZnO growth on Pt(111) advances to the $\langle 002 \rangle$ direction, while ZnO growth on other substrates experiences more random orientation or weaker texture due to the competition among neighboring grains. The same results can be found elsewhere [159, 178, 179].

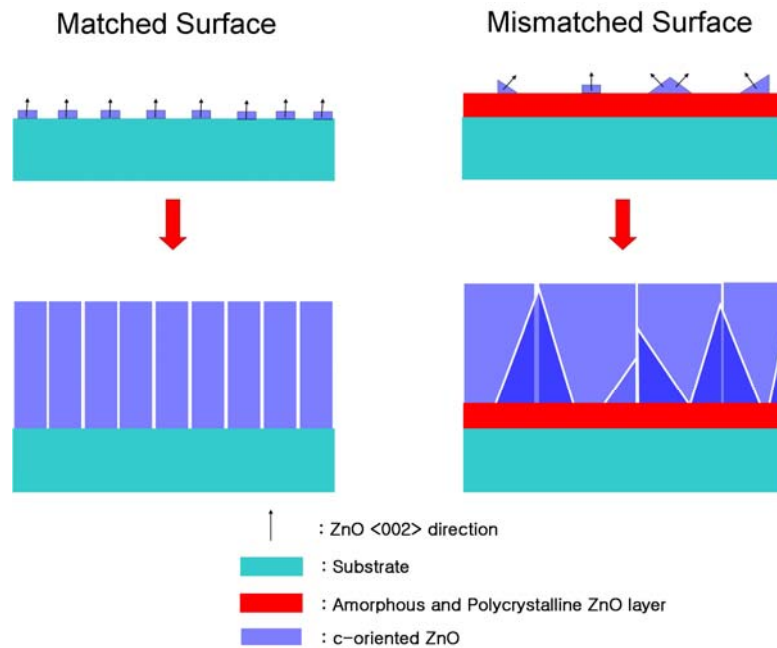


Fig. 4. 5 The effect of the matched and mismatched substrates on the nucleation and growth of ZnO films oriented in the $\langle 002 \rangle$ direction.

It is worthy to note that the surface roughness of the substrate has an effect on the preferred c-axis orientation [179]. J.B. Lee et al. [160] reported that the morphology and the crystallinity of sputtered ZnO films can be modified by the surface roughness of the substrate, and concluded that the preferred c-axis orientation is mainly determined by the surface roughness rather than by other process parameters, such as oxygen content or the chemical properties of the surface. Yoshino et al. [178, 179] reported that a smooth surface promotes the quality of c-oriented ZnO film by controlling the crystal growth, and low FWHM of the films can be achieved on substrates with less surface roughness. As seen in fig. 4.4, a similar tendency was found in our ZnO films. The surface roughness values (RMS) of three types of substrates in this experiment were 4.95 nm for Pt(200), about 2.5 nm for Si₃N₄, and 4.57 nm for Pt(111)substrates. ZnO film on Pt(200) shows the largest grain size and the highest roughness value compared to ZnO films on Pt(111) and Si₃N₄. The grain size of the ZnO film on Pt(200) is larger than that on Si₃N₄, even though Pt(200) has a crystalline surface. Thus, the RMS values and the crystallinity of the sputtered ZnO films in fig. 4.4 might not be solely explained from the nucleation and growth process as discussed before, because of the surface roughness of the substrates. A rough surface can be considered to have a large amount of nucleation sites which can impede the growth of the preferred orientation [180]. In this aspect of the effect of the

surface roughness, ZnO nuclei on Si_3N_4 grow easily in the $\langle 002 \rangle$ direction normal to the substrate without disturbance by other nuclei, while ZnO nuclei on Pt(200) have more random directions although they prefer to grow $\langle 002 \rangle$ direction, due to the rougher surface.

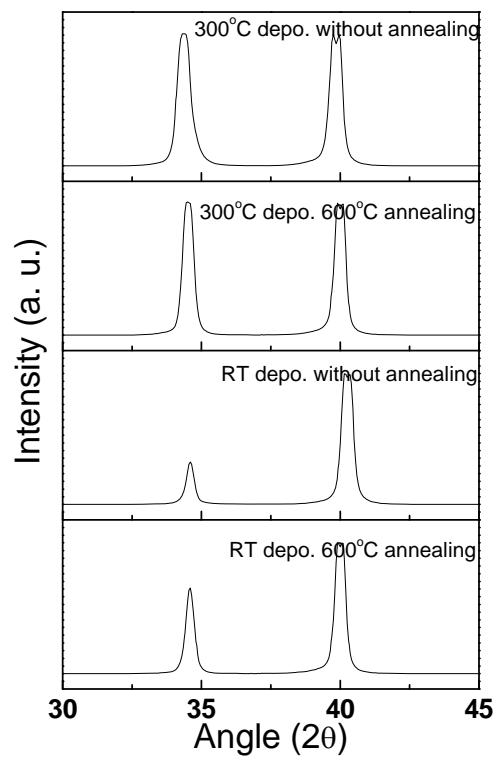


Fig. 4.6 XRD patterns of the sputtered ZnO films deposited at RT with various heat treatment and $\text{Ar}:\text{O}_2=1:1$ ratios on Pt(111) substrates.

The heat treatment effect on the crystallinity was investigated and is shown in fig.

4.6. The films deposited onto Pt(111) have two sputtering temperatures, room

temperature (although it should be noted that the temperature reached as high as 70°C during the entire deposition process) and 300°C. After deposition, the films were put into a furnace maintained at 600°C for 1 hour. The film deposited at RT without annealing has the smallest intensity of the ZnO(002) peak. The annealing process enhanced the film crystallinity as shown in the fig. 4.6. The sputtered ZnO films at 300°C show higher crystallinity than those sputtered at RT. Thus, it can be concluded that heat treatment can be used to improve the film crystallinity.

For a larger degree of crystallinity in the films, heat treatment of the substrate [181-184] and post-annealing [161, 162, 185] has been commonly utilized. In ZnO, ZnO(002) is the lowest energy plane, and a higher substrate temperature and a post-annealing step at an elevated temperature can enhance the diffusivity of the adatoms by the input of thermal energy [186], allowing them to move to stable sites for the lowest surface energy [184, 185]. Z.B. Fang et al. [171] investigated film density as a function of annealing temperature in an air atmosphere. They found that the highest film packing density occurred between 450°C and 600°C. Also, the highest XRD intensity and refractive index almost corresponded to this temperature range, indicating that a better quality of ZnO films can be achieved by annealing [171]. X.H. Li et al. [187] reported a ZnO film deposited at a 350 °C substrate temperature was almost chemically

stoichiometric. However, a further increase in the substrate temperature may deteriorate the film orientation, because the additional thermal energy can break the Zn-O bonds, causing re-evaporation of the deposited adatoms, rather than merely allowing them to move to the lower energy sites [181]. The crystallinity of ZnO film deposited above 450 °C was deteriorated [168], and void generation at annealing temperatures over 600°C was also found [171, 185]. Thus, the control of substrate temperature is one of the main factors in producing a strong c-oriented structure.

The better quality of the ZnO films by heat treatment has been explained by the enhancement of the stoichiometry in the films as well. The investigation of the post-annealing process has been performed under various atmospheres with gases such as H₂/Ar [169], N₂ [162], vacuum [165], air [171], and O₂ [161, 162, 165, 185]. Better crystallinity was obtained from the films annealed under oxygen and ambient air. This phenomenon is related to the defects in ZnO films. Zn interstitials and oxygen vacancies are considered to be native defects in ZnO [61] since their formation enthalpies are lower than other defects [170] that may be present in the films. When oxygen partial pressure exists in the environment during the heat treatment process, oxygen can be incorporated into the film [162, 165] and oxidize the uncombined Zn interstitials. Thus, film crystallinity can be enhanced with the annealing process by reducing the defects in the

film [169, 171]. Under other atmospheres, the crystallinity was degraded due to the re-evaporation of oxygen from the films [162, 165] accompanied by an increase in the amount of defects. Thus, an atmosphere including oxygen is needed to achieve high quality ZnO film [185].

4.4 Microstructure Evolution of Crystalline ZnO films influenced by Sputtering Gas and Pressure

Investigation of oxygen partial pressure is one of the key issues in the sputtering deposition of ZnO film because, by controlling oxygen concentration, the film orientation can be modified [188]. The sputtered ZnO films on SiO₂/Si substrates were studied with various oxygen partial pressures at a fixed total pressure (~ 8mTorr) at room temperature. No other peaks, except ZnO(002) and (004) peaks were found, indicating well-crystallized sputtered ZnO. However, the highest intensity for the c-axis orientation of ZnO film was found at Ar:O₂ = 3:1, which is the argon rich condition (fig. 4.7).

The existence of an optimum oxygen concentration for achieving a highly c-oriented ZnO film has been reported in the references [189-192]. J.J Chen et al. found relatively stronger texture and high XRD peak intensity at this condition [190], which can

be considered as an indicator of a high coupling factor [191]. Also, R. Ondo-Ndong reported the lowest stress and FWHM at this condition [192]. For the effect of oxygen gas on the film orientation, Aita et al. [28] investigated the ZnO crystallinity with variation of 0% to 100% oxygen in an argon-oxygen gas mixture, and observed that 25% oxygen in the gas mixture showed the maximum intensity in XRD. In this condition, the relative number of the non-basal planes to the basal planes and the relative number of Zn^{2+} to ZnO^{+} in the plasma are at a minimum, which leads to minimum disorder in the ZnO films, *i.e.* highly c-oriented ZnO films.

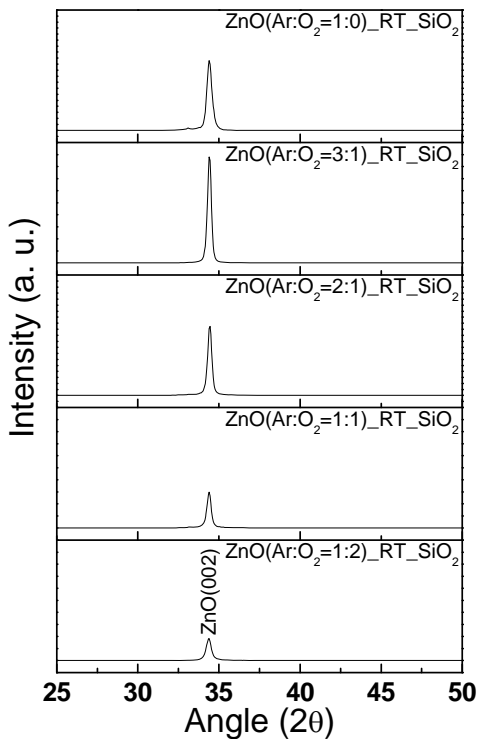


Fig. 4.7 XRD patterns of the sputtered ZnO films deposited at RT with various gas ratios.

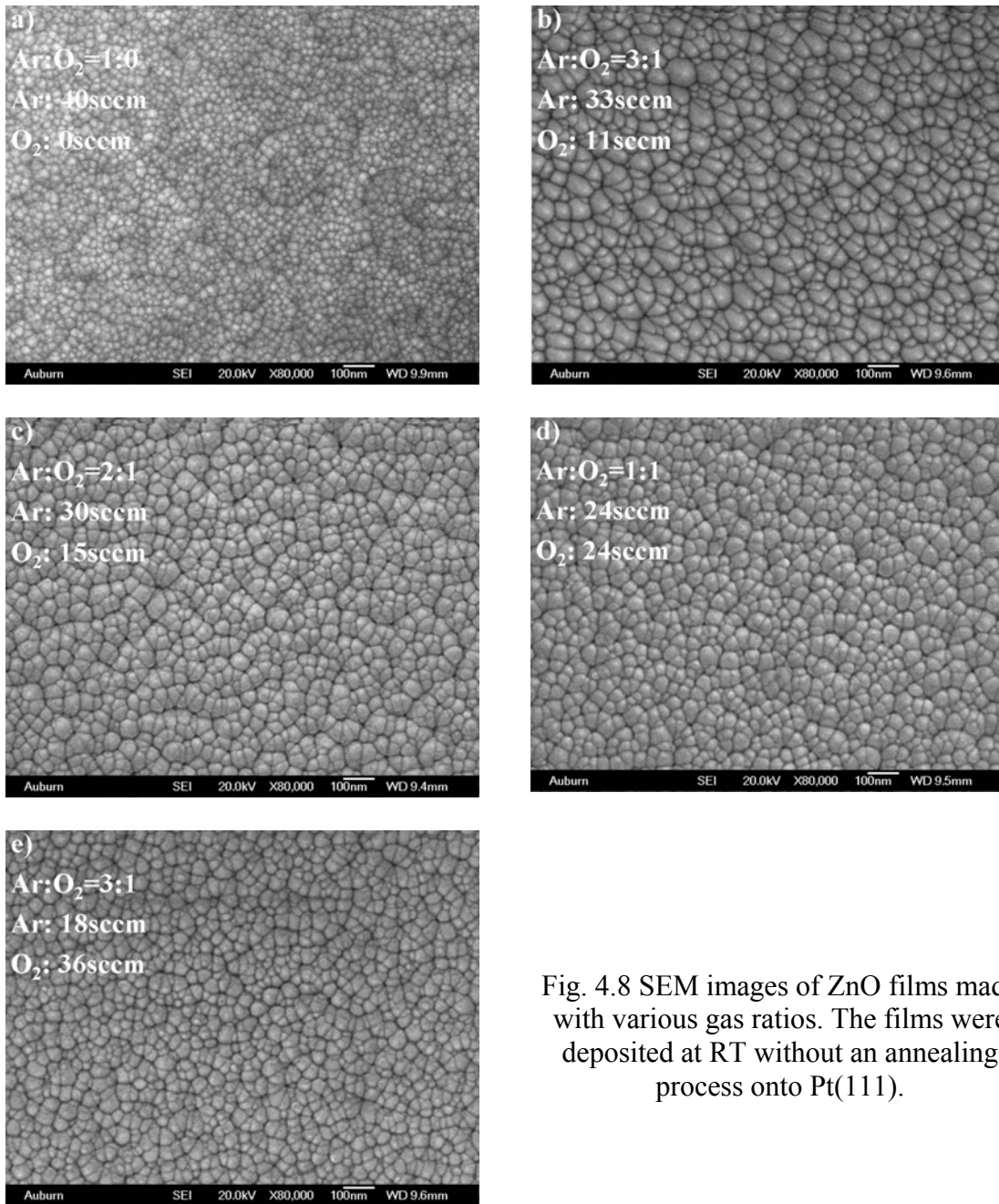


Fig. 4.8 SEM images of ZnO films made with various gas ratios. The films were deposited at RT without an annealing process onto Pt(111).

SEM images were taken for the investigation of the sputtered ZnO films. Fig. 4.8 shows the images with various gas ratios of the sputtering gas mixture. The sputtering power was fixed at RF 200W, and the total pressure was kept around 8mTorr.

Interestingly, as the oxygen partial pressure in the total pressure increases, the grain size of the film also increases. Further increasing oxygen partial pressure causes a reduction in the grain size. A similar result has been reported by Z. Li [193].

The existence of the optimum oxygen concentration can be explained by the flux behavior of energetic particles in the plasma. Of particular interest in this case is how the bombardment of energetic Ar species affects the reaction and how the re-sputtering effect of energetic oxygen species relates to the nucleation and growth mechanism [190, 191, 193]. According to K. Tominaga [194], as the oxygen partial pressure increases from 0 mTorr, the number of energetic oxygen particles increased at an almost exponential rate. Meanwhile, even though the amount of the Zn species decreases with increasing oxygen concentration, the amount of Zn species arriving at the surface of the substrate is relatively high due to the high bombardment of Ar species on the target in the low oxygen concentration [28, 194]. The large amount of Zn species will enhance the nucleation event at the surface rather than the growth event. Thus, the film morphology is dominated by nucleation, leading to small grain sizes, as shown in the SEM images of fig. 4.8. At this stage, due to the large amount of Zn species, a Zn-rich non-stoichiometric ZnO film will be obtained, leading to poor crystallinity of the sputtered ZnO films [145], as shown in XRD data of fig. 4.7. Additionally, due to a high concentration of Ar, the

incorporation of Ar into the film surface increases, and leads to a decrease in the adatom mobility, deteriorating the crystallinity of the films [67, 190] in this oxygen concentration range. As the oxygen concentration increases to reach the optimum concentration, the number of Zn species keeps decreasing and the number of oxygen species keeps increasing. At a critical point, the output number of Zn species reaches its minimum and the output number of oxygen species becomes constant [194]. Because of the minimum number of Zn species, the amount of Zn species arriving at the surface of the substrate is reduced. Since the reduced amount of the Zn species indicates a low deposition rate, the oxidation reaction of Zn with oxygen species can be enhanced at the surface by the extended time for the reaction. Also, due to the reduction in the amount of Zn species, the growth event may be dominant at the surface rather than the nucleation event. Thus, a large grain size can result from the dominant growth event, and the crystallinity can be enhanced because of sufficient time for the reaction between Zn and oxygen species. By increasing the oxygen concentration further, the number of Zn species is decreased by the oxidation of the target [28, 193] and by replacing the bombardment source from heavy Ar to light oxygen species. However, because the re-sputtering effect of oxygen species becomes dominant in a high oxygen concentration atmosphere, the grain growth is obstructed [190], resulting in the reduction of the grain size, as shown in SEM images.

Because the preferred c-axis orientation can be perturbed by the re-sputtering effect originating from the high flux of oxygen neutrons [195], a lower intensity of XRD was found in the high oxygen concentration region. A way to reduce the re-sputtering effect is to increase the sputtering pressure [196], since the neutral oxygen of the re-sputtering effect results from the neutralization of the negative oxygen upon passing through the discharge [197].

Additionally, comparing with other results, the XRD data show that all ZnO films have only (002) and (004) peaks in the detailed peak investigation, indicating a well-developed c-oriented texture for all the ZnO films in this study. This may be due to the configuration of the sputter system used in this study, which has an angle between the target and the substrate holder. The initiation of the preferred orientation by the oblique vapor incidence to the substrate is faster than that by normal incidence, due to the improved mobility of the incident atoms [198], which may help the incident atoms to find better sites for nucleation. Thus, the formation of a columnar structure is dominant in the films fabricated by this oblique vapor incident method [199]. Furthermore, S. Zhu et al. [182] reported a highly textured structure in ZnO films even on glass substrates by off-axis sputtering deposition.

4.5 Stress analysis with Defects Consideration by Raman Spectroscopy

An understanding of internal stress in the sputtered films is important because this is a crucial factor in determining device performance. Internal stress plays an important role in microelectronics and is related to the mechanical stability and the electrical parameters of devices [145]. Furthermore, in acoustic devices, the stress/strain can affect the acoustic wave velocity. F.J. Hickernell investigated the acoustic wave velocity change in a SAW device made with deposited ZnO films, and reported that a 1.5% change in strain caused a 1.2% change in the velocity, comparing between the strained and unstrained ZnO films [200].

The total stress in the films consists of two individual stresses, internal and thermal stress [201]. The thermal stress originates from the difference in thermal expansion coefficients (TEC) of the film and the substrate. If a ZnO film deposited on a Si wafer is cooled from the deposition temperature, the resulting stress will be tensile because of the difference in the TEC of ZnO ($\alpha_{11} = 6.05 \times 10^{-6} \text{ }^\circ\text{C}^{-1}$ and $\alpha_{33} = 3.53 \times 10^{-6} \text{ }^\circ\text{C}^{-1}$) and Si ($\alpha = 2.5 \times 10^{-6} \text{ }^\circ\text{C}^{-1}$) [202, 203]. The internal stress is generated during film fabrication, and is caused by the buildup of crystallographic imperfections during the deposition process [201]. For film materials with a low melting

point, stress relaxation processes, such as bulk diffusion, can activate at low temperatures, relieving the buildup of crystallographic imperfections. In contrast, when film materials with high melting points are deposited at a low temperature, the internal stress is high because the atoms at the imperfections do not have enough energy to be re-arranged. Thus, the internal stress can be amplified by the buildup of imperfections, and may be able to exceed the thermal stress. Thus, it can be easily seen that the state of stress is closely related to the defect state in the films.

The internal stress in the sputtered films can be varied by modifying other process parameters, such as the substrate, sputtering pressure, gas ratio, and heat treatment [202], all of which will also influence the defect state in the films. J.A. Thornton et al. [204] reported that the internal stress is caused by the enhanced bombardment of energetic particles in the sputtering process. Therefore, a compressive stress in the film can be developed by tailoring the process parameters for enhanced bombardment (e.g. low sputtering pressure and the usage of bias). At low pressures, atomic peening is the cause of the compressive stress in the deposited films. Thus, increasing the sputtering pressure can make the stress transition from compressive to tensile [205].

The stress analysis of the sputtered ZnO films was performed by Raman spectroscopy. The result is shown in fig. 4.9. The procedure of the Raman experiment was the same as used for the CSD ZnO film. For the stress analysis, $E_2(\text{high})$ mode was evaluated and for the reference, Raman data for ZnO single crystal was used.

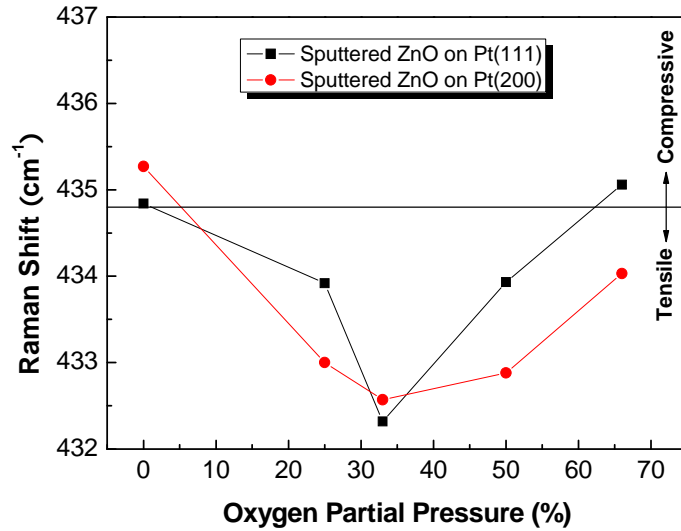


Fig. 4.9 Stress variation with the variation of gas ratio by Raman spectroscopy of ZnO films onto Pt(111)- and Pt(200)-oriented layered silicon wafers.

ZnO films on both Pt(111)- and Pt(200)-oriented layered silicon wafers shows a stress transition from compressive to tensile and back to compressive internal stress as oxygen partial pressure is varied. Since the only variable is the oxygen concentration at a fixed sputtering pressure, the thermal stress can be ignored and only the intrinsic stress is

considered. Because the intrinsic stress is generated by the crystallographic imperfections in the nucleation and growth process [206], the stress transition can be explained by the flux behavior of energetic particles in the plasma.

In the plasma resulting from the ZnO ceramic target, there exists several species, including Ar^+ , Ar^{++} , O^+ , Zn^+ , ZnO^+ , ZnAr^+ , ZnOH^+ , and ZnO^+ [28]. Aita et. al reported a high ratio of Zn^+ and ZnO^+ in the plasma with pure Ar as the process gas [28], indicating the partial decomposition of the ceramic ZnO target and the Zn^+ ion as the dominant particle incident to the substrate. The introduction of the uncombined Zn^+ ion into the film as interstitials may be the source of compressive stress in the film [157, 207], due to the repulsion of the Zn^+ ions from each other. In addition, films grown in an oxygen-deficient atmosphere may be less homogeneous and have more crystallographic imperfections [153], which is the source of the internal stress causing crystallite deformation [154]. Another possible reason for the compressive stress in the low oxygen partial pressure region is the incorporation of Ar species into the film, because the low oxygen region has a high concentration of Ar species. Additionally, the incorporation of Ar species may be enhanced by the oblique symmetry between the substrate and the target used in this study. The oblique incident angle may increase the possibility of the introduction of Ar molecules into the film, causing compressive stress in the films [208-

210]. Thus, the ZnO films deposited in the range from pure Ar atmosphere to low oxygen concentration experienced high internal stress due to Zn interstitials and the incorporation of Ar as shown in fig. 4.9, with correspondingly low intensity in XRD data in fig. 4.7. As oxygen concentration increases, the possibility of the oxidization of Zn^+ with the excess oxygen may result in a more balanced ZnO film stoichiometrically, reducing the internal stress [157] with the crystallinity of the films. In the high oxygen concentration region, the stress becomes compressive. Because the major energetic particle incident to the substrate changes from Ar to oxygen due to the high concentration of oxygen in the plasma [193], the excess oxygen concentration can be incorporated into the films [211], leading to a compressive stress state [212]. This interstitial oxygen results in the crystallite elongation along the c-axis [213], forming the distorted structure. In addition, the oblique incident angle between the target and substrate can provide more oxygen molecules in the films [214], which can be considered as another source for internal stress.

The stress in ZnO film deposited on a Pt(200)-oriented layered silicon wafer is more tensile than that on a Pt(111)-oriented layered silicon wafer. This is similar to the results with the CSD ZnO films, and may be caused by the lattice mismatch at the interface between the film and the substrate.

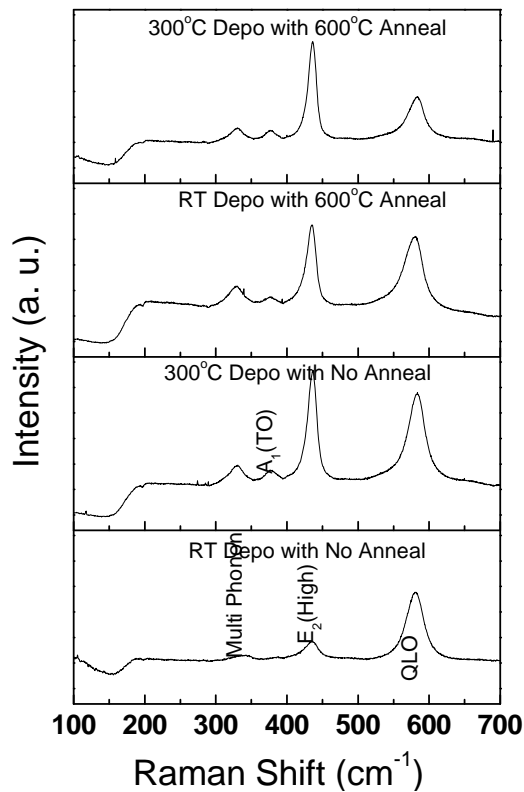


Fig. 4.10 Raman spectroscopy of ZnO films deposited on Pt(111) with Ar:O₂=1:1 and various heat treatments.

The effect of heat treatment was studied by Raman spectroscopy and is shown in fig. 4.10. The film crystallinity was enhanced by heat treatments, substrate temperature, and post-annealing temperature. The improved E₂ mode representing the crystallinity of ZnO is in good agreement with XRD data shown in fig. 4.6. With the detailed investigation of the modes, it was found that the effect of substrate temperature was much more effective than that of post-annealing temperature. As expected, the QLO mode, which is related to the charge carriers, decreased with the heat treatments. This may be

due to the decrease of the charge carrier concentration in the films as a result of the heat treatments.

The stress evaluation with the heat treated films was performed by Raman spectroscopy and is shown in fig. 4.11. As already mentioned, the effect of heat treatments is related to the diffusivity of the absorbed atoms in the film and the oxygen incorporation into the film, which causes stress relief by re-arranging the structural ordering and reducing the crystallographic imperfections in the film. The heat treatments raise both the internal stress and the thermal stress of the films, which are related to the crystallographic imperfections and by the difference in TEC between the film and the substrate, respectively. From the data, it was found that the heat treatments have a trend to lead the films into a state of compressive stress. This may be explained in that the oxygen can be intensively incorporated into the films to oxidize the uncombined Zn interstitial. Furthermore, compared to RT deposition, deposition with an elevated substrate temperature was found to be a much more effective way to incorporate compressive stress into the films rather than using a post-annealing heat treatment. This may be because substrate temperature is more effective in causing the adsorbed species to react with each other during the nucleation and growth processes during film fabrication [215].

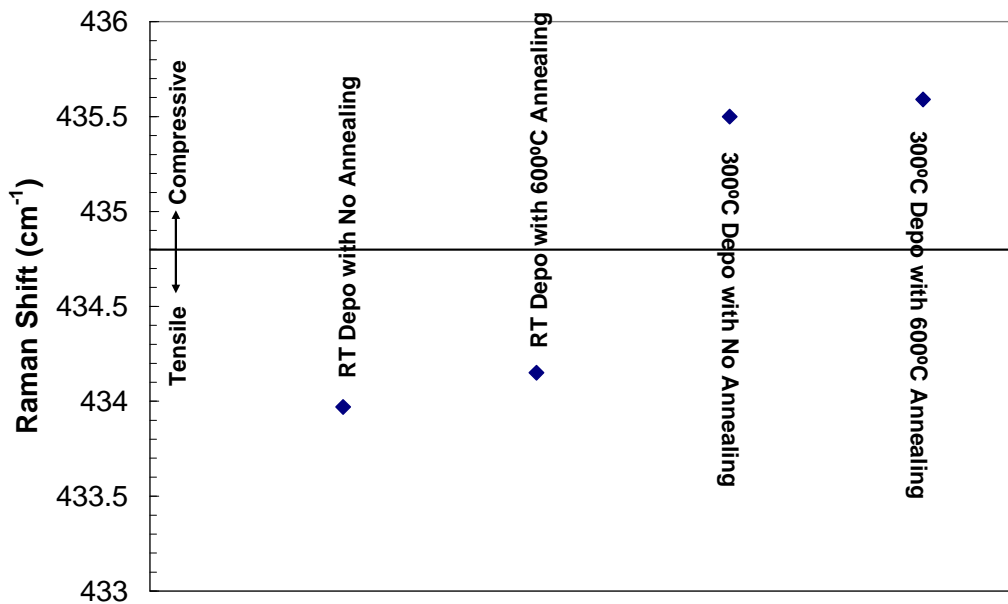


Fig. 4.11 Raman shift for evaluation of stress in ZnO films deposited on Pt(111) with Ar:O₂=1:1 and various heat treatments.

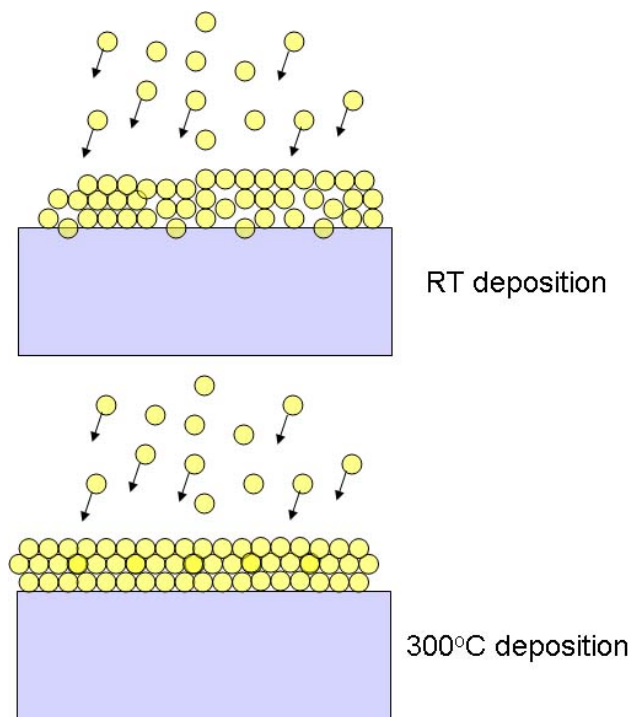


Fig. 4.12 Schematic diagram of the effect of substrate temperature on the bombardment of energetic particles onto the substrate.

M.K. Puchert et al. [216] investigated the stress of ZnO films deposited in a pure oxygen atmosphere, and found the compressive stress in the films to be in a compressive state of stress, which is in good agreement with the result in this study. The compressive stress originated from a high atomic packing density and crystallographic imperfections, which was reduced by annealing to provide thermal energy enough for the imperfections and grain boundaries to move, thereby reducing the free energy in the film.

J.A. Thornton et al. [204] reported that the compressive stress under an Ar atmosphere is not caused by the presence of Ar particles in the film, but instead by the bombardment of the energetic Ar particles from the cathode. Additionally, another source of compressive stress is the incorporation of oxygen particles in the films [201]. Thus, the internal stress is mainly caused by the energetic bombardment of the various species present in the plasma. Therefore, the stress can be relieved by increasing the amount of gas particles in the plasma [217], thereby increasing the collision probability between the species. M.J. Brett et al. [218] investigated the ion bombardment effect on sputtered ZnO film with an electrical bias between the target and the substrate and found that amorphous ZnO films were created by the deteriorated crystallinity due to the ion bombardment of the film. Also, similar degradation by ion bombardment was reported in Ag films [219]. It was also reported that the ion bombardment can sputter the growing films [220].

However, the substrate temperature can deliver the thermal energy to the adatoms to diffuse to more stable sites, leading to the re-ordering of the adatoms. Thus, high quality ZnO films can be obtained by heat treatment, as can be seen from the XRD data. The effect of substrate temperature is shown in fig. 4.12.

4.6 Hardness and Modulus Investigation of ZnO films with Gas Effect

Nanoindentation was performed to determine the hardness and Young's modulus of the ZnO films. Indentations were created by a Nanoindenter XP (MTS) system with a Berkovich-type diamond pyramid. The experiment was done using the static method, and the thermal drift rate was limited to 0.05nm/s. The depth of indentations was 100nm, which is 10% of the film thickness fixed at 1 μ m, to avoid the indentation substrate effect. Each sample was measured with 10 indents for reliable data.

The hardness of sputtered ZnO films had a range from 6.5 to 11.8 GPa, and the modulus ranged from 125 to 220GPa, depending on the oxygen concentration. These values are a little higher than other published results for sputtered ZnO films (8.7 ± 0.2 GPa for hardness and 154 ± 5 GPa for modulus [221]), and much higher than those for single crystal ZnO (5 ± 0.1 GPa for the hardness and 111.2 ± 4.7 GPa for modulus [222]).

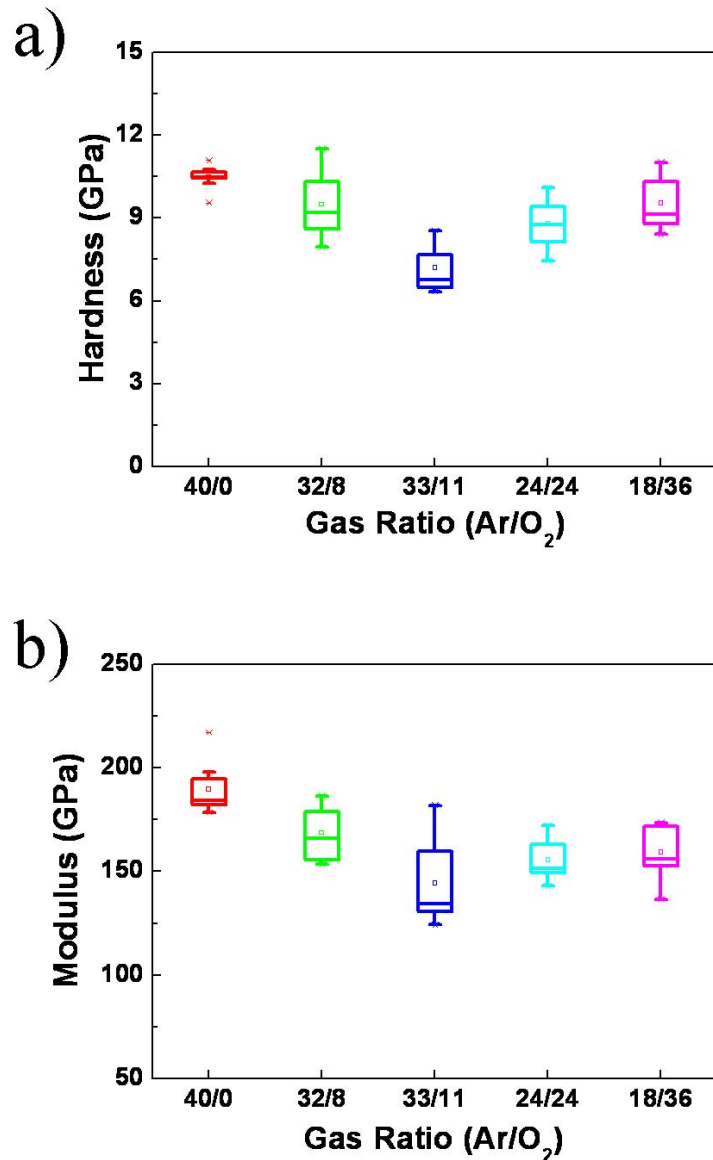


Fig. 4.13 Hardness and modulus of ZnO films deposited at RT with various gas ratios on SiN substrate, measured by Nanoindentation.

The higher values of the sputtered ZnO films compared with the single crystal may be explained by the polycrystalline nature of the sputtered films, where the grain boundaries serve as obstacles for dislocations movement. The hardness and modulus have

similar trends as reported elsewhere [190]. However, a key difference is that they found the hardness and modulus to be not much affected by the change in oxygen concentration, which is different with the results in this study. The results presented here show that the hardness and the modulus were greatly influenced by the oxygen concentration, and this may be because the microstructure of the films has been changed by the oxygen concentration in the plasma. The modulus and the hardness are related to the stress state by the equation below [223]:

$$\sigma = \frac{\kappa\Theta\sqrt{FME}}{(1-\nu)\rho} \dots\dots\dots(4.1)$$

where σ is the stress, and Θ , F , and E are the ion flux, the ion energy, and the modulus of the film, respectively. Thus, the modulus is linearly proportional to the state of stress in the film. Physically, the results can be explained as follows. Films under compressive stress will have resistance against an external force, while films under tensile stress will not. As a result, compressive thin films have been used for protection against fracture [224].

4.7 Conclusion

The film orientation was controlled by the choice of substrate, as shown is shown by the XRD results. However, comparing XRD results between CSD and sputtered ZnO films, the sputtering deposition process is not very sensitive to the substrate effect, while this effect greatly influences the film orientation in CSD ZnO films. From the AFM results, the surface roughness of the ZnO film on Pt(111) deposited at RT is the smoothest, and so is best for acoustic wave device fabrication. The gas type and ratio were investigated, and it was found that the microstructure evolution of sputtered ZnO film is greatly dependent on this parameter. The microstructural evolution was explained by the effect of the sputtering gases on the nucleation and growth process in terms of how the sputtering gases can modify the surface morphology of the films. There was a transition in the grain size of the deposited films, where small grain sizes occurred for high and low oxygen concentrations. Heat treatment during deposition and post-deposition annealing can provide better film microstructure due to the high diffusivity of the adatoms by thermal energy and the reduction of crystallographic imperfections. The stress state in the films varies with the gas ratio, showing a transition from compressive to tensile, and then returning to the compressive stress state in the film as the ratio is

changed further. The transition in stress was explained by the reactive molecules in the plasma (Zn, O, and Ar) as a result of sputtering gas composition. From the nanoindentation experiment, it was found that the hardness and the modulus of the films are also closely related to the stress state in the film.

CHAPTER 5

PZT film fabrication by Chemical Solution Deposition (CSD)

5.1 Introduction

For PZT film fabrication, several methods have been utilized, such as sputtering [225, 226], laser ablation [227], pulsed laser ablation deposition [228, 229], MOCVD [230-232] and CSD (Chemical Solution Deposition) [233]. CSD has been widely used for PZT film fabrication due to some advantages, such as high deposition rate, good composition control, large coverage area at low cost, and low cost for initial capital investment [234]. In contrast, other PVD (Physical Vapor Deposition) methods have low deposition rate, difficulties with the control of film stoichiometry, and compositional inhomogeneities in the film [233]. However, CSD has its own technical issues in that the precursor is composed of several chemicals that have some problems with stability and toxicity [235]. Also, the material properties can be varied within a wide range of the parameters, such as the solution chemistry and heat treatment conditions [236].

The CSD method can be divided to three categories: a sol-gel method based on 2-methoxyethanol (2-MOE, $\text{CH}_3\text{OCH}_2\text{CH}_2\text{OH}$) and alkoxide, a hybrid sol-gel process utilizing an alkoxide complex modified with chelating agents, and a metalorganic deposition (MOD) with metal carboxylate compounds insensitive to water [235]. The MOD method commonly uses large carboxylate compounds and the precursor, which has a composition almost identical to the resulting film composition. Thus, it has the advantage of being less sensitive to water than the sol-gel method [77] due to the carboxylate compounds. Also, since the starting chemicals have a composition very close to that of the resulting film, the process is straightforward and the final film composition can be evaluated before the experiment. However, due to the large shrinkage during the heat treatment, cracks in the film cannot be easily avoided. Also, due to the solution stability, modifying the film properties cannot be easily performed by reactions such as hydrolysis, condensation, and chelating. In the sol-gel method, 2-MOE with alkoxides is the solution most widely used instead of other alcohols, because 2-MOE can reduce hydrolysis sensitivity by an alcohol exchange reaction [235, 237]. Even though this method has some advantages, such as the ability to modify the film properties by the chemical reactions and excellent controllability and reproducibility of process chemistry, its sensitivity to humidity causes problems with solution stability. Because of this issue,

the hybrid sol-gel method, which uses chelating agents to increase precursor stability, has been widely utilized for PZT film fabrication. With this method, the solution is stabilized through the modification of the small, oligomeric species in the precursor by chelating agents, such as MEA, DEA, acetic acid, and acetylacetone. Another advantage is that this method does not need distillation and refluxing processes for the precursor fabrication. Even though the hybrid sol-gel method has some drawbacks, primarily the complexity of the reactions and the aging effect of the precursor, it has been considered to be useful for ceramic film fabrication.

Because the metal alkoxides commonly used in the sol-gel method are sensitive to the humidity, chelating agents have been used to enhance the solution stability by suppressing hydrolysis [238]. (Diethanol)Amine, acetic acid, and acetylacetone (AcAc) are the agents commonly used for ceramic film fabrication by CSD. In this study, AcAc has been chosen as a chelating agent, even though acetic acid has been reported to be an effective agent for low internal stress in the film [239]. For acetic acid, it has been reported that a porous film is obtained as film thickness increases [233], while a smooth surface without cracks or voids can be expected with AcAc, due to its ease of evaporation during heat treatment [240]. While nucleation at both the interface between film and substrate and at the film surface is preferable, the solution chelated with AcAc can

promote nucleation only at the interface [237, 241]. Thus, using AcAc might be more beneficial for the control of the preferred orientation of the films, although a higher pyrolysis temperature is needed due to the single nucleation event, which is not desirable for film fabrication [242].

The configuration of the substrate surface plays a large role in the film orientation. K.S. Hwang et al. [243] reported that epitaxial PZT films were found on SrTiO₃ and LaAlO₃, while polycrystalline and amorphous structured PZT films resulted from Sapphire and Si wafer substrates. (100), (110), and (111)-oriented SrRuO₃ substrates were used to find the effect of substrate orientation on PZT films [244]. This was explained by the minimization of lattice misfit via lattice mismatch. Another consideration concerning the substrate is that PZT film cannot be deposited directly onto a silicon wafer due to the reaction between Pb and Si at the elevated temperatures. A layer to act as a diffusion barrier for the atoms is needed to prevent the reaction [245]. The buffer layers commonly used for epitaxial PZT films, which show better quality than the textured polycrystalline PZT, are TiO₂ [75, 245], ZrO₂ [246], MgO [10, 228], LaAlO₃ [247], and RuO₂ [248]. The film orientation is also greatly dependent on the buffer layer, because the growth of PZT films has been found to be controlled by the nucleation process [248].

Heat treatment is also one of the important issues for film orientation. A report showed that a fast heating rate can orient the film texture to PZT(111), a moderate rate to Pt(100), and a low heating rate will promote a random orientation in the film [249]. The heat treatment can modify the solution chemistry [250] as well, which causes a change in the film orientation [251, 252]. Pyrolysis temperature and time have been enthusiastically investigated as a factor to determine film orientation [253]. Heating rate [249] and calcination atmosphere [240] have also been discussed in the literature as other parameters affecting the orientation of the film.

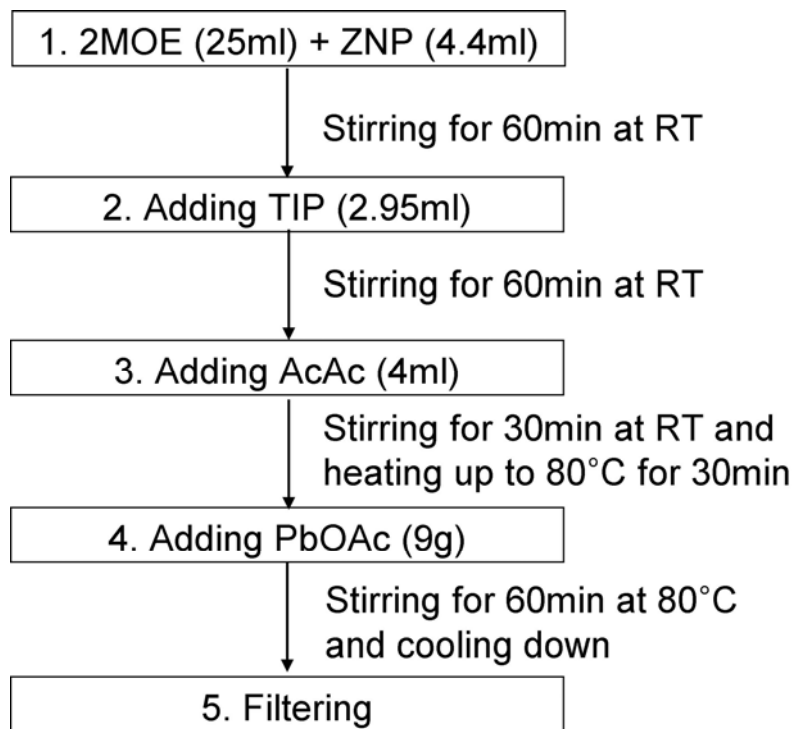


Fig. 5.1 Fabrication procedure of PZT precursor.

5.2 Detailed Experiment

The precursor for PZT films consists of lead acetate trihydrate (Aldrich, PbOAc, $\text{Pb}(\text{CH}_3\text{CO}_2)_2 \cdot 3\text{H}_2\text{O}$), titanium isopropoxide (Aldrich, TIP, $\text{Ti}[\text{OCH}(\text{CH}_3)_2]_4$), and zirconium propoxide (Aldrich, ZNP, $\text{Zr}(\text{OCH}(\text{CH}_3)_2)_4$). 2-methoxyethanol (Aldrich, 2-MOE, $\text{CH}_3\text{OCH}_2\text{CH}_2\text{OH}$) was used as a solvent. Additionally, acetylacetonone (Aldrich, AcAc, $\text{C}_5\text{H}_8\text{O}_2$) was employed as a chelating agent. Thus, two types of precursor, with Acetylacetonone (labeled as WAC) and without Acetylacetonone (labeled as WOAC), were used to examine the effect of the chelating agent on the preferred orientation of PZT films. The precursor fabrication steps are shown in fig. 5.1. First, ZNP was dissolved in 2-MOE, and the mixed solution was stirred for 1 Hr at RT. Then, TIP was added to the mixed solution. Due to the lower reactivity of ZNP in 2-MOE than TIP in 2-MOE, ZNP was mixed with 2-MOE prior to TIP. After 1 hr. stirring at RT, AcAc was added to the mixed solution for the AcAc chelated solution. In the precursor fabrication, the source for the water molecule is PbOAc, which has 3 water molecules to one PbOAc molecule. Thus, prior to adding PbOAc, AcAc was added to the solution to have the chelating agent effect on the precursor. The final concentration of PZT solution is 0.5M. The ratio between Zr to Ti was set to between 0.53 and 0.47, which is the composition of the MPB

(Morphotropic Phase Boundary). 10 mol% excess lead sources were included in the precursor to compensate for PbO volatilization during heat treatment. The Pb concentration must be exactly controlled, as the second phase of PbO may be obtained at the high concentration of Pb, and the pycnophore phase at the low concentration of Pb [254]. After aging the precursors for 72 hours, the solutions were dropped onto the substrates, which were Pt(111)- and Pt(200)-oriented layered silicon wafers. The dropped precursors were spun by spin coater at 3000rpm for 30sec, which gave about 90nm of thickness per each layer. After 72 hours, the solutions were clear with no precipitates visible.

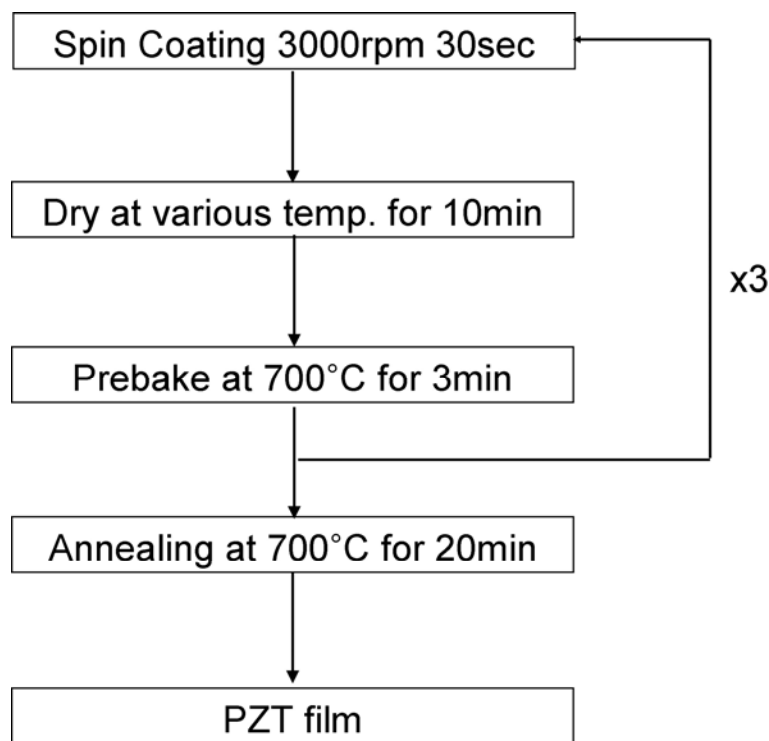


Fig. 5.2 Experimental procedure diagram of PZT film fabrication by sol-gel.

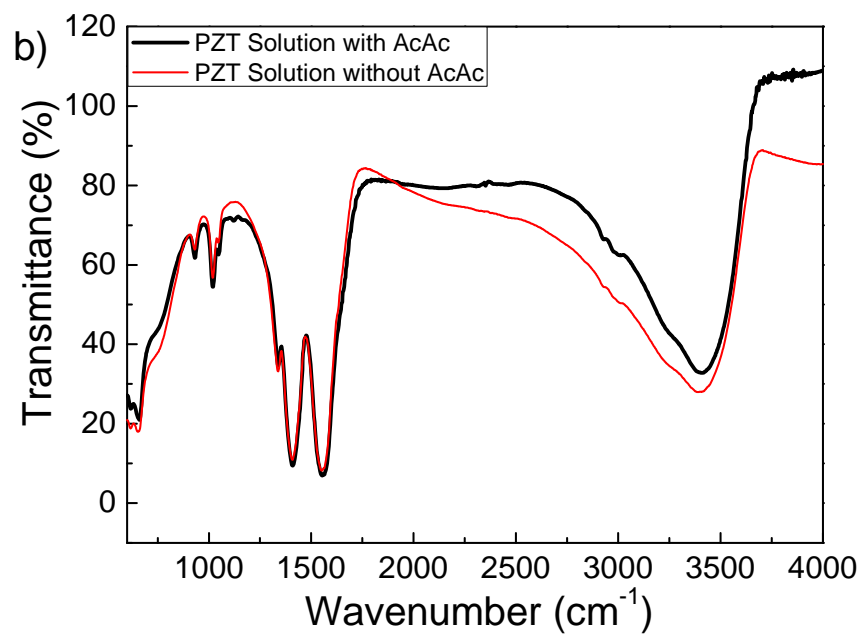
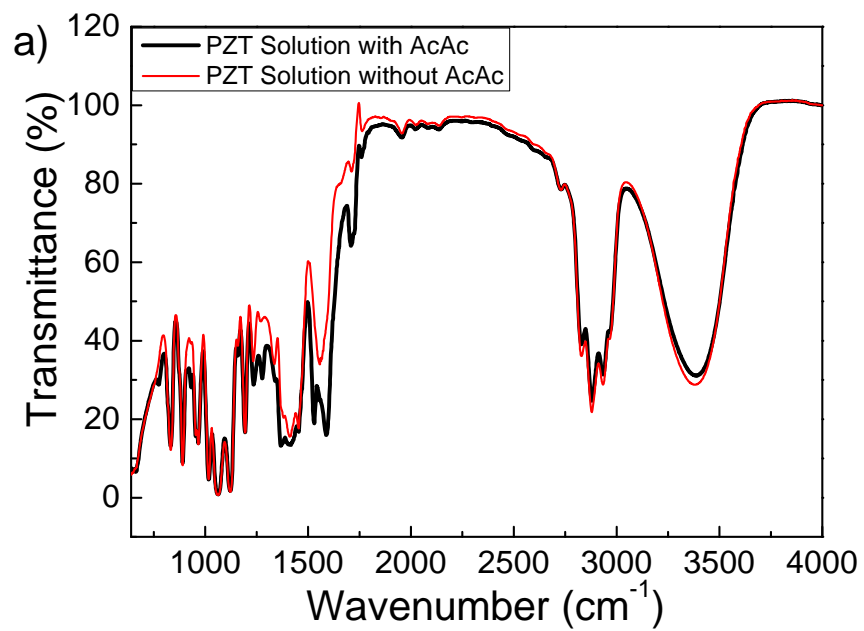


Fig. 5.3 Infra-red spectra of PZT precursors with/without AcAc.

- a) as synthesized, but aged over 72 hours at RT.
- b) heat treated below 110°C for 12 hours.

The heat treatment of films was performed at 250-450°C for 10 min, and then at 700°C for 10 min. This process was repeated three times. Finally, all the PZT films were annealed at 700°C for 20min to ensure crystallization. The final film thickness was measured to be 270 nm. The schematic of the fabrication protocol is shown in fig. 5.2.

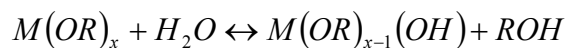
5.3 Precursor Study by Solution Chemistry

The hybrid sol-gel method with acetylacetonone has been used for this study, and it has been found that the chelating agent not only affects the solution stability, but also influences the film orientation with respect to the substrate type, thus it plays an important role in determining the film properties. Also, the pyrolysis temperature effect will be discussed.

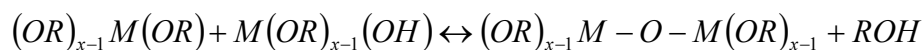
The precursors of PZT were analyzed by FTIR to investigate the chemical bonding in the solutions. Fig. 5.3(a) shows the data for the as-fabricated solution aged for over 72 hours, and fig. 5.3(b) shows the results when the aged solutions were heated up to 110°C for 12 hours. The precursor with AcAc transformed to a brownish hard gel after the heat treatment, and the precursor without AcAc transformed to a cream-colored solid. The precursors still in solution were directly measured by FTIR and the heat treated

precursors were crushed with a mortar and pestle, and mixed with KBr powder. The mixture was shaped into a pellet by a press to be compatible with the FTIR equipment. The KBr powder pellet was first measured by FTIR, and then this data was subtracted from the data for the mixtures. The scanned range was 600cm^{-1} to 4000cm^{-1} .

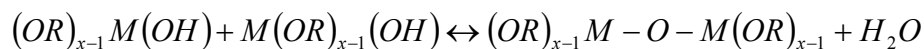
The CSD (chemical solution deposition) process, also called the sol-gel process, uses a colloidal solution of a metalorganic, $M(OR)_x$ and a metalorganic-oxygen-metalorganic, $(OR)_{x-1}M-O-M(OR)_{x-1}$. The solution chemistry is controlled by hydrolysis and condensation reactions. For the hydrolysis reaction,



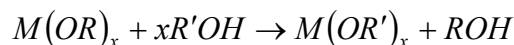
for the condensation reaction by alcohol elimination,



and, for the condensation reaction by water elimination,



M is the metal and R is the alkyl group. During the hydrolysis reaction, one of the alkoxide groups, (OR) , is substituted by an hydroxide, (OH) , to release an hydroxyl group. The hydroxyl group is readily reacted with other hydrolyzed molecules and/or alkoxides, forming a $M - O - M$ bond from a condensation reaction. These two reactions are reversible, and if the equilibrium between the reactions is reached, then the gelation of the solution will not occur under stable conditions. In addition to these reactions, the solvent, 2-MOE, can act as a chelating agent by the alcohol exchange process below:



Metal methoxyethoxide, $M(OR')_x$ can be formed by the reaction, and is less sensitive to the hydrolysis and will improve the stability of the solution. In the solution system in this study, AcAc was used as a chelating agent, and the resulting chemical reaction is:



By this reaction, metal acetylacetonate can be formed, and will make the solution stable against humidity from the environment.

From the FTIR data of the as-synthesized solution in fig. 5.3 (a), the C-H bending

modes were obtained in the range of 750cm^{-1} to 1000cm^{-1} , and a peak of the carbonate group (CO_3^{2-}) was found at 832cm^{-1} from the lead carbonate [255]. In the range of 1234cm^{-1} to 1017cm^{-1} , C-O stretching bands from the ether and alcoholic functional groups exist [255, 256]. At 663cm^{-1} and 1063cm^{-1} , M-O (metal-oxygen) bonding was found [257]. Peaks at 1280cm^{-1} , 1531cm^{-1} , and 1589cm^{-1} in the precursor with AcAc originate from the C-CH₃, C-C, and C-O bonds in the AcAc, and are not present in the precursor that has no AcAc [258]. At 1455cm^{-1} and 1560cm^{-1} , the vibrations of COO-bonding due to the bidentate acetate ligands were observed in symmetric and asymmetric stretch, respectively [255, 256, 259], indicating the bridging configuration for the acetate group [260]. A peak at 1710cm^{-1} is indicative of the ester [257], which is a byproduct of the condensation reaction shown in above. In the range of 2839cm^{-1} and 2968cm^{-1} , the peaks are related to C-H stretching vibrations [255, 256]. The peaks observed at 2879cm^{-1} and 2935cm^{-1} result from residual 2-MOE remaining in the precursors after synthesis. The broad band around 3300 to 3400 cm^{-1} is related to the O-H stretching vibration from the hydroxyl group of alcohol or water as a by-product of the condensation reaction [257], and not from the residual solvent originating from the lead-zirconium-titanium alkoxide [255].

The IR data of the heat treated precursor is very different from that of the

solution precursor, as can be seen from fig. 5.3 (a) and (b). Most C-H and C-O bonds disappear due to the heat treatment [261], but the O-H bond at 3380cm^{-1} still exists, indicating of the presence of metal hydroxide after heat treatment [256, 262]. The peaks in the range of 1300 to 1558cm^{-1} , which originate from carbonate and were present in the data of the liquid precursor as well, become easily distinguishable. Their presence can be explained by the decomposition of the acetate and the CO_2 absorption [256], which disappeared above 300°C . Another difference in comparison with the precursor without AcAc is that a peak at 1378cm^{-1} was found in fig. 5.3 (a), which is related to the bonding of the isopropoxide and AcAc [258], and indicates that the PZT precursor with AcAc is chelated by AcAc [237]. Furthermore, M-O bonds at 620cm^{-1} and 660cm^{-1} due to stretching vibration become very visible, and the peak at 2351cm^{-1} due to CO_2 absorption was found [255] in the precursor with AcAc.

5.4 Film Orientation Evolution by Nucleation and Growth Mechanism

The film orientations were evaluated by XRD, with the results shown in fig. 5.4, and 5.5. This data does not show the pyrochlore phase in the film, which has been reported to be found around 29° in x-ray diffraction [263]. Fig. 5.4 shows PZT films that

were fabricated with pyrolysis temperatures between 250-450°C on a (200) oriented Pt layer on a TiO₂/SiO₂/Si wafer. All PZT films show a (100) oriented structure, regardless of different pyrolysis temperatures and the presence of the chelating agent.

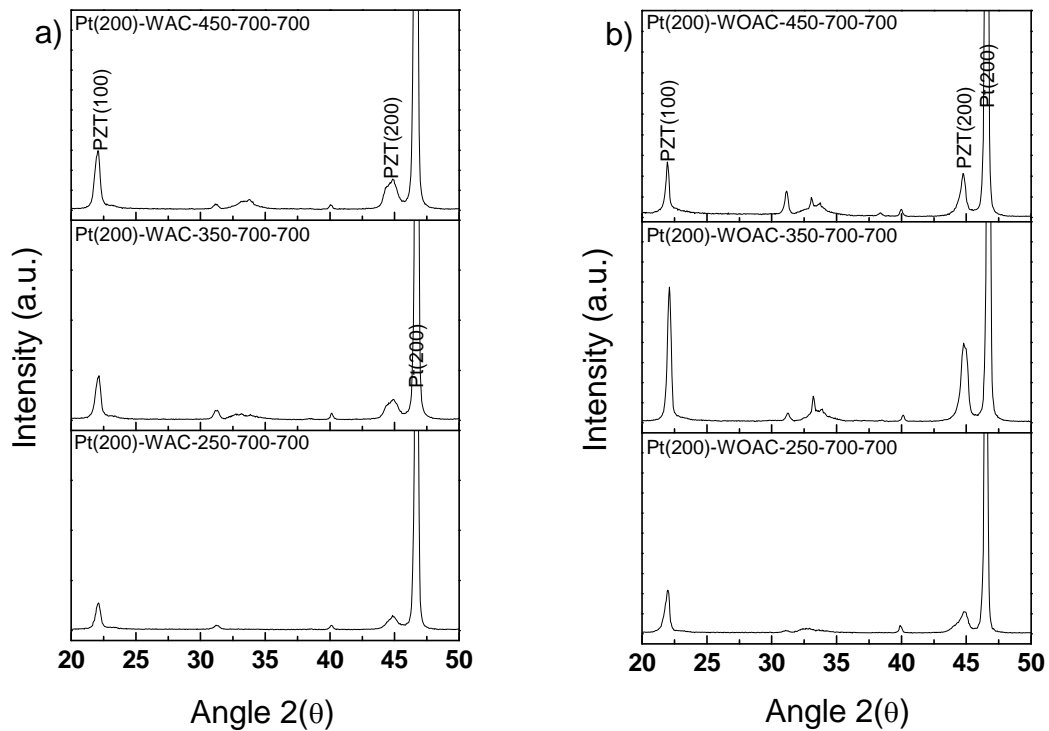


Fig. 5.4 XRD results of solution derived PZT thin films on Pt(200)/Si substrate a) with acetylacetone, and b) without acetylacetone.

PZT films were deposited on (111)-oriented Pt-layered silicon wafers, and the XRD results are shown in fig. 5.5. Compared with fig. 5.4, PZT films fabricated at a low pyrolysis temperature of 250°C possess a <111> oriented structure, while PZT films fabricated at higher pyrolysis temperatures have a trend towards a <100> textured

structure. Interestingly, with the 350°C pyrolysis temperature, PZT film fabricated by the precursor with AcAc shows a $\langle 111 \rangle$ textured structure, while PZT film without the AcAc chelating agent has a $\langle 100 \rangle$ oriented texture.

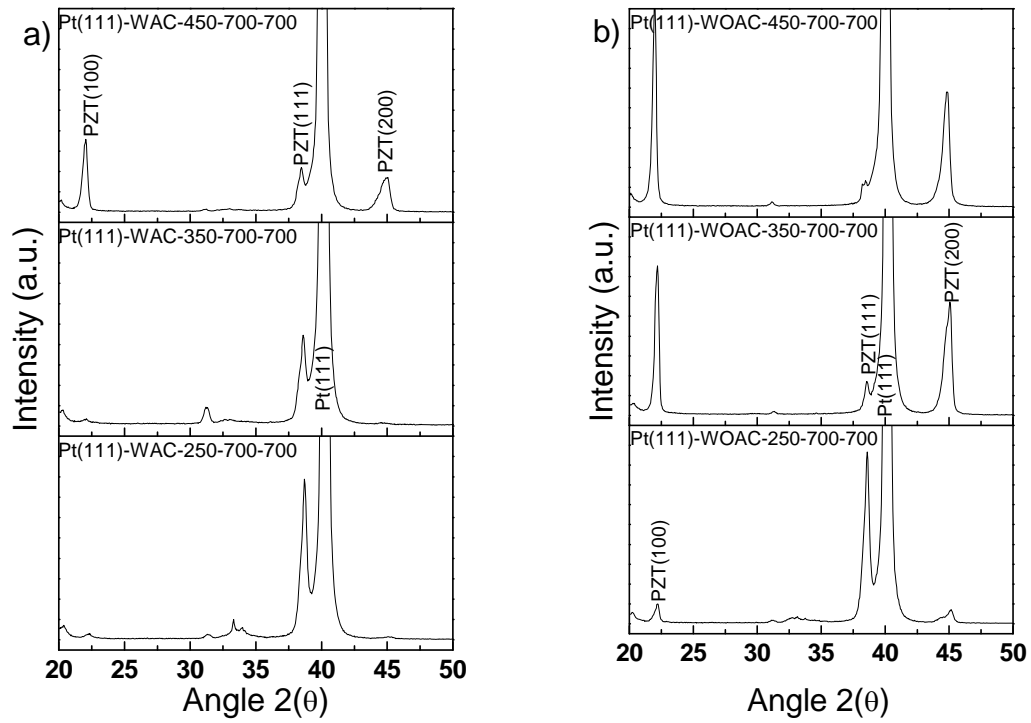


Fig. 5.5 XRD result of solution derived PZT thin films on Pt(111)/Si substrate a) with acetylacetonone, and b) without acetylacetonone.

In this study, PZT films have been investigated for use in the application of acoustic wave devices. The crystal orientation depends on many factors, such as solution chemistry, surface configuration of the substrate, and heat treatment scheme. The XRD graphs clearly show the effects of the substrate and the chelating agent. There are two

primary mechanisms that determine the preferred orientation of the film. One is lattice matching, in that the nucleation and growth of the film and the resulting texture can be controlled by the surface configuration of the substrate and the interfacial properties. Another is low surface energy, which may be considered as the nucleation and growth direction of the film. For the lattice matching effect, there are several reports that PZT growth is controlled by nucleation and not by self-texture growth. This can be used to facilitate the textured and columnar structure by controlling the nucleation event with the appropriate substrate [243, 245] or with an electrode [264]. The lattice matching effect has been used to fabricate PZT films oriented in the $\langle 100 \rangle$ direction by using substrates which have same surface configuration with the film [265], and by using seed layers which have same crystal structure of the films [240, 246, 266, 267]. However, G.J. Norga et al. [268] reported that the preferred orientation is not solely dependant upon the lattice matching effect. They found that $(\text{LaZr})_2\text{O}_7$ had a (111) oriented texture on $\text{SrTiO}_3(100)$, even though $(\text{LaZr})_2\text{O}_7(111)$ had not matched with $\text{SrTiO}_3(100)$, which may be explained by the minimum surface energy effect. R. Kurchania et al. reported that the PZT (111) texture decreased with the increase in the film thickness [13], which may also be explained by this effect. The (100) plane of PZT has the minimum surface energy, so that the crystal growth in this direction is preferable [253].

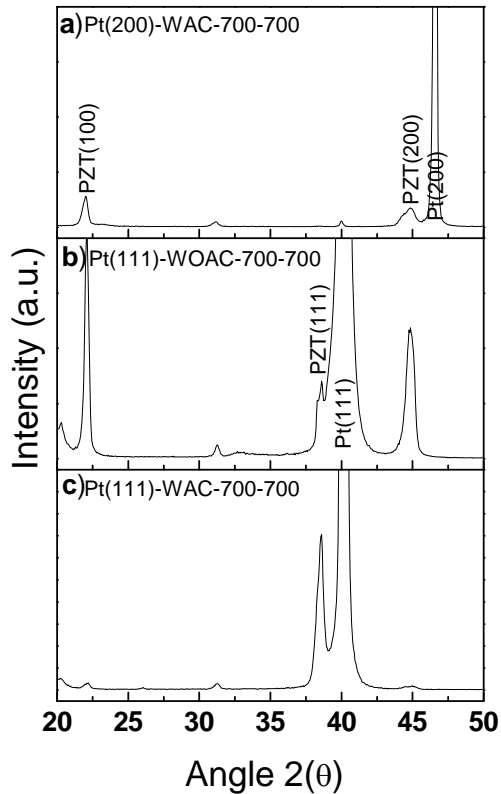


Fig. 5.6 XRD results of PZT films with a heat treatment of 700°C.

Fig. 5.4 shows the XRD results from PZT films on (200) oriented Pt substrates, and all of the PZT films have a tendency towards a (100) preferred orientation. This can be explained by both the lattice match and minimum surface energy effects. The (100) orientation of PZT film is affected by the surface configuration of Pt (200), which is matched well with the PZT (100), which is also the minimum surface energy plane in PZT. Thus, PZT film might have a preferred orientation of (100) regardless of the heat treatment. Also, this could be the reason for the behavior of the PZT film that was

subjected to the 700°C annealing temperature without pyrolysis heat treatment, as shown in fig. 5.6.

In the case of PZT films on the (111) oriented Pt layer, the preferred orientation varies with the heat treatment, as shown in fig. 5.5. From the detailed investigation of fig. 5.5, it is found that the PZT films that have undergone the 250°C pyrolysis heat treatment, both with and without AcAc, shows a (111) preferred orientation. For the 350°C pyrolysis heat treatment, the PZT film with AcAc shows a (111) preferred orientation, while the PZT film without AcAc shows a (100) preferred orientation. PZT films with the 450°C pyrolysis heat treatment show (100) preferred orientation in both films with and without AcAc.

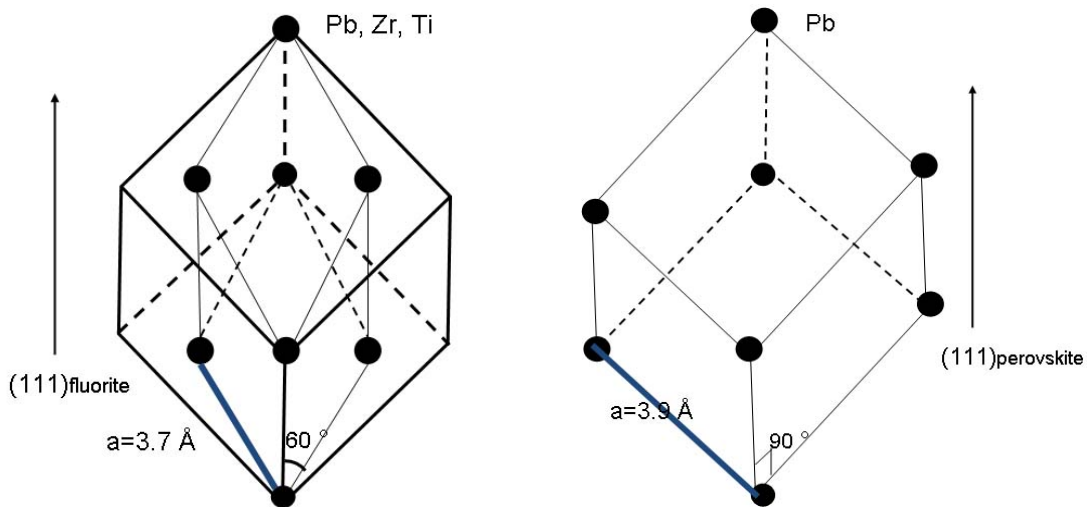


Fig. 5.7 Fluorite structure (left) and perovskite structure (right).

G.J. Norga et al. studied the film orientation of solution derived PZT films, and found that the nucleation of the perovskite structure can be enhanced by the formation of a fluorite structure [268], occurring generally at lower temperatures. Perovskite has the formula $\text{Pb}_{2+x}\text{Ti}_{2-x}\text{O}_{7-y}$, which is an oxygen deficient structure [269]. Thus, its formation was thought to happen in a low oxygen atmosphere, and the low oxygen atmosphere was thought to be achieved by the burn-off of the residual organic in the initial stage of the pyrolysis[262]. If the pyrolyzed film includes an (OH) group after low temperature pyrolysis, then it can make the atmosphere oxygen deficient during annealing, which can promote a PZT(111) orientation by forming the fluorite structure at the interface. And, if the pyrolyzed film has an equiaxial (100) perovskite structure and/or amorphous pyrochlore phase in the case of high temperature pyrolysis, the final orientation will trend towards (100) in PZT films, which is the lowest surface energy plane [270]. Therefore, the solution chemistry greatly influences the orientation evolution of PZT films. Additionally, the pyrochlore structure of formula PbTiO_3 may occur at a relatively high temperature, but with heavy lead loss during heat treatment [269]. The role of the oxygen deficient fluorite structure in the orientation of PZT films can be attributed to the fluorite lattice structure of the face-centered orthorhombic unit cell, because the transformation of fluorite to perovskite can be accomplished by just a little angular distortion, as shown in

fig. 5.7. Thus, the formation of a fluorite structure can lead to obtaining well-crystallized perovskite at a low temperature heat treatment, because of the reduction in the driving force for producing the perovskite structure as opposed to going through a direct transformation [271].

Both PZT films, with and without AcAc, on Pt(111) layered substrate at 250°C have (111) oriented structure. This can be explained in that, after the 250°C pyrolysis, these films may have a well-crystallized fluorite structure caused by the oxygen deficient atmosphere due to the burn-off of the organics [270]. Because the fluorite structure has the lowest surface energy in the (111) plane [272] and Pt(111) has similar configuration to the fluorite structure, the (111) oriented fluorite structure will be formed on the Pt(111) substrate. Because the fluorite structure is metastable, the transformation from fluorite to perovskite is so fast as to be able to trap pores with little angular distortion [273]. The amount of the fluorite structure was greatly reduced in PZT annealed at 700°C, even compared to 30sec and 60sec annealing times [274]. Thus, (111) oriented perovskite PZT will evolve from the fluorite structure at the interface between the PZT and Pt layers.

PZT films, both with and without AcAc, on the Pt(111) layered substrate at 350°C show a mixture of PZT(111) and PZT(100). However, the PZT film with AcAc shows a (111) orientation dominant structure, while PZT without AcAc shows a (100)

orientation dominant structure. It was found that there was amorphous pyrochlore and some perovskite structure present with the 2min, 350°C heat treatment in the pyrolyzed film [270], and, from this structure, a mixed orientation of (111) and (100) PZT was obtained. However, the PZT film with AcAc shows a much stronger (111) peak intensity, which may be explained in that AcAc has an important role in the orientation evolution. This may due to the strong bonding in the PZT precursor resulting from the addition of the chelating agent. The strong bonding can trap more residual organic in the films, and the large amount of the residual organic can facilitate the orientation evolution to (111) in PZT.

PZT films on Pt(111) have been oriented to (100), irrespective of the presence of a chelating agent. It is likely that the 450°C pyrolysis temperature can create the pyrochlore structure in the pyrolyzed film [270], because the pyrochlore structure is a stable phase in the temperature range of 350-500°C [242], and this is a high enough temperature to remove all residual organic in the film. During the annealing stage at 700°C, the heat treatment provides enough thermal energy for the atoms to diffuse over a relatively long range. The atoms in the film are then more likely to find positions to minimize the interfacial energy with the substrate. The (100) plane of PZT has the

minimum surface energy where the atoms can be arranged in the plane, and the films will tend to grow in the (100) oriented texture.

A more simplified heat treatment scheme was employed to determine its effect on the films. PZT films were deposited onto (111) and (200) oriented Pt layered silicon wafers without a pyrolysis heat treatment, as shown in fig. 5.6. The films were then subjected to a one step heat treatment at 700°C. XRD results show the chelating effect in the PZT film on the Pt(111) substrates. When the films are subjected to such a high temperature, they experience a high heating rate. For the PZT film on Pt(111) without AcAc, the high heating rate promotes the direct transformation to the perovskite structure, which is the stable phase at high temperatures. On the contrary, the PZT film on Pt(111) with AcAc can delay the transformation due to the strong bonding of the chelating agent. By adding the chelating agent, the transformation delay can give time for the fluorite structure to develop. However, the high heating rate can also provide a much more oxygen-deficient atmosphere, which can facilitate the formation of the fluorite structure. Concerning the PZT films on Pt(200), both with and without AcAc, the (100) peak intensity increases with increasing pyrolysis temperature. This means that increasing pyrolysis temperature can reduce the amount of the residual organic in the film, which can make PZT films oriented to (100) easily. On the other hand, the fluorite

structure may not be favored because of the lattice mismatch between the fluorite and Pt(200). This will warrant further investigation in the future.

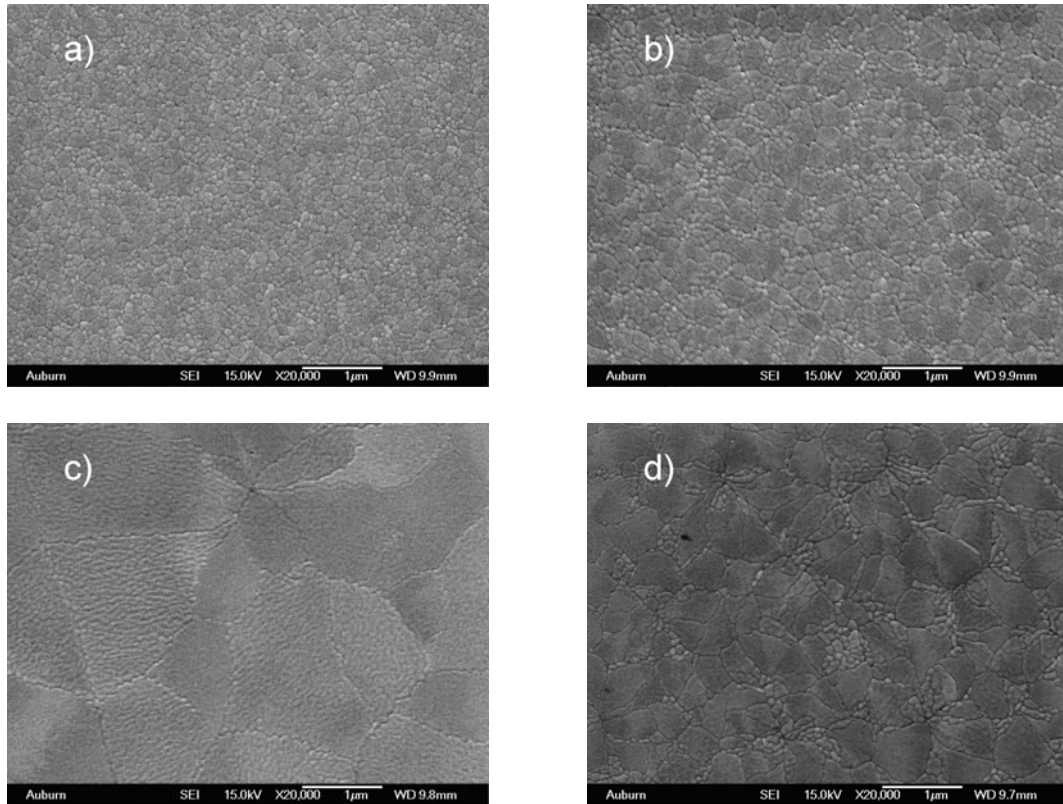


Fig. 5.8 SEM images of PZT films derived by the solution with AcAc on Pt(111) with different pyrolysis temperature and 700°C annealing temperature.

- a) 250°C
- b) 350°C
- c) 450°C
- d) 700°C heat treatment only

The surface SEM images of PZT films are shown in fig. 5.8. The grain size has increased with the pyrolysis temperature. Note that the PZT film pyrolyzed at 450°C has a large grain size and a (100) oriented texture as verified by XRD measurement, shown in

fig. 5.5. By considering the large size of the grains, it may be construed that the atom mobility was high enough for the atoms to have the (100) oriented texture because of the minimum surface energy. Comparing this with the PZT film heat treated at 700°C, the film with 700°C heat treatment shows a smaller grain size than that of the film pyrolyzed at 450°C. This is because, in the case of the 700°C heat treated PZT, the AcAc enhanced the heterogeneous nucleation at the interface, which was facilitated by the formation of the fluorite structure. The fluorite structure can reduce the energy barrier for nucleation in conjunction with the high heating rate. The rosette-like texture was also found in other studies[243, 249], and is considered to be the perovskite PZT phase annealed at high temperature.

In fig. 5.9, SEM images of PZT films are shown. It can be seen that the grain sizes of PZT films derived by the solution with AcAc are smaller than that of PZT films derived by the solution without AcAc. Also, the grain sizes of PZT films on the Pt(111)-oriented layered silicon substrate are larger than those on the Pt(200)-oriented layered substrate. This may be due to the formation of the fluorite structure on the Pt(111) surface, because the fluorite structure has a similar surface configuration to Pt(111). Then, on the Pt(111) surface, the nuclei of the fluorite structure with (111) orientation can easily grow, and proceeds to the growth stage, while on the Pt(200) surface, the nucleation may be

hindered by the strain energy due to the lattice mismatch. On the Pt(111) substrate, nucleation is the dominant stage, while on Pt(200), the growth stage is dominant.

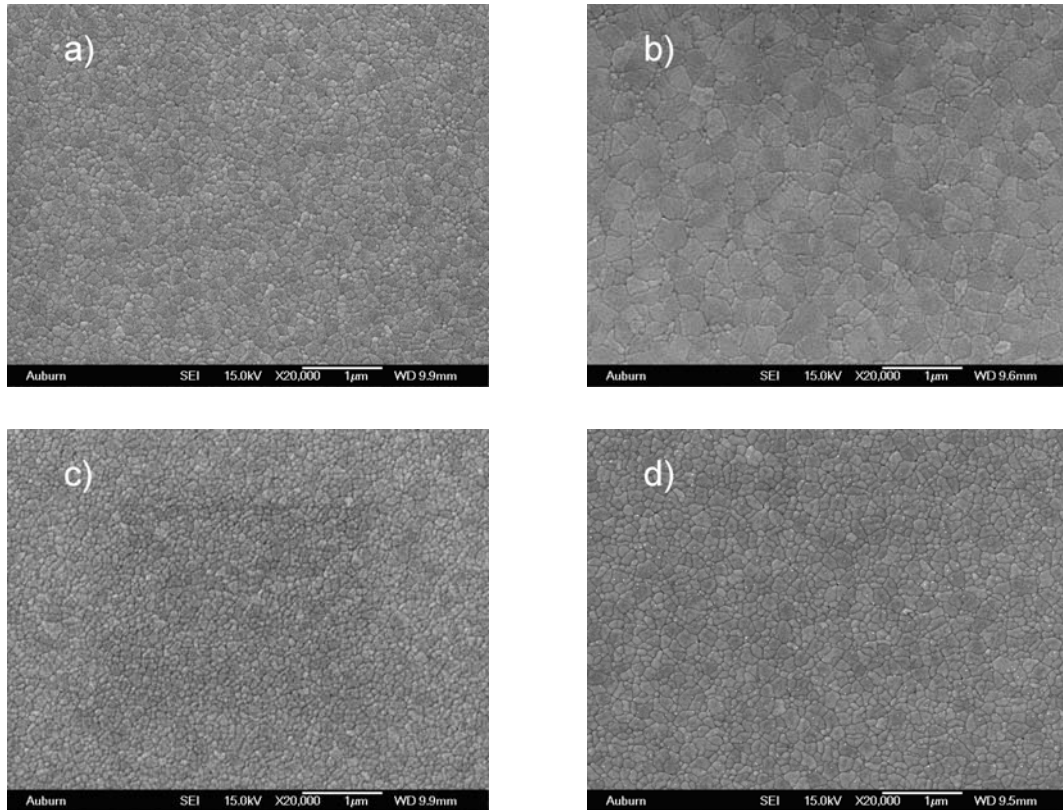


Fig. 5.9 SEM images of PZT films with 250°C pyrolysis and 700°C annealing.

- a)** on Pt(111) derived by the solution with AcAc
- b)** on Pt(111) derived by the solution without AcAc
- c)** on Pt(200) derived by the solution with AcAc
- d)** on Pt(200) derived by the solution without AcAc

Comparing PZT films on Pt(111) with and without pyrolysis heat treatment (fig. 5.9(b) and 5.10, respectively), the PZT with only the one step heat treatment shows many voids on the surface, which is caused by rapid evaporation from the high heating rate.

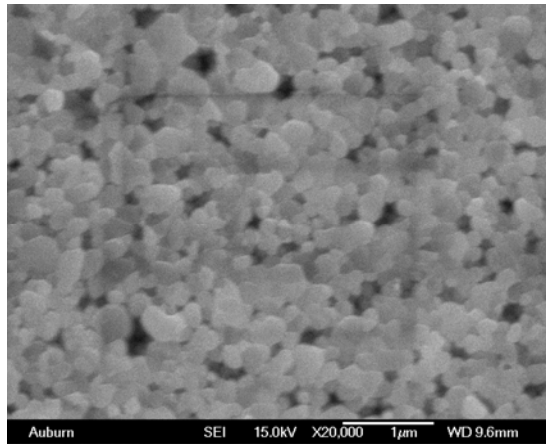


Fig. 5.10 SEM image of PZT film derived by the precursor without AcAc and with only the 700°C heat treatment on Pt(111).

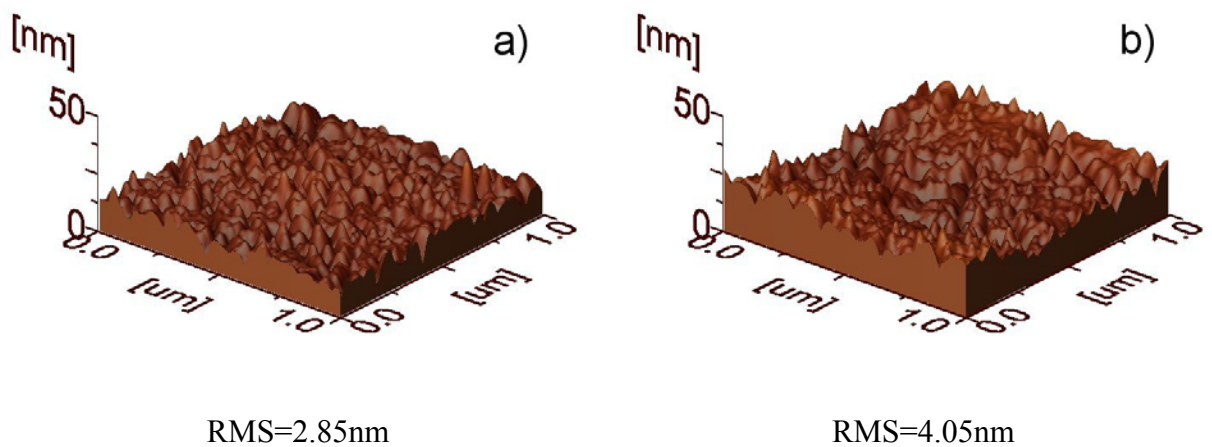


Fig. 5.11 AFM images of PZT films with 250°C pyrolysis and 700°C annealing
a) on Pt(111) derived by the solution with AcAc
b) on Pt(111) derived by the solution without AcAc

Fig. 5.11 shows AFM images with RMS values for the PZT films shown in fig. 5.9. Thus, the heterogeneous nucleation from the interface by the formation of the fluorite structure can facilitate the smooth surface of PZT films., And so, it appears that PZT film derived by the solution with AcAc on a Pt(111) substrate can be used for acoustic wave

devices, because the acoustic wave propagates the signal at the film surface, and the roughness of the film can greatly affect the acoustic wave propagation.

5.5 Raman Characterization of Film Stress

Raman spectroscopy has long been considered to be a powerful technique for assessing the properties of ferroelectric films, such as domain and grain orientation, phase transition [275], stress state [276], and the crystallization process [277]. Compared with other techniques, such as X-ray [278, 279], and neutron diffraction [280], Raman spectroscopy has the advantages of being simple, fast, and non-destructive. From the phase diagram of PZT in fig. 2.8, it has been generally accepted for several decades that PZT at its MPB (Morphotropic Phase Boundary) consists of tetragonal and rhombohedral structures. However, in addition to these structures at MPB region, a monoclinic structure has been identified [281, 282] and is considered to be a second-order transitional bridge between the tetragonal and rhombohedral structures. The crystallographic relationship between the monoclinic and tetragonal structures in PZT films at the MPB composition is that a_m and b_m lie along the $[110]$ and $[1\bar{1}0]$ directions of the tetragonal structure, and c_m lies along the $[001]$ direction of the tetragonal structure with an angle of 90.5°

between a_m and c_m . In the relationship between the monoclinic and rhombohedral structures, the [001] direction of the monoclinic structure lies along the [111] direction of the rhombohedral structure. Thus, the condensation in the directions of [110] in the tetragonal structure and [111] in the rhombohedral structure can represent the monoclinic distortion, and this monoclinic structure has been considered to play a role in dielectric, piezoelectric, ferroelectric, and high electromechanical properties of PZT films at the MPB composition [283, 284]. Raman spectra are determined by the crystal symmetry and the scattering geometry in the experiment. Thus, prior to the experiment, it is important to obtain the information on the crystal structure in order to expect the plausible modes of the crystal by the selection rule. PZT films at the MPB composition are expected to have tetragonal, rhombohedral, and monoclinic structures, and above the Curie temperature ($T_c = \sim 360^\circ\text{C}$ [19]), all structures transform to Cubic structure, which belongs to space group $O_h^1(Pm3m)$ [285]. The degree of freedom of the cubic unit cell of PZT is $(3N-3) = 12$, thus a total of 12 optic modes can exist, which are distributed as $3T_{1u} + T_{2u}$. A single triply degenerate T_{2u} is a silent mode, because it is not Raman active or infrared active. The three triply degenerate T_{1u} modes are infrared active, but not Raman active. As the cubic structure is cooled down below T_c , it transforms into other structures, such as rhombohedral ($C_{3v}^6(R3C)$ or $C_{3v}^5(R3m)$), tetragonal structure ($C_{4v}^1(P4mm)$), and

monoclinic ($C_s^3(Cm)$ or $C_s^4(Cc)$). In the case of the transformation from the cubic to the tetragonal structure, which has $C_{4v}^1(P4mm)$ by cooling, T_{1u} of cubic structure transforms to A_1+E of tetragonal structure, which are infrared and Raman active. Thus, by the long range electrostatic force [286], the modes can have a polarization perpendicular to the propagation direction (TO mode) and can have a polarization parallel to the propagation direction (LO mode). T_{2u} splits to B_1+E [285]. Both are infrared active, but the B_1 mode is silent for Raman. However, the splitting in mode frequency for both modes is too small to detect, and in most cases, they have been labeled as a silent mode in one mode frequency. Due to 3 T_{1u} and 1 T_{2u} , and the split of A and E modes into TO and LO, a total of 12 Raman modes can exist in the tetragonal structure: B_1+E , $A_1(1TO)$, $A_1(1LO)$, $E_1(1TO)$, $E_1(1LO)$ $E_1(3TO)$. Furthermore, due to the complexity of PZT films by the presence of several structures at MPB composition, each Raman peak cannot be easily assigned to each mode frequency, and, in many cases, one peak in the Raman spectra can consist of several mode frequencies as sub-peaks [284, 287, 288].

Raman can provide the information of bond anharmonic with the mode frequency shift as a function of temperature and pressure, which is more useful for investigating polar materials, such as piezoelectric and ferroelectric materials [289]. From the phase diagram, it has been found that the phase transformation can occur with a

change in temperature and composition. However, the phase transition can occur with a change in pressure [290] as well. It has been reported that the ferroelectric tetragonal structure can be transformed into the paraelectric cubic structure above a transition pressure, P_c [291]. Therefore, due to the different first-order Raman modes between the structures, the modes' disappearance can be expected with increasing pressure [292], because the first order modes in a cubic structure are not Raman active [287] and, in an ideal cubic perovskite structure above P_c , the first order Raman modes are forbidden [292, 293]. Moreover mode coalescence can also be anticipated [292], because the mode pairs in the tetragonal structure, such as A_1+E and B_1+E , originate from the first order Raman modes (T_{1u} and T_{2u}) in the cubic structure. P_c has been reported to occur at 11GPa [293] for PZT at the MPB, 2.3GPa and 17.5GPa for nanocrystalline $PbZrO_3$ (PZ) [294], and 12.1 ± 0.2 Gpa [292], 4.3Gpa [291], and 8GPa [295] for pure $PbTiO_3$ (PT). Thus, when pressure is applied to the tetragonal structure, the mode frequency will shift to the mode frequency of the cubic structure until reaching P_c .

The investigation of internal stress is important [117], because it is well-known that the dielectric and piezoelectric properties of PZT films are greatly affected by the stress stimulated by external elastic and/or electric fields due to the stress effect on domain wall motion [82, 83]. The effect of hydrostatic pressure on single crystal PZT can

be simulated as an effect of compressive stress in the film [286] because of the effect similarity between them [296]. The compressive stress can shift the mode to a higher frequency (right in fig. 5.12) and the tensile stress to lower frequency (left in fig. 5.12) [297]. Not all mode frequencies shift under pressure, and the pressure affects the frequency depending on the specific mode. Among the existing modes, B_1+E modes are almost independent of pressure [276], while the other modes can be affected by the application of pressure. The lowest frequency phonon modes, $A_1(1TO)$ and $E_1(1TO)$, known as soft modes, are very sensitive to changes in pressure. However, the lowest modes may be not useful for the pressure evaluation due to high background noise and small changes in frequency under identical pressure [292]. Thus, the frequency shift in the $A_1(3TO)$ mode has been studied in order to evaluate internal pressure [276]. Additionally, because there are the difficulties in the fabrication of single crystal PZT at the MPB composition, the results in this study could be compared with the results from other studies.

The results of Raman spectroscopy are shown in fig. 5.12, organized by the substrate type and the presence of the chelating agent. Contrary with other films, PZT film with heat treatment of 250 °C pyrolysis and 700 °C annealing temperature does not show clear peak intensity, perhaps caused by the high intensity of the background. There

are several factors which affect the peak intensity in the Raman experiment, such as angular dependency of phonon propagation relative to the structure orientation [288, 298-300], the interference among the modes originating from the presence of several structures in PZT films at the MPB composition, and grain size effect [301], and these factors act as background in Raman spectra as well. Furthermore, the compositional fluctuation in the films can be another reason for the line broadening [302]. The presence of the $A_1(2TO)$ mode indicates the presence of a tetragonal structure [275], and the presence of the B_1+E modes indicates the presence of a monoclinic structure [284] in the PZT film. Stress evaluation was performed by the investigation of the $A_1(3TO)$ mode frequency. In both cases, PZT films derived with the precursor with AcAc have higher tensile stress than those derived with the precursor without AcAc. This result may be due to the well crystallized films with AcAc. Comparing the films on the Pt(111) and Pt(200) substrates, much more stress exists in PZT films on Pt(200), probably due to the much higher level of strain originating from the lattice-mismatched substrate. With the various heating temperatures shown in fig. 5.13, the $A_1(3TO)$ peak in the Raman spectra shifts to a lower frequency with increasing pyrolysis temperature. This may be caused by the high degree of the film contraction under high temperature heat treatment during film fabrication.

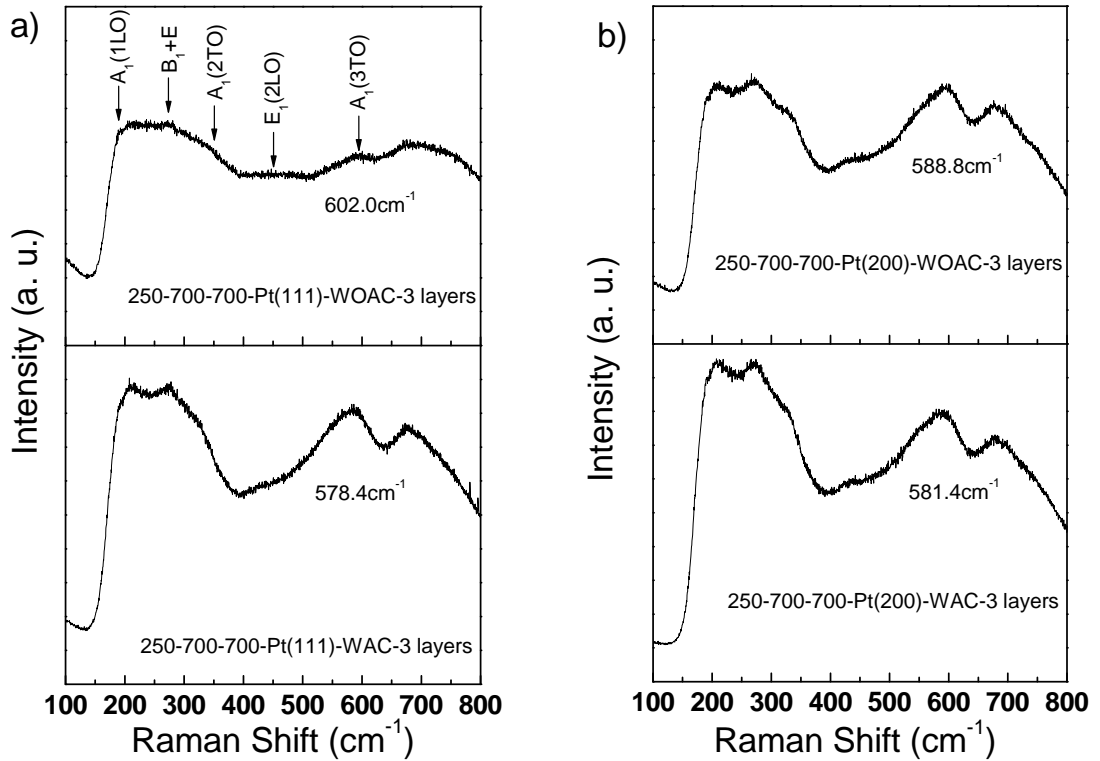


Fig. 5.12 Raman spectroscopy results of PZT films with 3 layers fabricated by a heat treatment of 250 °C pyrolysis and 700°C annealing.

- a) on Pt(111) with and without AcAc
- b) on Pt(200) with and without AcAc

All films shown in fig. 5.12 and 5.13 are under tensile stress. This film stress could be caused by the difference of the thermal expansion coefficient between the film (PZT: $4.03 \times 10^{-6} / ^\circ C$) [303] and the substrate (Si: $2.33 \times 10^{-6} / ^\circ C$) [303] during the cooling in the film fabrication process. Also, the strain originating from the interface between the film and the substrate due to lattice matching can be another possible reason for the tensile stress. Furthermore, it has been reported that the compositional

inhomogeneity and the phase inhomogeneity in the film may also be the reasons for the stress in the film [286].

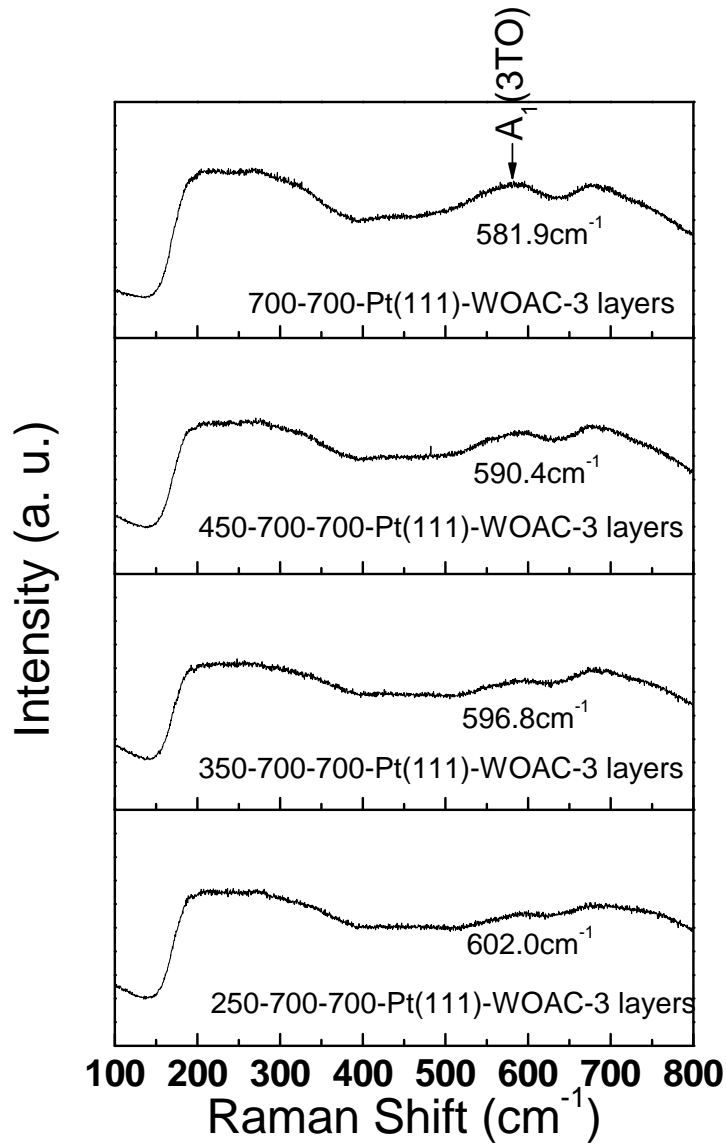


Fig. 5.13 Raman spectroscopy results of PZT films with 3 layers fabricated with various heat treatment conditions on Pt(111) substrate.

5.6 Ferroelectric Property of CSD PZT films by Film Orientation

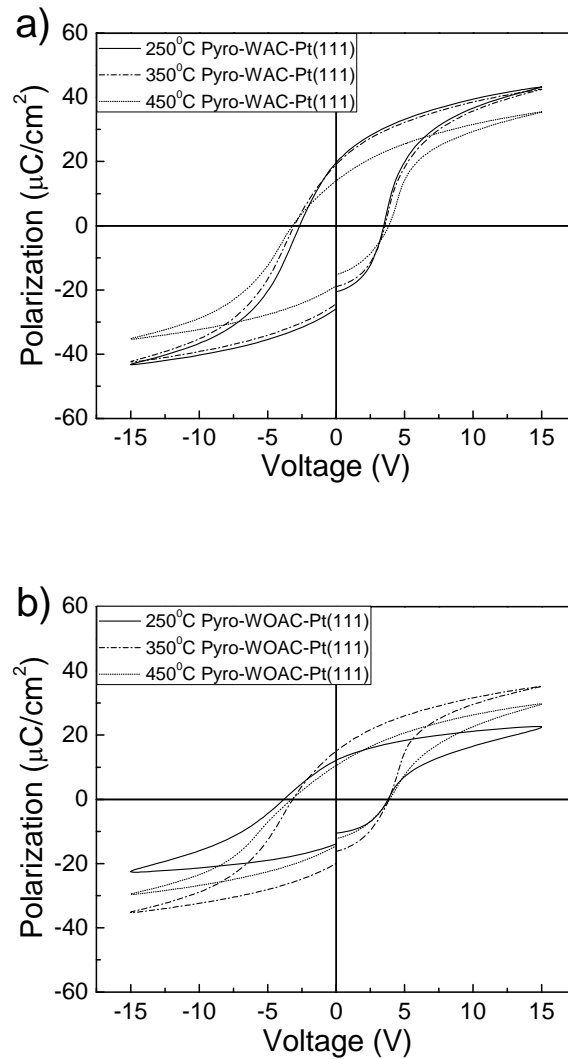


Fig. 5.14 Hysteresis loops of PZT films.

The ferroelectric property of PZT films was investigated by examining the hysteresis loop and the remanent polarization with respect to the sweep voltage, as shown

in fig. 5.14 and 5.15. The maximum polarization value of around $20\mu\text{C}/\text{cm}^2$ can be found in PZT film derived by the solution with AcAc, pyrolyzed at 250°C , and annealed at 700°C . Also, the maximum remanent polarization value is found with this same PZT film.

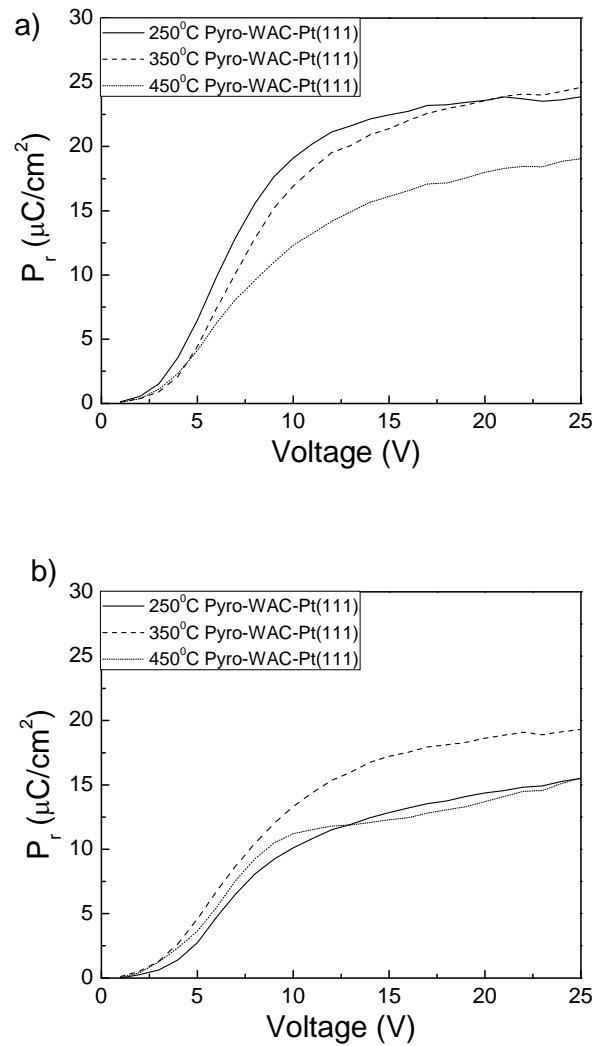


Fig. 5.15 Remanent Polarization of PZT films.

It was found from fig. 5.15 that the PZT film on Pt(111), pyrolyzed at 250°C, and annealed at 700 °C with AcAc shows the highest remanent polarization. The PZT film also has the lowest coercive strength, meaning that the film will have highest polarization at low voltage by the domain switching process. Additionally, the hysteresis loops shows a clockwise rotation with increasing pyrolysis temperature. This is in agreement with the result of S. Trolier-McKinstry et al. [304]. The rotation of the hysteresis loop results from tensile stress due to the difference in the thermal expansion coefficients.

In fig. 5.15, the saturation voltage was evaluated. Most films have a saturation voltage between 10-15V, and the data for the sweep voltage of 15V is shown in Table 5.1. Comparing the films, PZT with the heat treatment of 250°C pyrolysis and 700°C annealing has the highest remanent polarization value. Additionally, from fig. 5.15, it can be found that that at sweep voltages below 5V, which is the operating range of the device, this film has the highest polarization value as well, meaning that this is the optimized condition for the device to reduce voltage consumption during operation.

Table 5.1 Summary of the remanent polarization values of 3-layered PZT films on Pt(111) with different fabrication conditions with film orientation investigation.

Film Condition	Pr ($\mu\text{C}/\text{cm}^2$)	Film Orientation
250°C-WAC-Pt(111)	22.4	(111)
250°C-WOAC-Pt(111)	12.8	(111) (100)
350°C-WAC-Pt(111)	21.4	(111)
350°C-WOAC-Pt(111)	17.2	(100) (111)
450°C-WAC-Pt(111)	16.1	(100) (111)
450°C-WOAC-Pt(111)	12.3	(100)

5.8 Conclusion

PZT films were deposited onto platinized silicon wafers by CSD. Similar to CSD ZnO films, the film properties were greatly influenced by the process parameters, such as the substrate type, the presence of a chelating agent, and heat treatment scheme. Additionally, the chelating agent can provide precursor stability against water molecules and it affects the crystallographic orientation of the film, which is also related to the film properties. The chelating agent, AcAc, increased the crystallization temperature, which may facilitate the formation of the fluorite structure and (111) oriented PZT films. The

chelating agent effect can also be found in PZT films with a one-step heat treatment at 700°C. The surface was affected by the nucleation and growth process, which promoted a dense structure. From the Raman experiment, PZT films on Pt(200) have more stress than those on Pt(111), and this was explained by the strain due to the lattice mismatch. PZT film with low coercive strength and high remanent polarization also has a dense structure and low surface roughness, which are important in terms of real device performance.

CHAPTER 6

DEVICE FABRICATION AND CHARACTERIZATION

6.1 Introduction

FPW devices have been fabricated with various piezoelectric materials, such as AlN [305-307], LiNbO₃ [308], ZnO [70, 309-312], and PZT [313-315]. A wide range of applications for the FPW device as a sensor has been studied, including pressure [316], temperature [305, 317-319], mass density [320-322], viscosity [320], angular rate [315], and vapor [323] and bio- and chemical detection [324-331]. As a chemical sensor, FPW devices (using a Lamb wave) have a higher noise level than SAW devices (using a surface acoustic wave) [332]. However, in vapor sensing, an FPW device will have a phase velocity change higher than that of a SAW device [310], and will also have a higher sensitivity than that of a SAW device [89, 333] and a BAW (Bulk Acoustic Wave) device [308]. Even with a gel-type medium, such as gelatin, agar, and polyvinyl alcohol, wave propagation was not disturbed by the mediums there was no appreciable attenuation

of the signal [334], which indicates that the FPW device is a useful acoustic wave device for chemical and bio sensor applications. The sensitivity for the bio-detection of FPW devices has been reported to be $2.8\mu\text{g}/\text{cm}^2$ for absorbing protein [324], $17200\text{cm}^2/\text{g}$ for detecting IgE immunoglobulins [330], and $16.5\text{m}^2/\text{Kg}$ for IgG immunoglobulins [331]. The first bio-sensor utilizing a FPW device was reported by J.C. Pyun, et al. [335]. They reported a detection range of $3 \times 10^5 - 6.2 \times 10^7$ cells/ml for *E. coli*. In the case of the application of a Lamb wave in a thin membrane to measure temperature, the thin membrane can have a rapid thermal response due to the low heat capacity of the thin plate [336]. However, in other applications, this frequency temperature sensitivity is undesirable and can be a source of instability for FPW devices [317, 319, 337]. The frequency change of the device by temperature variation is due to the variation of the elastic constant and the mechanical deformation by thermal expansion within the membrane materials [318]. For example, the temperature sensitivity of a device with $2.5\mu\text{m}$ and $12\mu\text{m}$ thicknesses of AlN piezoelectric film and the total membrane, respectively, had a frequency change of $-70\text{ppm}/^\circ\text{C}$ in a temperature range of $20 \sim 38^\circ\text{C}$ [319]. This means that undesirable temperature sensitivity cannot be avoided in practical applications, even at a range near room temperature, and so it requires correction. This

compensation for the temperature sensitivity of FPW devices has been reported [318, 319].

6.2 Device Fabrication Process and Issues

In this trial, FPW devices were fabricated with sputtered ZnO films. The device fabrication started with silicon wafers layered with 1.2 μm of stoichiometric silicon nitride. The silicon nitride layer is used for the mechanical support of the FPW membrane and a KOH etching stop (the etching rate of stoichiometric silicon nitride in KOH is almost zero) [338]. Two kinds of adhesion layers, Pt and Ta, were used for the device fabrication. Because Pt, used for the bottom electrode, has poor adhesion strength as deposited onto silicon nitride, using an intermediate Ta layer can provide good adhesion of Pt layer. The Ta layer was deposited by sputtering to a thickness of 40nm. Next, the Pt layer was deposited onto the Ta adhesion layer. Pt is an often-used material for electrodes, due to its chemical and thermal stability under heat treatment [339]. Then, the piezoelectric films were deposited onto the bottom electrode for generating and detecting acoustic waves for the sensor application. Sputtered ZnO film of 1.5 μm in thickness was fabricated with 200W RF power, and a sputtering pressure of approximately 16mTorr,

which was achieved by flowing 48sccm each of Ar and O₂ gases. The desired thickness was reached after about 4 hours of sputtering. RT deposition was used because of the avoidance of heat treatment during and after film deposition, which reduces a step in the device fabrication process, and, hence, reduces the cost for mass production of the device. Then, the Pt layer for the top electrode was deposited onto the piezoelectric film. The top electrode was completed by a lift-off process. Positive photoresist (PR) AZ5214 was used for patterning of the top electrode. The wafer with piezoelectric film was put onto a spin coater, and the photoresist was dropped onto the surface. The spin condition was 300rpm for 30sec, which provided around 1.4 μ m of PR thickness. Photolithography was performed using a double-sided mask aligner. The patterned wafer was exposed to 345nm UV light for 8 seconds and developed for 40 seconds to form the pattern. The Pt layer for the top electrode was deposited by sputtering to a thickness of 100nm, and then the wafer was immersed into acetone to dissolve the PR for lift-off. To etch out the silicon wafer from the back side by KOH etching, an opening in the silicon nitride layer was made by the reactive ion etching (RIE) process. The power settings were RF 300W for the coil and 50W for the plate, and the process gases were CH₃ (30sccm) and oxygen (10sccm). The etching was performed 3 cycles of 3 minutes each. Then, around 1.2 μ m of silicon nitride layer was etched out. After the RIE process, the wafer was immersed into

the etchant, consisting of KOH (45%), water, and isopropanol, to etch out the silicon wafer through the whole thickness. KOH etching was performed at 80°C, and about 10 hours etching time was required for the etching of the whole silicon wafer. The entire process of FPW device fabrication and the roles and issues of each step are summarized in table 6.1 and fig. 6.1.

Table 6.1 FPW device fabrication issues.

Layer type	Composition (Thickness)	Purpose of the layer	Fabrication issue	Remarks
Membrane	Si ₃ N ₄ (800nm, 1200nm)	Mechanical support KOH etch stop	Stress Control	
Adhesion layer	Ta (40nm)	Prevention of delamination of the electrode		
Bottom electrode	Pt (200nm)	Electrical contact	Orientation	Orientation of ZnO films is affected by the orientation of the bottom electrode
Piezoelectric layer	ZnO (1500nm)	Transducing of the acoustic wave generating through the membrane	Orientation, Stress Resistivity	
Top electrode	Pt (100nm)	Electrical contact		

A potential source of difficulty in the photolithography process is that sputtered ZnO film is transparent and sensitive to UV light. However, reducing the thickness of the PR and the duration time in developer can help alleviate this issue. The most difficulty with the fabrication process was with the KOH etching step. Due to the very thin membrane, care had to be taken during the handling of the wafer. Also, stirring was needed for during etching in order to maintain compositional and thermal uniformity of the KOH solution. However, stirring can break the membrane due to the high strength of etchant flow; thus, a low stirring rate is recommended for KOH etching for this device.

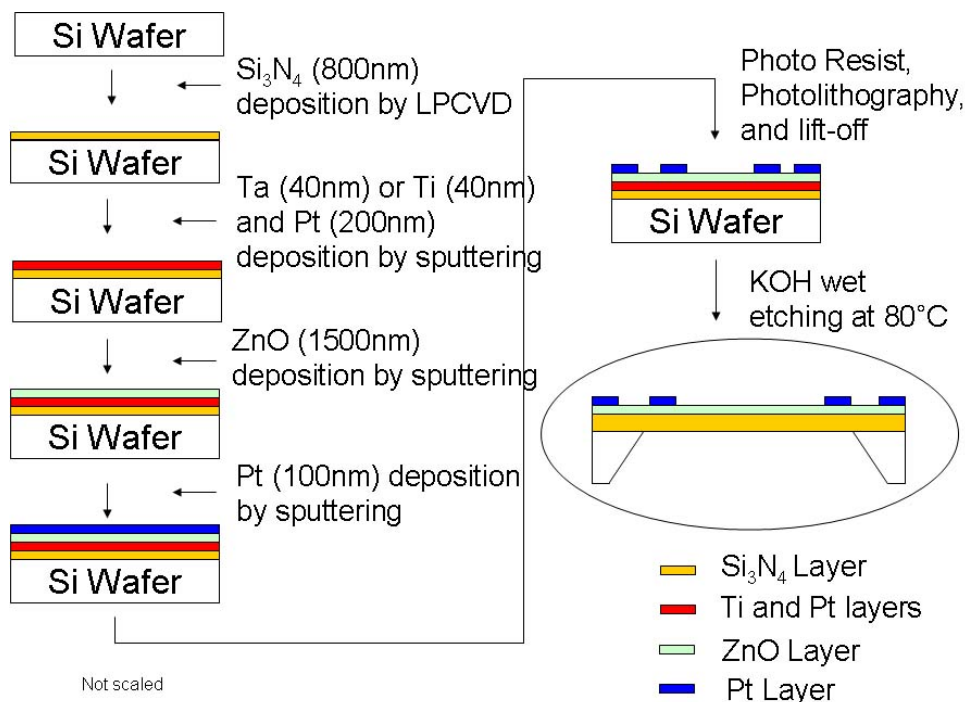


Fig. 6.1 FPW device fabrication procedure.

6.3 Device Design and Characterization

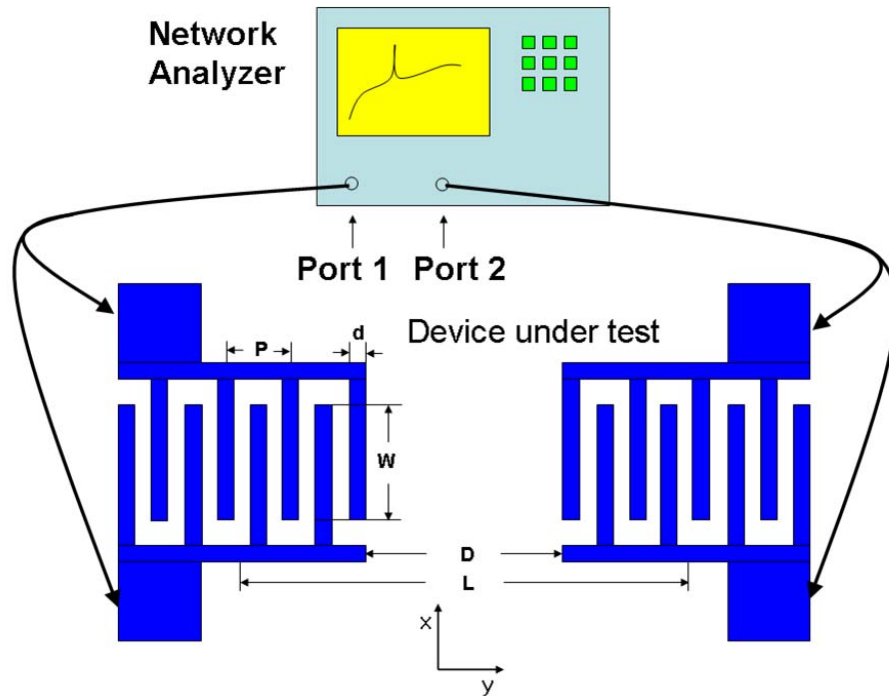


Fig. 6.2 Schematic diagram of Network analyzer set-up for device characterization.

A network analyzer is commonly used for device characterization, and the typical set-up of this system is shown in fig. 6.2. Through port 1, the electric signal is provided to the input IDT for generating the acoustic wave through the piezoelectric material. The generated wave propagates through the membrane and reaches the output IDT. At the output IDT, the acoustic wave, with a specific frequency determined by the device design, is transformed into electrical signal at port 2. The device was characterized by identifying

the operating frequency and the frequency change (in dB) as measured by the network analyzer.

Fig. 6.3 shows the dispersion characteristic of Lamb waves in a curve of v_M/v_t vs. $k_t d$. v_M is the phase velocity of the FPW membrane, and v_t is the phase velocity of the transverse acoustic wave. d is the thickness of the membrane and k_t is the wave number of the transverse wave, which is related to the wavelength of the transverse wave by $k_t = 2\pi/\lambda$, where λ is the wavelength of the transverse wave. These parameters are the measurable quantities in the experiment and are related to each other. Thus, they can be used to make a comparison between theoretical and experimental results, such that the mode may be identified [340].

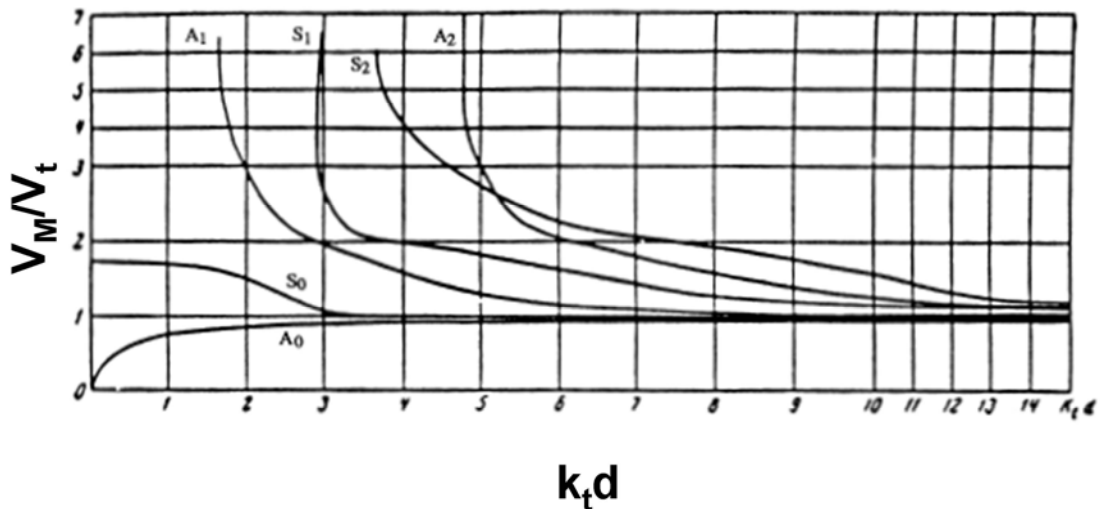


Fig. 6.3 Calculated antisymmetric and symmetric modes of Lamb waves [341].

Additionally, the phase velocity is related to the material density and the elastic stiffness coefficient by $v = \left(\frac{c}{\rho} \right)^{\frac{1}{2}}$. Therefore, if the measurands are the factors which affect the stiffness and density, such as lattice strain, temperature, and pressure, then they can be considered to be the sensing parameters by means of their perturbation. However, the relationship can also be applied to homogeneous, non-piezoelectric materials. In the case of piezoelectric materials, the wave velocity is also a function of the electrical conductivity of the materials, because of the piezoelectric characteristic. Thus, in piezoelectric materials, the factors that affect elastic stiffness, density, and electrical conductivity can be considered the sensing parameters [333]. As shown in fig. 6.3, all non-zero modes have a region where the modes cannot exist, and this can provide a cut-off frequency where the modes may be used for the sensing application. The A_0 mode's wave velocity approaches zero as the plate becomes thinner, and the S_0 mode is shown to be dispersionless in the thin region of the plate. So, the dispersion character of A_0 indicates that, in a FPW device with a thin plate (usually equal to or less than the wavelength), the A_0 mode can be used for the sensor application. Furthermore, the thin plate can provide lower phase velocity of the A_0 mode, typically in the range of 200-300m/s [342], depending on the materials and sensor configuration. This is less than the

velocity in water, which is typically in the range of 1481 – 1555m/s for temperatures of 20–75 °C [343]. This low phase velocity can provide operation at low frequencies by the relation $f = v_M/\lambda$, and can provide a simple electrical circuit. Additionally, the acoustic wave propagation velocity is the factor that is related to piezoelectric materials. For SAW devices, the acoustic wave velocity has been reported to be 6,340m/s for ZnO film, and 4,500m/s for PZT film, which are higher than the velocity in water because SAW devices have a bulk silicon wafer below the electrodes, while FPW devices have a membrane.

For the group and phase velocity of the A_0 and S_0 modes propagating in an homogeneous and isotropic membrane with thickness increasing from zero, the expression is given by [341]:

$$v_{pA0} = \sqrt{\omega d} \left(\frac{E}{3\rho(1-\nu^2)} \right)^{\frac{1}{4}}, \text{ and } v_{pS0} = \left(\frac{E}{\rho(1-\nu^2)} \right)^{\frac{1}{2}} \dots\dots\dots(6.1)$$

and

$$v_{gA0} = 2\sqrt{\omega d} \left(\frac{E}{3\rho(1-\nu^2)} \right)^{\frac{1}{4}}, \text{ and } v_{gS0} = \left(\frac{E}{\rho(1-\nu^2)} \right)^{\frac{1}{2}} \dots\dots\dots(6.2)$$

where E is Young's modulus, ρ is the plate density, ν is Poisson ratio, ω is a circular frequency, and d is the plate thickness. From equations (6.1) and (6.2), it can be found that

$$v_{gA_0} = 2v_{pA_0} \text{ and } v_{gS_0} = v_{pS_0} \dots\dots\dots(6.3)$$

Thus, A_0 has a group velocity of twice the phase velocity, and S_0 has a group velocity that is equal to the phase velocity. Note that these equations do not include tension or any perturbation effect. During film and device fabrication, tension will be introduced into the film and device, which will affect the device operation. When the membrane is under tension and the wave is propagating in the x-direction, the phase velocity of the A_0 mode with the tension effect is [336]:

$$v_{pA_0} = \frac{2\pi}{\lambda} \left(\frac{T_x + B}{M} \right)^{\frac{1}{2}} \dots\dots\dots(6.4)$$

and the group velocity is expressed by:

$$v_{gA0} = v_{pA0} \left(1 + \frac{v_{pA0}[T_x=0]^2}{v_{pA0}^2} \right) \dots\dots\dots(6.5)$$

where, $B = \left(\frac{\lambda}{2\pi} \right)^2 T_x + \frac{Ed^3}{12(1-\nu^2)}$ for an homogeneous and isotropic membrane, and represents the plate material stiffness. T_x is the in-plane tension component in the x-propagation direction, and M is the mass per unit area of the membrane.

$$v_{pA0}[T_x=0] = \frac{2\pi}{\lambda} \sqrt{\frac{Ed^3}{12M(1-\nu^2)}} \text{ indicates the phase velocity without tension in the}$$

membrane. From equations (6.4) and (6.5), it is found that the phase velocity of the acoustic wave can be increased by adding tension to the membrane, while the group velocity will decrease [336]. The difficulty of calculating the operating frequency originates from the difficulties of calculating the bending stiffness and elastic modulus of the membrane, because the membrane is composed of four layers [336].

For chemical and biological applications, most sensors are of the mass-sensing type. Thus, the mass adding effect is the main concept for the sensor application. By including the mass adding effect in equation (2.4), the phase velocity change of the A_0 mode with a mass change without the tension effect can be expressed by [89]:

$$v_{pA0} = \frac{2\pi}{\lambda} \left(\frac{B}{M + \Delta m} \right)^{\frac{1}{2}} \dots\dots\dots (6.6)$$

With the tension effect, the equation becomes:

$$v_{pA0} = \frac{2\pi}{\lambda} \left(\frac{T_x + B}{M + \Delta m} \right)^{\frac{1}{2}} \dots\dots\dots (6.7)$$

where Δm is the mass change of the sensor. This equation can be widely used for chemical, physical, and biological sensing perturbed by a mass change. When the added mass is quite smaller than M ($M \gg \Delta m$), the square root expression in the Taylor series can be utilized, and the phase velocity change by adding a small mass can be approximated by [88]:

$$\frac{\Delta v_{pA0}}{v_{pA0}} \cong -\frac{\Delta m}{2M} \dots\dots\dots (6.8)$$

where v_{pA0} is the A_0 phase velocity of the acoustic wave unperturbed by the mass change, and Δv_{pA0} is the amount of the velocity change after perturbation by adding the mass. The mass sensitivity of the FPW device can be defined by:

$$S_m = \frac{1}{\Delta m} \frac{\Delta v_{pA0}}{v_{pA0}} \cong -\frac{1}{2M} \dots\dots\dots (6.9)$$

The unit of the mass sensitivity is area/mass, and so a thinner membrane will reduce the phase velocity and increase the mass sensitivity.

For chemical gas sensing, a selective layer is usually used for detecting and absorbing the gas particles. For example, polydimethylsiloxane is used for carbon tetrachloride and toluene due to its high diffusion coefficient and ability to absorb non-polar organic vapors [327], and photoresist is used for acetone and methanol [309]. The layer attached to the sensor surface can be considered as a part of the sensor, and the phase velocity of the total sensor becomes [89, 329, 344]:

$$v_{pA0} = \frac{2\pi}{\lambda} \left(\frac{B}{M + \rho_L d_L} \right)^{\frac{1}{2}} \dots\dots\dots (6.10)$$

where ρ_L and d_L are the density and the thickness of the selective layer, respectively.

The product of ρ_L and d_L is the mass of the layer, and this can be considered to be a mass change by the addition of the layer (Δm) as per equation (6.7). The sensitivity of the FPW device with the selective layer can be expressed by:

$$S_m = -\frac{1}{2(M + \rho_L d_L)} \dots\dots\dots (6.11)$$

When the mass loading effect is on both sides of the FPW device, the mass term is corrected to $2\rho_L d_L$ [89].

There is little to no attenuation when an FPW device is immersed in water, but this is not true with the case of immersion in a viscous liquid or gel. The viscous liquid can be considered to act as a mass load, but the difference with the case of water comes from the liquid characteristic, which can cause an evanescent decay during operation. The phase velocity of a FPW device in such a medium with the tension effect is [88]:

$$v_{pA0} = \frac{2\pi}{\lambda} \left(\frac{T_x + B}{M + \rho_L d_E} \right)^{\frac{1}{2}} \dots\dots\dots (6.12)$$

where ρ_L and d_E are the density of the viscous liquid and the evanescent decay length, respectively. The decay length is given by:

$$d_L = \left(\frac{\lambda}{2\pi} \right) \left[1 - \left(\frac{v_{pA0}}{v_L} \right)^2 \right]^{-\frac{1}{2}} \dots\dots\dots (6.13)$$

where v_L is the phase velocity of the viscous liquid. The sensitivity of the FPW device in a viscous liquid becomes:

$$S_m = -\frac{d_E}{2(M + \rho_L d_E)} \dots\dots\dots (6.14)$$

Equations (6.10-12) can be utilized for the characterization of the properties of the viscous liquid, such as a viscosity. Additionally, the typical decay length of a typical FPW device has been reported to be 16 μ m [329]. Compared with this value, APM has a typical decay length of 50nm [345], which is much less than that of FPW device.

In the FPW device, transduction is carried out by an interdigital transducer (IDT). Therefore, the design of the IDT is the key issue for generating and detecting the electrical and mechanical signals. The IDT was created by White [346], and with an IDT,

an electric field can be produced at the surface of a piezoelectric material. The electric field can generate an acoustic wave, which propagates through the membrane, and is reconverted to an electric field at the second pair of the electrodes. Commonly, only one pair of IDT is insufficient to generate the acoustic wave at the surface, and at least five pairs of IDTs are usually required [347]. The longer the length of the IDT (L_1), especially the length of the aperture (L), and the more the number of IDTs (N), the more enhancement there will be to the electrical and mechanical signals. In other words, by using the many long IDTs, the device will be more capable to produce and receive the signals. According to T. Laurent [348], the generated modes of the Lamb wave depend on the IDT design. The IDT configuration in this study can have three modes in the membrane of the FPW device: A_0 , S_0 , and SH modes. Among those modes, the oscillation frequency can be determined by the mode which has lowest delay line loss [324].

There have been some methods used to analyze the excitation by IDT, including the equivalent circuit model [349] and Green's function method [350], and the delta-function model [351]. In Green's function model, the amplitudes of the generated Lamb wave are calculated in terms of surface energy charge density on the transducer electrodes. However, the various parameters in the equivalent circuit cannot be calculated,

and so the best fit to the experimental data must be obtained. The delta-function model has been widely employed for the mathematical analysis for the IDT design [351]. This model assumes that the system is linear and the charge distribution at the electrode surface is uniform, even though the distribution has a peak at the edge of the electrode in reality. Assume that the IDTs have equal dimensions in length (L) and width (d_1) and that $\phi(x')$ is the charge density per unit length in the $+x$ direction, which is the acoustic wave propagation at the surface of the piezoelectric material. Due to the linear system, the charge in a small length dx' can be expressed by $\phi(x')dx'$, and the amplitude $A(x, \omega)$ is linearly proportional to the amplitude of stress, strain, and particle velocity.

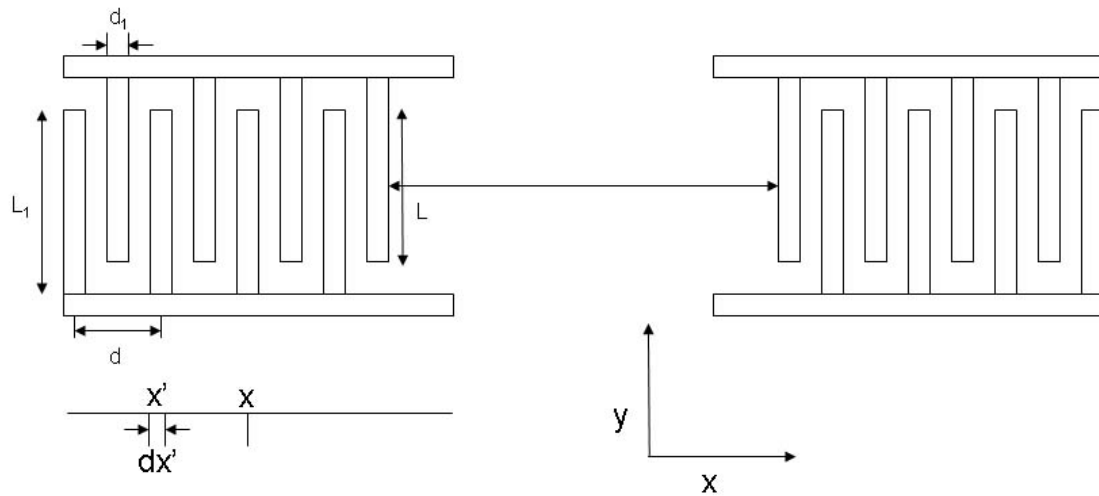


Fig. 6.4 Schematic diagram of IDT design.

When the wave with radian frequency ω arrives at x from the element between x' and $x'+dx'$, the amplitude $dA(x, x', \omega)$ can be expressed as:

$$dA(x, x', \omega) = \sigma \phi(\omega, x') e^{-jk(x-x')} dx' \dots\dots\dots(6.15)$$

where σ is a coupling constant between the amplitude of the acoustic excitation and the charge, and $k(x-x')$ is the phase shift between the acoustic excitation position x' and the detection position x . The amplitude observed at x should be the sum of the contributions from all elements of length dx' between x' and x , when the acoustic excitation is propagating in x -direction. The total signal at x is:

$$A(x, \omega) = \sigma \int_{-\infty}^x \phi(\omega, x') e^{-jk(x-x')} dx' \dots\dots\dots(6.16)$$

When the position x is outside of the exciting IDT, $\phi(x) = 0$. Thus,

$$A(x, \omega) = \sigma \int_{-\infty}^{\infty} \phi(\omega, x') e^{-jk(x-x')} dx' \dots\dots\dots(6.17)$$

The amplitude at the output is a Fourier transform of the charge on the IDTs, and due to the Fourier transform for the output signal, the impulse response of the IDTs is equal to the spatial charge distribution along with the length of the IDTs. Furthermore, in a FPW device, which has a large IDT width compared with the membrane thickness, the electric field applied to the IDTs will be uniform and vertical through the whole thickness. Thus, the applied electric field is uniformly distributed across the width and through the thickness, which gives:

$$A(x) = j\sigma C e^{-jkx} \frac{\sin(kNd/2)}{\cos(kd/4)} \operatorname{sinc}\left(\frac{d_1}{\lambda}\right) e^{jk(N-1)d/2} \dots\dots\dots (6.18)$$

where N is the number of finger pairs, and d is the distance of one period of the IDT finger pairs. In the expression $\operatorname{sinc} cx = \frac{\sin \pi cx}{\pi cx}$, C is the total charge for a single finger and can be expressed as $C = \phi d_1$. The amplitude $A(x)$ is periodic, according to the term $\frac{\sin(kNd/2)}{\cos(kd/4)}$. The amplitude $A(x)$ is at a maximum, when $kd = 2\pi n$ ($n = \text{integer}$) and n is an odd integer, which makes the term $\frac{\sin(kNd/2)}{\cos(kd/4)} = \pm 2N$, and the amplitude $|A(x)| = 2\sigma CN \operatorname{sinc}\left(\frac{d_1}{d}\right)$. This condition of k value happens at the center frequency (or synchronous frequency), $\omega = \omega_n$, where $\lambda = \frac{d}{n}$. If n is even integer, the operating frequency $\lambda = \frac{d}{n}$ is 180° out

of the phase between the neighboring fingers, and they will cancel out each other, resulting in no amplitude. Additionally, because of the dispersive characteristic of the A_0 Lamb wave, the operating frequency with wavelength $\lambda = d/n$ in a higher mode will not exactly be the multiple of the lowest operating frequency. Thus, from equation (6.18) it can be concluded that a larger number of fingers can increase the output signal.

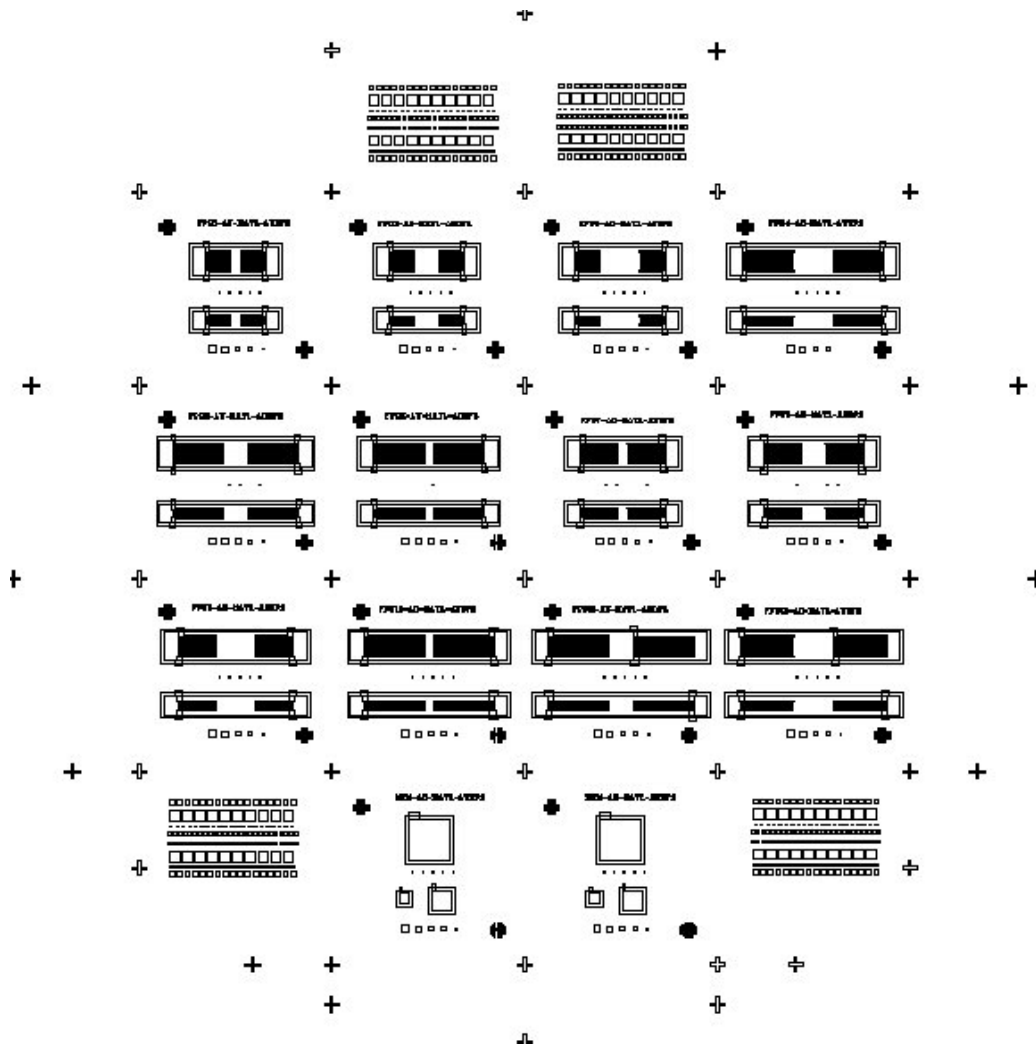


Fig. 6.5 Mask design of FPW device array in this study.

The IDT design in this study consisted of 22 different types, which had different sizes of IDT pairs (25, 35, 40, and 50 μm), different distances between both IDTs (1000, 2500, and 4000 μm), different electrode widths (100 μm and 150 μm) and different sizes of aperture (650, 750, and 1550 μm). The mask, shown in fig. 6.5, was designed to ascertain the variation of output signal according to the IDT design. The frequency of the acoustic wave depends on the periodicity (P) of the IDT, which vary with the IDT width (d). This is because the periodicity (P) is typically four times the IDT width (d) due to the equal length of IDT width and the distance between the IDT fingers. The frequency is expressed by $f = \nu/d$, where f , ν , and d are the operating frequency, the acoustic wave propagation velocity, and the periodicity of IDT, respectively. Thus, the periodicity is the main factor to determine the operating frequency of the device.

The distance between both IDTs (D) can be used for the delay time, because there will be some amount of time for the acoustic wave to propagate through the area which does not have any electrodes. The number of IDT pairs and the aperture (w) are the main factors which govern the strength of output signal.

The fabricated FPW device array on the silicon wafer is shown in fig. 6.6, fabricated by microelectronic fabrication techniques as detailed earlier. In fig. 6.6 (a), the

front side (electrode side) is shown, and the etched appearance of the backside of the wafer due to the KOH solution can be seen in fig. 6.6 (b).

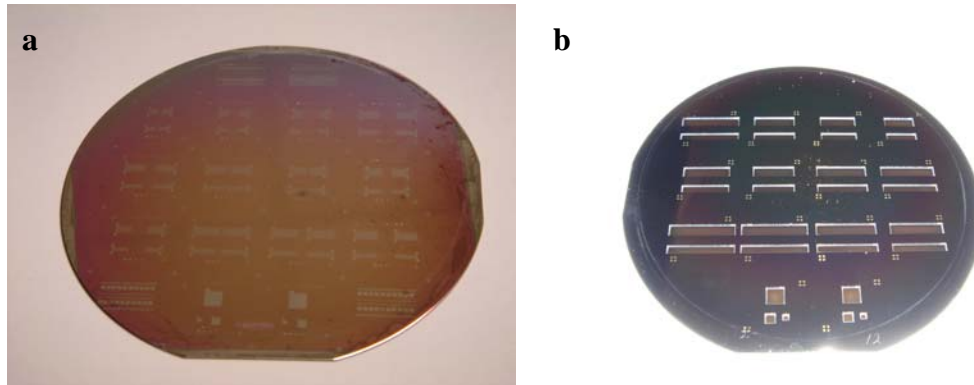


Fig. 6.6 The array of FPW device; a) front side view, and b) backside view (KOH etched side).

Fig. 6.7 represents the typical response of the FPW device, which is the gradual increase of the dB value in the low frequency range. In fig. 6.7 (a), the first peak around 1.65MHz has been assigned as the first operating frequency (A_0 mode, $n=1$), and the second peak around 6.18MHz as the second operating frequency (A_0 mode, $n=3$). They correspond to the first antisymmetry mode. Compared with this response, only one mode at 3.33MHz has been found in fig. (c), and the peak has been assigned as the first operating frequency in the measured frequency range. This difference originates from the device design. The device shown in fig. (a) has a 150 μm IDT period, while the device in

fig. (b) has a 100 μm IDT period. The larger IDT period gives a lower operating frequency according to the equations, $f = \frac{v_p}{\lambda}$ and $\lambda = 4p$ [344] for the case where the IDT width has same dimension as the distance between IDTs. The insertion loss at the first peaks was found to be -23.18dB for the device in fig. (a), and -28.67dB for the device in fig. (c), respectively. Theoretically, the device has a minimum insertion loss of -6dB in a two port device, which originates from the loss in both IDTs. Thus, the rest of the insertion loss is coming from the poor material quality [352]. From fig. 6.7, the peaks can be found between 1.6MHz and 1.7MHz for the device in fig. (b) and between 3.35MHz and 3.45MHz for the device in fig. (d). In those ranges, multiple peaks were found, and those peaks may be due to the multiple wave reflections from both ends of the membrane [101]. The FPW device can operate when differentially driven by the voltage and the displacement of adjacent fingers that are 180° out of phase with the ground plane [344]. And, the operating frequency of the FPW device can be found by investigating the change in the phase angle, where there is a 180° phase angle change at the frequency, as can be seen in fig. 6.7 (b) and (d). By the equation $f = \frac{v_p}{\lambda}$, the phase velocity of the acoustic wave device can be derived. For the device in fig. (a), the phase velocity was found to be 247m/s, and 333m/s for the device in fig. (c). These velocities are much lower than the velocity in water. For the estimation of the sensitivity, equation (6.9) may

be useful. The membrane is composed of 4 layers and the value of M is 0.0172Kg/m^2 , which gives a sensitivity of -290.7cm/g . Moreover, in the case of the device with a 1.65MHz operating frequency, if a 10Hz change with short term instability can be detected, then the minimum detectable mass density (MDMD), $\Delta m_{\min} = \frac{1}{S_m} \frac{\Delta f_{\min}}{f_o}$, is 208.5ng/cm^2 . If 1Hz in change can be detected, then the MDMD is 20.85ng/cm^2 .

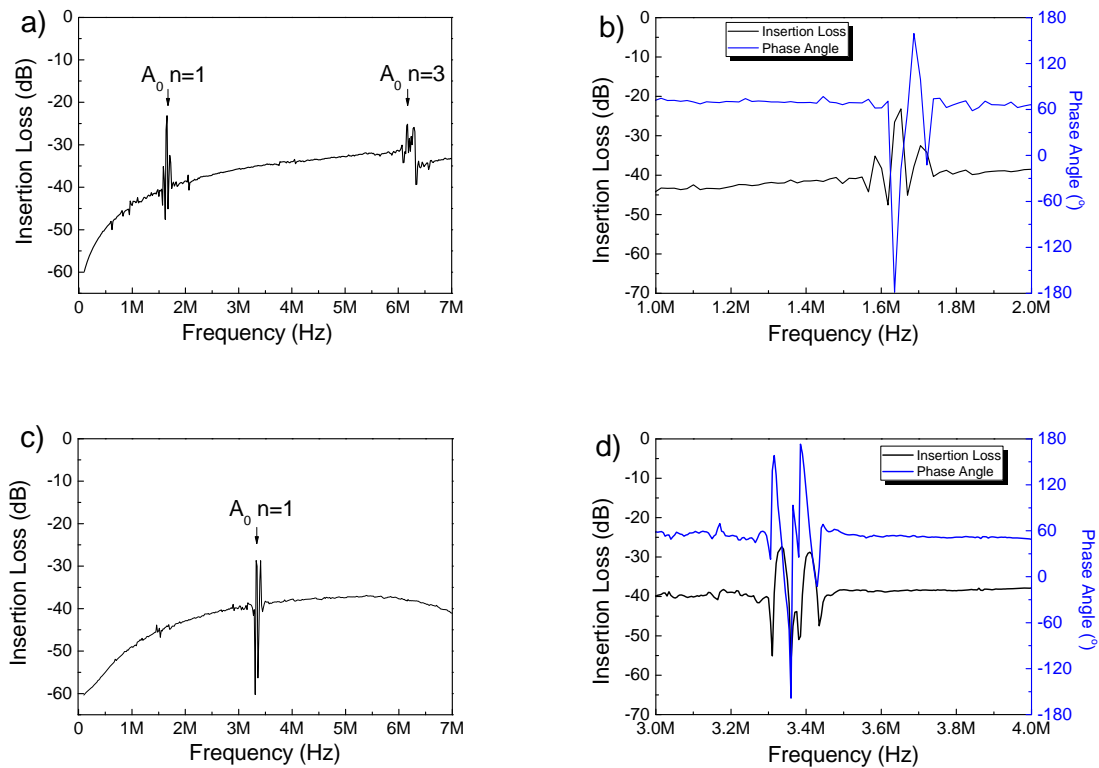


Fig. 6.7 FPW device response with sputtered ZnO film.

- e) FPW device with $150\mu\text{m}$ of IDT period, 25 pairs of IDT, $1550\mu\text{m}$ of aperture
- f) Frequency range of 1MHz to 2MHz according to (a)
- g) FPW device with $100\mu\text{m}$ of IDT period, 25 pairs of IDT, $750\mu\text{m}$ of aperture
- h) Frequency range of 3MHz to 4MHz according to (c)

In fig. 6.8, the (a) device has 25 pairs of IDT on both sides, and a 750 μm aperture size. Comparing with this, the (b) device has a 1550 μm aperture size with the same number of IDT pairs, and the (c) device has 50 pairs of IDTs with the same aperture size. As seen from the figure, both of these devices have a lower insertion loss than the (a) device, as might be expected from equation (6.18), which shows that a strong amplitude of the acoustic signal at the output port can be achieved by increasing the aperture size and the number of IDT pairs.

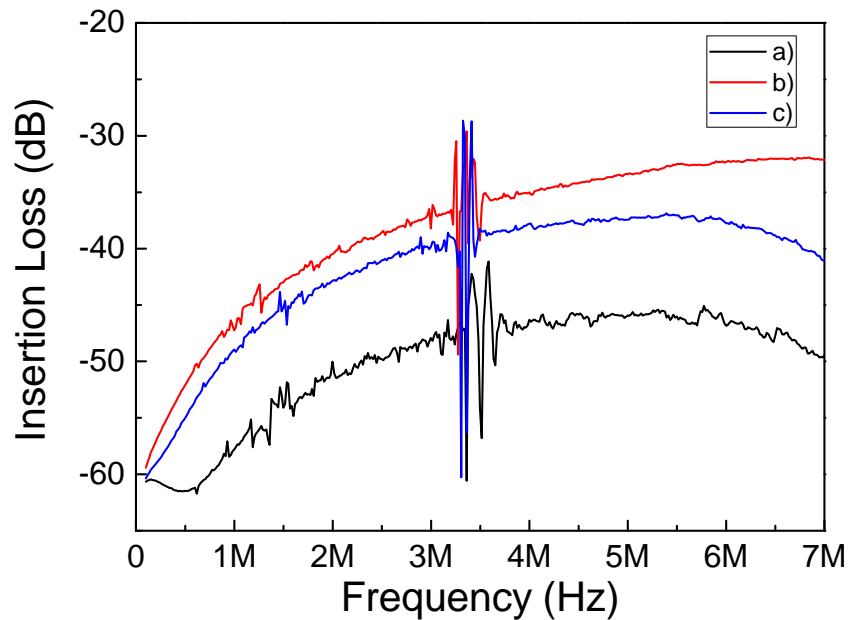


Fig. 6.8 FPW device response of three different device designs.

6.4 Conclusion

An FPW device has been successfully fabricated onto a 4 inch silicon wafer by microelectronic fabrication. The issues in fabrication of the FPW device were addressed in this chapter. Ta was used for the adhesion layer, and sputtered ZnO films were used for the piezoelectric film. The device response was obtained, and the A_0 mode occurred at 1.65MHz and 3.33MHz, depending on the device design. The phase velocities of the device were found to be 247m/s for the device with a 1.65MHz operating frequency, and 333m/s for the device with a 3.33MHz operating frequency. The calculated sensitivity is -290.7cm/g, and MDMD was calculated to be 208.5ng/cm² if 10Hz in the frequency change by the perturbation of the acoustic wave can be detected. For the device design, the aperture size and the number of IDT pairs were investigated, and it was found that the output signal can be enhanced by increasing the number of IDT pairs and the aperture size.

CHAPTER 7

CONCLUSION OF DISSERTATION AND FUTURE WORK

7.1 Conclusion of Dissertation

ZnO and PZT films have been fabricated by the sputtering deposition and chemical solution deposition methods for use in the sensor application. The material properties of the films were a key focus in this work since they are closely related to the final device performance. In this study, the main focus was on the microstructural properties of the materials, because the textured microstructure is the main factor for the piezoelectric property.

Two methods were used to fabricate the ZnO films: sputtering and CSD. In CSD ZnO, the chelating agent effect on the microstructure of ZnO films was assessed. Two kinds of chelating agents, DEA and MEA, were employed to stabilize the precursor and increase the solubility of zinc acetate in 2-MOE. The difference between them comes from the bonding of the metal ion, which causes polymerization in the precursors to a different degree. Because the degree of polymerization affects the energy barrier of nucleation, it also greatly influences the film texture. When DEA was used as a chelating agent, the solution stability was confirmed. However, because it increases the nucleation barrier, a substrate is required that closely matches the crystallographic configuration of

the desired film in order to reduce the energy barrier. In the case of the ZnO films derived with MEA-chelated solution, the c-oriented microstructure can be found even on an amorphous substrate, due to the low energy barrier for nucleation. Another difference is in the degree of film contraction during crystallization. Due to the weaker bonding with the MEA chelated precursor as compared to the DEA chelated precursor, the film derived with MEA has more tensile stress in the film due to the larger degree of contraction. All ZnO films derived by CSD were under a tensile stress, which may have been caused by different thermal expansion coefficients between the films and the substrates and the lattice mismatch at the interface between the films and the substrates.

Sputtered ZnO films were fabricated and their properties investigated because CSD is generally not suitable for mass production. The substrate effect, heat treatment, and the process gases and their ratio were investigated. It was found that the substrate effect in the sputtered ZnO films is less sensitive than in CSD ZnO films, which may be due to the highly energetic particles from the plasma. However, the existence of strain due to lattice mismatch hinders oriented nucleation on the substrate surface. Two process gases, Ar and oxygen, were used for the fabrication of sputtered ZnO films. The film properties, such as film crystallinity and stress, were found to vary depending on the gas ratio. There was a transition in stress depending on the gas ratio, and the stress was also related to the defect state in the films. Heat treatment during deposition and post deposition was found to enhance certain film properties, such as a more c-oriented structure, lower defect concentration, and less internal stress due to the high mobility of the adatoms and the incorporation of oxygen from the environment. Film morphology

and microstructure were investigated according to the gas type and ratio. It was found that the process parameters are co-related to each other and to the film properties.

The properties of ferroelectric PZT films were also evaluated. CSD was the fabrication method for PZT films. For PZT films, the structure of the film was the main property to be investigated in this study. The texture of PZT films was influenced by the process parameters, such as the presence of a chelating agent, heat treatment, and substrate type. Due to the presence of a chelating agent, the crystallization temperature increased, thereby enhancing the generation of the fluorite phase, which can easily be transformed into the perovskite structure. The configuration of the substrate also plays a role in film orientation, but the orientation can be modified by varying the heat treatment temperature. The films were found to be in a tensile internal stress state, which was determined to be due to the degree of lattice mismatch and the difference in the thermal expansion coefficients between the film and the substrate.

From the characterization of the films, it was found that the process parameters can manipulate the film properties and are also co-related to each other. Thus, to achieve the desired film properties, each parameter should be evaluated in terms of its relationship to all of the other parameters.

FPW device arrays on a 4 inch silicon wafer were successfully fabricated by microelectronic fabrication methods. Sputtered ZnO films were utilized for the piezoelectric film, and Ta was employed as an adhesion layer. The device response was evaluated using a network analyzer, and A_0 modes were obtained at 1.65MHz and 3.33MHz, depending on the device design. Phase velocities of 247m/s and 333m/s were

found in the devices with A_0 modes of 1.65MHz and 3.33MHz, respectively. The calculated sensitivity was -290.7cm/g , and the minimum detectable mass density was 208.5ng/cm^2 . The operating frequency varied with the device design, depending especially on the IDT period. The aperture size and the number of IDT pairs were found to affect the amplitude of the output signal.

7.2 Future Work

In the future, this research should be extended to real-world applications in the areas of biosensors and actuators. FPW devices show promise for these applications because of several advantages, including high sensitivity, simple electric set-up, and the ability of the electric set-up to be isolated from the measurands. Furthermore, the FPW device with PZT film has very high dielectric and piezoelectric constants, and so should be an excellent choice for use as an actuator due to the high displacement of this film. Also, for use as a microfilter or micropump, the PZT FPW device has the advantages the no-clogging effect by the material to be filtered and the self-cleaning effect. Furthermore, it would be of interest to further define the relationship between the acoustic properties and the material properties of the thin membrane.

BIBLIOGRAPHY

- [1] C. T. Lin, S. M. Wang, *Frontiers in Bioscience* 10 (2005) 99.
- [2] A. K. Deisingh, M. Thompson, *Canadian Journal of Microbiology* 50 (2004) 69.
- [3] R. Raiteri, M. Grattarola, H. J. Butt, P. Skladal, *Sensors and Actuators B* 79 (2001) 115.
- [4] S. J. Pearton, D. P. Norton, K. Ip, Y. W. Heo, T. Steiner, *Progress in Materials Science* 50 (2005) 293.
- [5] S. J. Pearton, C. R. Abernathy, M. E. Overberg, G. T. Thaler, D. P. Norton, N. Theodoropoulou, A. F. Hebard, Y. D. Park, F. Ren, J. Kim, L. A. Boatner, *Journal of Applied Physics* 93 (2003) 1.
- [6] Q. X. Su, P. Kirby, E. Komuro, M. Imura, Q. Zhang, R. Whatmore, *IEEE Trans. Microwave Theory and Techniques* 49 (2001) 769.
- [7] F. Bernardini, V. Fiorentini, D. Vanderbilt, *Physical Review B* 56 (1997) R10024.
- [8] A. R. Hutson, *Physical Review Letters* 4 (1960) 505.
- [9] T. Kawaguchi, H. Adachi, K. Setsune, O. Yamazaki, K. Wasa, *Applied Optics* 23 (1984) 2187.
- [10] J. Koo, J. H. Jang, B. S. Bae, *Journal of Materials Science* 34 (1999) 5075.
- [11] D. J. Jung, F. D. Morrison, M. Cawber, H. H. Kim, K. Kim, J. F. Scott, *Journal of Applied Physics* 95 (2004) 4968.
- [12] K. S. Hwang, *Materials Chemistry and Physics* 57 (1999) 228.
- [13] R. Kurchania, S. J. Milne, *Journal of Materials Research* 14 (1999) 1852.
- [14] S. H. Kim, Y. S. Choi, C. E. Kim, Y. J. Oh, *Journal of Materials Research* 12 (1997) 1576.
- [15] Y. L. Tu, S. J. Milne, *Journal of Materials Science* 30 (1995) 2507.
- [16] S. Mathews, R. Ramesh, T. Venkatesan, J. Benedetto, *Science* 276 (1997) 238.
- [17] P. Gonnard, M. P. Thi, *IEEE International Ultrasonic, Ferroelectrics and Frequency Control* (2004) 51.
- [18] P. Luginbuhl, G. A. Racine, P. Lerch, B. Romanowics, K. G. Brooks, N. F. d. Rooji, P. Renaud, N. Setter, *Sensors and Actuators A* 54 (1996) 530.
- [19] B. Jaffe, W. R. Cook, H. Jaffe, *Piezoelectric ceramics*, Academic press, London and New York, 1971.
- [20] H. Wohltjen, *Sensors and Actuators* 5 (1984) 307.
- [21] J. M. Myung, W. H. Yoon, D. H. Lee, I. Yun, S. H. Bae, S. Y. Lee, *Japan Journal of Applied Physics* 41 (2002) 28.
- [22] Y. R. Ryu, S. Zhu, J. D. Budai, H. R. Chandrasekhar, P. F. Miceli, H. W. White, *Journal of Applied Physics* 88 (2000) 201.
- [23] F. Wen, W. Li, J. H. Moon, J. H. Kim, *Solid State Communications* 135 (2005) 34.

- [24] T. Shiosaki, S. Ohnishi, Y. Hirokawa, A. Kawabata, *Applied Physics Letters* 33 (1978) 406.
- [25] B. S. Li, Y. C. Liu, Z. S. Chu, D. Z. Shen, Y. M. Lu, J. Y. Zhang, X. W. Fan, *Journal of Applied Physics* 91 (2002) 501.
- [26] M. Rebien, W. Henrion, M. Bar, C.-H. Fischer, *Applied Physics Letters* 80 (2002) 3518.
- [27] C. R. Aita, R. J. Lad, T. C. Tisone, *Journal of Applied Physics* 51 (1980) 6405.
- [28] C. R. Aita, A. J. Purdes, R. J. Lad, P. D. Funkenbusch, *Journal of Applied Physics* 51 (1980) 5533.
- [29] J. Aranovich, A. Ortiz, R. H. Bube, *Journal of Vacuum Science and Technology* 16 (1979) 994.
- [30] M. Krunks, E. Mellikov, *Thin Solid Films* 270 (1995) 33.
- [31] Y. Chen, H. J. Ko, S. K. Hong, T. Yao, Y. Segawa, *Applied Physics Letters* 80 (2002) 1358.
- [32] D. M. Bagnall, Y. F. Chen, Z. Zhu, T. Yao, M. Y. Shen, T. Goto, *Applied Physics Letters* 73 (1998) 1038.
- [33] D. Bao, H. Gu, A. Kuang, *Thin Solid Films* 312 (1998) 37.
- [34] V. Fathollahi, M. M. Amini, *Materials Letters* 50 (2001) 235.
- [35] S. Fujihara, C. Sasaki, T. Kimura, *Applied Surface Science* 180 (2001) 341.
- [36] S. Fujihara, C. Sasaki, T. Kimura, *Journal of the European Ceramic Society* 21 (2001) 2109.
- [37] S. K. Kim, S. Y. Jeong, C. R. Cho, *Applied Physics Letters* 82 (2003) 562.
- [38] J. E. Jaffe, R. Pandey, A. B. Kunz, *Physical Review B* 43 (1991) 14030.
- [39] J. E. Jaffe, A. C. Hess, *Physical Review B* 48 (1993) 7903.
- [40] A. Schleife, F. Fuchs, J. Furthmuller, F. Bechstedt, *Physical Review B* 73 (2006) 245212.
- [41] U. Ozgur, Y. I. Alivov, C. Liu, A. Teke, M. A. Reshchikov, S. Dogan, V. Avrutin, S. J. Cho, H. Morkoc, *Journal of Applied Physics* 98 (2005) 041301.
- [42] D. C. Reynolds, D. C. Look, B. Jogai, H. Morkoc, *Solid State Communications* 101 (1997) 643.
- [43] K. K. Kim, J. H. Song, H. J. Jung, W. K. Choi, S. J. Park, J. H. Song, J. Y. Lee, *Journal of Vacuum Science and Technology A* 18 (2000) 2864.
- [44] R. W. Birkmire, E. Eser, *Annual Review of Materials Science* 27 (1997) 625.
- [45] T. L. Yang, D. H. Zhang, J. Ma, H. L. Ma, Y. Chen, *Thin Solid Films* 326 (1998) 60.
- [46] B. Sang, A. Yamada, M. Konagai, *Japan Journal of Applied Physics* 37 (1998) L206.
- [47] A. F. Kohan, G. Ceder, M. Morgan, *Physical Review B* 61 (2000) 15019.
- [48] T. Minami, H. Sato, H. Nanto, S. Takata, *Japan Journal of Applied Physics* 24 (1985) L781.
- [49] I. Sieber, N. Wanderka, I. Urban, I. Dorfel, E. Schierhorn, F. Fenske, W. Fuhs, *Thin Solid Films* 330 (1998) 108.
- [50] Z. L. Pei, C. Sun, M. H. Tan, J. Q. Xiao, G. D.H, R. F. Huang, L. S. Wen, *Journal of Applied Physics* 90 (2001) 3432.
- [51] A. E. Zimenez-Gonzalez, J. A. S. Urueta, R. Suarez-Parra, *Journal of Crystal Growth* 192 (1998) 430.

- [52] D. G. Baik, S. M. Cho, *Thin Solid Films* 354 (1999) 227.
- [53] K. Yoshino, T. Hata, T. Kakeno, H. Komaki, M. Yoneta, Y. Akaki, T. Ikari, *Physica Status Solidi C* 0 (2003) 626.
- [54] B. M. Ataev, A. M. Bagamadova, A. M. Djabrailov, V. V. Mamedov, R. A. Rabadanov, *Thin Solid Films* 260 (1995) 19.
- [55] E. J. Luna-Arredondo, A. Maldonado, R. Asomoza, D. R. Acosta, M. A. Melendez-Lira, M. d. I. L. Olvera, *Thin Solid Films* 490 (2005) 132.
- [56] S. Major, A. Banerjee, K. L. Chopra, *Thin Solid Films* 108 (1983) 333.
- [57] J. H. Lee, B. O. Park, *Thin Solid Films* 426 (2003) 94.
- [58] D. R. Lide, *CRC Handbook of Chemistry and Physics*, CRC Press, Boca Ranton, FL, 2005.
- [59] W. Walukiewicz, *Physical Review B* 50 (1994) 5221.
- [60] N. Ohashi, T. Ishigaki, N. Okada, T. Sekiguchi, I. Sakaguchi, H. Haneda, *Applied Physics Letters* 80 (2002) 2869.
- [61] X. M. Fan, J. S. Lian, Z. X. Guo, H. J. Lu, *Applied Surface Science* 239 (2005) 176.
- [62] B. E. Sernelius, K. F. Berggren, Z. C. Jin, I. Hamberg, C. G. Granqvist, *Physical Review B* 37 (1988) 10244.
- [63] N. A. Spaldin, *Physical Review B* 69 (2004) 125201.
- [64] L. Poul, S. Ammar, N. Jouini, F. Fievet, F. Villain, *Solid State Sciences* 3 (2001) 31.
- [65] T. Itoh, T. Suga, *Nanotechnology* 4 (1993) 218.
- [66] C. C. Chang, S. K. Fang, *International Journal of electronics* 87 (2000) 1013.
- [67] F. C. M. V. d. Pol, F. R. Blom, T. J. A. Popma, *Thin Solid Films* 204 (1991) 349.
- [68] F. S. Hickernell, *Journal of Applied Physics* 44 (1973) 1061.
- [69] F. S. Hickernell, *IEEE Transaction on Sonics and Ultrasonics* 32 (1985) 621.
- [70] J. X. Wang, X. W. Sun, A. Wei, Y. Lei, X. P. Cai, C. M. Li, Z. L. Dong, *Applied Physics Letters* 88 (2006) 233106.
- [71] J. L. Deschanvres, P. Rey, G. Delabouglise, M. Labeau, J. C. Joubert, J. C. Peuzin, *Sensors and Actuators A* 33 (1992) 43.
- [72] J. Valasek, *Physical Review* 17 (1921) 475.
- [73] H. D. Megaw, *Nature* 155 (1945) 484.
- [74] B. Jaffe, R. S. Roth, S. Marzullo, *Journal of Applied Physics* 25 (1954) 809.
- [75] F. F. C. Duval, R. A. Dorey, R. H. Haigh, R. W. Whatmore, *Thin Solid Films* 444 (2003) 235.
- [76] G. A. C. M. Spierings, G. J. M. Dormans, W. G. J. Moors, M. J. E. Ulenaers, P. K. Larsen, *Journal of Applied Physics* 78 (1995) 1926.
- [77] M. Klee, R. Eusemann, R. Waser, W. Brand, H. v. Hal, *Journal of Applied Physics* 72 (1992) 1566.
- [78] G. A. C. M. Spierings, M. J. E. Ulenaers, G. L. M. Kampschoer, H. A. M. v. Hal, *Journal of Applied Physics* 70 (1991) 2290.
- [79] A. J. Moulson, J. M. Herbert, *Electroceramics* (2ed), John Wiley & Sons, west Sussex, England, 2003.
- [80] M. E. Lines, A. M. Glass, *Principles and applications of ferroelectrics and related materials*, Oxford University Press, 1977.
- [81] L. L. Hench, J. K. West, *Principles of electronic ceramics*, John Wiley & Sons, 1990.

- [82] D. Damjanovic, Reports on Progress in Physics 61 (1998) 1267.
- [83] D. Damjanovic, Journal of Applied Physics 82 (1997) 1788.
- [84] S. H. Kim, D. Y. Park, H. J. Woo, D. S. Lee, J. Ha, C. S. Hwang, I. B. Shim, A. I. Kingon, Thin Solid Films 416 (2002) 264.
- [85] F. Li, D. Fang, Mechanics of Materials 36 (2004) 959.
- [86] M. J. Vellekoop, G. W. Lubking, P. M. Sarro, A. Venema, Sensors and Actuators A 43 (1994) 175.
- [87] J. W. Grate, S. J. Martin, R. M. White, Analytical Chemistry 65 (1993) 940A.
- [88] D. S. Ballantine, R. M. White, S. J. Martin, A. J. Ricco, E. T. Zellers, G. C. Frye, H. Wohltjen, Acoustic Wave Sensors: Theory, Design, and Physico-Chemical Applications, Academic Press, 1997.
- [89] J. W. Grate, S. W. Wenzel, R. M. White, Analytical Chemistry 63 (1991) 1552.
- [90] H. Lamb, Proceedings of the Royal Society of London. Series A, containing papers of a Mathematical and Physical Character 93 (1917) 114.
- [91] R. M. White, IEEE International Frequency Control Symposium (1998) 587.
- [92] N. T. Nguyen, R. W. Doering, A. Lal, R. M. White, IEEE Ultrasonic Symposium (1998) 431.
- [93] R. M. Moroney, R. M. White, R. T. Howe, IEEE Micro Electro Mechanical Systems Proceedings (1991) 277.
- [94] R. M. Moroney, R. M. White, R. T. Howe, IEEE Micro Electro Mechanical Systems Proceedings (1990) 182.
- [95] N. T. Nguyen, A. H. Meng, J. Black, R. M. White, Sensors and Actuators 79 (2000) 115.
- [96] R. M. Moroney, R. M. White, R. T. Howe, IEEE Ultrasonic Symposium (1989) 745.
- [97] P. F. Caton, R. M. White, IEEE Micro Electro Mechanical Systems Proceedings (2001) 479.
- [98] P. K. Sekhar, S. Akella, S. Bhansali, Sensors and Actuators A 132 (2006) 376.
- [99] P. Luginbuhl, S. D. Collins, G. A. Racine, M. A. Gretillat, N. F. d. Rooij, K. G. Brooks, N. Setter, Journal of Microelectromechanical System 6 (1997) 337.
- [100] P. Luginbuhl, S. D. Collins, G. A. Racine, M. A. Gretillat, N. F. d. Rooij, K. G. Brooks, N. Setter, MEMS '97 Proc. 10th International Workshop (1997) 327.
- [101] P. Luginbuhl, S. D. Collins, G. A. Racine, M. A. Gretillat, N. F. d. Rooij, K. G. Brooks, N. Setter, Sensors and Actuators A 64 (1998) 41.
- [102] J. H. Lee, K. H. Ko, B. O. Park, Journal of Crystal Growth 247 (2003) 119.
- [103] T. Tsuchiya, T. Emoto, T. Sei, Journal of Non-Crystalline Solids 178 (1994) 327.
- [104] H. Y. Bae, G. M. Choi, Sensors and Actuators B 55 (1999) 47.
- [105] Y. Huang, M. Liu, S. Jiang, Y. Zeng, C. Li, S. Liu, D. Zhou, Microelectronic Engineering 66 (2003) 760.
- [106] D. Fischer, W. J. Varhue, J. Wu, C. A. Whiting, Journal of Microrlrcrtromechanical Systems 9 (2000) 88.
- [107] C. R. Gorla, N. W. Emanetoglu, S. Liang, W. E. Mayo, Y. Lu, M. Wraback, H. Shen, Journal of Applied Physics 85 (1999) 2595.
- [108] I. Petrov, V. Orlinov, A. Misiuk, Thin Solid Films 120 (1984) 55.

- [109] B. M. Ataev, I. K. Kamilov, A. M. Bagamadova, V. V. Mamedov, A. K. Omaev, M. K. Rabadanov, *Materials Science and Engineering B* 68 (1999) 56.
- [110] J. H. Choi, H. Tabata, T. Kawai, *Journal of Crystal Growth* 226 (2001) 493.
- [111] W. Tang, D. C. Cameron, *Thin Solid Films* 238 (1994) 83.
- [112] M. Ohyama, H. Kozuka, T. Yoko, *Thin Solid Films* 306 (1997) 78.
- [113] D. Basak, G. Amin, B. Mallik, G. K. Paul, S. K. Sen, *Journal of Crystal Growth* 256 (2003) 73.
- [114] Y. Ohya, H. Saiki, Y. Takahashi, *Journal of Materials Science* 29 (1994) 4099.
- [115] L. Znaidi, G. J. A. A. S. Illia, R. L. Guennic, C. Sanchez, A. Kanaev, *Journal of Sol-Gel Science and Technology* 26 (2003) 817.
- [116] M. Toyoda, J. Watanabe, T. Matsumiya, *Journal of Sol-Gel Science and Technology* 1/2 (1999) 93.
- [117] S. Chakrabarti, D. Ganguli, S. Chaudhuri, *Materials Letters* 58 (2004) 3952.
- [118] Y. Ohya, H. Saiki, T. Tanaka, Y. Takahashi, *Journal of American Ceramic Society* 79 (1996) 825.
- [119] M. N. Kamalasanan, S. Chandra, *Thin Solid Films* 288 (1996) 112.
- [120] Y. Takahashi, M. Kanamori, A. Kondoh, H. Minoura, Y. Ohya, *Japan Journal of Applied Physics* 33 (1994) 6611.
- [121] Y.-S. Kim, W.-P. Tai, S.-J. Shu, *Thin Solid Films* 491 (2005) 153.
- [122] A. E. J. Gonzales, J. A. S. Urueta, *Solar Energy Materials and Solar Cells* 52 (1998) 345.
- [123] Z. Liu, Z. Jin, W. Li, J. Qiu, *Materials Letters* 59 (2005) 3620.
- [124] H. Li, J. Wang, H. Liu, C. Yang, H. Xu, X. Li, H. Cui, *Vacuum* 77 (2004) 57.
- [125] M. Wang, J. Wang, W. Chen, Y. Cui, L. Wang, *Materials Chemistry and Physics* 97 (2006) 219.
- [126] S. Bandyopadhyay, G. K. Paul, R. Roy, S. K. Sen, S. Sen, *Materials Chemistry and Physics* 74 (2002) 83.
- [127] Z. Y. Xiao, Y. C. Liu, L. Dong, C. L. Shao, J. Y. Zhang, Y. M. Lu, D. Z. Zhen, X. W. Fan, *Journal of Colloid and Interface Science* 282 (2005) 403.
- [128] S. Sakohara, M. Ishida, M. A. Anderson, *Journal of Physical Chemistry B* 102 (1998) 10169.
- [129] D. Mondelaers, G. Vanhoyland, H. V. D. Rul, J. D'Haen, M. K. V. Bael, J. Mullens, L. C. V. Poucke, *Journal of Sol-Gel Science and Technology* 26 (2003) 523.
- [130] M. S. Bhuiyan, M. paranthaman, K. Salama, *Superconductor Science and Technology* 19 (2006) R1.
- [131] M. Ohyama, H. Kozuka, T. Yoko, S. Sakka, *Journal of the ceramic society of Japan* 104 (1996) 296.
- [132] M. Ohyama, H. Kozuka, T. Yoko, *Journal of American Ceramic Society* 81 (1998) 1622.
- [133] Y. Ohya, T. Ogata, T. Ban, Y. Takahashi, *Journal of the Ceramic Society of Japan* 113 (2005) 220.
- [134] M. Tzolov, N. Tzenov, D. Dimova-Malinovska, M. Kalitzova, C. Pizzuto, G. Vitali, G. Zollo, I. Ivanov, *Thin Solid Films* 379 (2000) 28.
- [135] G. J. Exarhos, S. K. Sharma, *Thin Solid Films* 270 (1995) 27.

- [136] A. Pinczuk, E. burstein, *Physical Review Letters* 21 (1968) 1073.
- [137] Y. Huang, M. Liu, Z. Li, Y. Zeng, S. Liu, *materials Science and Engineering B* 97 (2003) 111.
- [138] T. C. Damen, S. P. S. Porto, B. Tell, *Physical Review* 142 (1966) 570.
- [139] R. Job, Formation of Hydrogen related defects and nano-voids in plasma hydrogenated ZnO, in: *Mater. Res. Soc. Symp.*, vol 994, 2007, pp. F02.
- [140] C. J. Youn, T. S. Jeong, M. S. Han, J. H. Kim, *Journal of Crystal Growth* 261 (2004) 526.
- [141] J. Yu, H. Xing, Q. Zhao, H. Mao, Y. Shen, J. Wang, Z. Lai, Z. Zhu, *Solid State Communications* 138 (2006) 502.
- [142] I. K. Oh, D. W. Lee, *Microelectronic Engineering* 84 (2007) 138801392.
- [143] H. Iwanaga, A. Kunishige, S. Takeuchi, *Journal of Materials Science* 35 (2000) 2451.
- [144] S. J. Henley, M. N. R. Ashfold, D. Cherns, *Thin Solid Films* 422 (2002) 69.
- [145] K. Ellmer, *Journal of Physics D:Applied Physics* 33 (2000) R17.
- [146] B. T. Khuri-Yakub, J. G. Smits, *Journal of Applied Physics* 52 (1981) 4772.
- [147] K. B. Sundaram, B. K. Garside, *Journal of Physics D:Applied Physics* 17 (1984) 147.
- [148] S. Onishi, M. Eschwei, W. C. Wang, *Applied Physics Letter* 38 (1981) 419.
- [149] T. Yamamoto, T. Shiosaki, A. Kawabata, *Journal of Applied Physics* 51 (1980) 3113.
- [150] R. Cebullar, R. Wendt, K. Ellmer, *Journal of Applied Physics* 83 (1998) 1087.
- [151] J. Vuillod, *Journal of Vacuum Science and Technology* 9 (1972) 87.
- [152] G. A. Rozgonyi, W. J. Polito, *Applied Physics Letters* 8 (1966) 220.
- [153] E. M. Bachari, G. Baud, S. B. Amor, M. Jacquet, *Thin Solid Films* 348 (1999) 165.
- [154] S. S. Lin, J. L. Huang, *Surface and Coating Technology* 185 (2004) 222.
- [155] J. Hinze, K. Ellmer, *Journal of Applied Physics* 88 (2000) 2443.
- [156] K. B. Sundaram, A. Khan, *Thin Solid Films* 295 (1997) 87.
- [157] G. D. Hillman, H. J. J. Seguin, *Journal of Applied Physics* 44 (1973) 5053.
- [158] S. Zhu, C. H. Su, S. L. Lehoczky, P. Peters, M. A. George, *Journal of Crystal Growth* 211 (2000) 106.
- [159] J. B. Lee, M. H. Lee, C. K. Park, J. S. Park, *Thin Solid Films* 447-448 (2004) 296.
- [160] J. B. Lee, S. H. Kwak, H. J. Kim, *Thin Solid Films* 423 (2003) 262.
- [161] J. Ye, S. Gu, S. Zhu, T. Chen, L. Hu, F. Qin, R. Zhang, Y. Shi, Y. Zheng, *Journal of Crystal Growth* 243 (2002) 151.
- [162] K. Ogata, K. Sakurai, S. Fujita, S. Fujita, K. Matsushige, *Journal of Crystal Growth* 214/215 (2000) 312.
- [163] N. Fujimura, T. Nishihara, S. Goto, J. Xu, T. Ito, *Journal of Crystal Growth* 130 (1993) 269.
- [164] M. Kasuga, M. Mochizuki, *Journal of Crystal Growth* 54 (1981) 185.
- [165] Q. P. Wang, D. H. Zhang, Z. Y. Xue, X. J. Zhang, *Optical Materials* 26 (2004) 23.
- [166] M. B. Assouar, O. Elmazria, R. J. Rioboo, F. Sarry, P. Alnot, *Applied Surface Science* 164 (2000) 200.
- [167] J. C. Lodder, T. Wielinga, J. Worst, *Thin Solid Films* 101 (1983) 61.

- [168] Y. J. Kim, Y. T. Kim, H. K. Yang, J. C. Park, J. I. Han, Y. E. Lee, H. J. Kim, *Journal of Vacuum Science and Technology A* 15 (1997) 1103.
- [169] W. S. Shi, O. Agyeman, C. N. Xu, *Journal of Applied Physics* 91 (2002) 5640.
- [170] S. B. Zhang, S. H. Wei, A. Zunger, *Physical Review B* 63 (2001) 075205.
- [171] Z. B. Fang, Z. J. Yan, Y. S. Tan, X. Q. Liu, Y. Y. Wang, *Applied Surface Science* 241 (2005) 303.
- [172] D. J. Kang, J. S. Kim, S. W. Jeong, Y. Roh, S. H. Jeong, J. H. Boo, *Thin Solid Films* 475 (2005) 160.
- [173] W. T. Lim, C. H. Lee, *Thin Solid Films* 353 (1999) 12.
- [174] B. T. Khuri-Yakub, G. S. Kino, P. Galle, *Journal of Applied Physics* 46 (1975) 3266.
- [175] R. J. H. Voorhoeve, J. N. Carides, R. S. Wagner, *Journal of Applied Physics* 43 (1972) 4876.
- [176] M. S. Wu, W. C. Shih, W. H. Tsai, *Journal of Physics D: Applied Physics* 31 (1998) 943.
- [177] A. v. d. Drift, *Philips Research Reports* 22 (1967) 267.
- [178] Y. Yoshino, K. Inoue, M. Takeuchi, K. Ohwada, *Vacuum* 51 (1998) 601.
- [179] Y. Yoshino, K. Inoue, M. Takeuchi, T. Makino, Y. Katayama, T. Hata, *Vacuum* 59 (2000) 403.
- [180] J. G. E. Gardeniers, Z. M. Rittersma, G. J. Burger, *Journal of Applied Physics* 83 (1998) 7844.
- [181] T. K. Subramanyam, B. S. Naidu, S. Uthanna, *Optical Materials* 13 (1999) 239.
- [182] S. Zhu, C. H. Su, S. L. Lehoczky, M. A. George, D. H. Lowndes, *Journal of Material Research* 15 (2000) 1125.
- [183] T. Mitsuyu, S. Ono, K. Wasa, *Journal of Applied Physics* 51 (1980) 2464.
- [184] R. J. Lad, P. D. Funkenbusch, C. R. Aita, *Journal of Vacuum Science and Technology* 17 (1980) 808.
- [185] H. W. Kim, N. H. Kim, *Materials Science in Semiconductor Processing* 7 (2004) 1.
- [186] K. Koshi, J. Holsa, P. Juliet, *Thin Solid Films* 339 (1999) 240.
- [187] X. H. Li, A. P. Huang, M. K. Zhu, S. L. Xu, J. Chen, H. Wang, B. Wang, H. Yan, *Materials Letters* 57 (2003) 4655.
- [188] M. Matsuoka, K. Ono, *Applied Physics Letter* 53 (1988) 1393.
- [189] S. Y. Chu, T. Y. Chen, W. Water, *Journal of Vacuum Science and Technology A* 22 (2004) 1087.
- [190] J. J. Chen, Y. Gao, F. Zeng, D. M. Li, F. Pan, *Applied Surface Science* 223 (2004) 318.
- [191] J. J. Chen, F. Zeng, D. M. Li, J. B. Niu, F. Pan, *Thin Solid Films* 485 (2005) 257.
- [192] R. Ondo-Ndong, G. Ferblantier, M. A. Kalfioui, A. Boyer, A. Foucaran, *Journal of Crystal Growth* 255 (2003) 130.
- [193] Z. Li, W. Gao, *Materials Letters* 58 (2004) 1363.
- [194] K. Tominaga, I. Mori, *Vacuum* 59 (2000) 574.
- [195] P. Sharma, K. Sreenivas, K. V. Rao, *Journal of Applied Physics* 93 (2003) 3963.
- [196] S. B. Krupanodhi, M. Sayer, *Journal of Applied Physics* 56 (1984) 3308.

- [197] K. Tominaga, S. Iwamura, Y. Shintani, O. Tada, Japanese Journal of Applied Physics 21 (1982) 688.
- [198] P. K. Dutta, H. Wilman, Journal of Physics D:Applied Physics 4 (1971) 1971.
- [199] A. G. Dirks, H. J. Leamy, Thin Solid Films 47 (1977) 219.
- [200] F. J. Hickernell, IEEE Ultrasonics Symposium (1977) 309.
- [201] J. A. Thornton, D. W. Hoffman, Thin Solid Films 171 (1989) 5.
- [202] J. H. Jou, M. Y. han, D. J. Cheng, Journal of Applied Physics 71 (1992) 4333.
- [203] Y. F. Li, B. Yao, Y. M. Lu, C. X. Cong, Z. Z. Zhang, Y. Q. Gai, C. J. Zheng, B. H. Li, Z. P. Wei, D. Z. Shen, X. W. Fan, L. Xiao, S. C. Xu, Y. Liu, Applied Physics Letter 91 (2007) 021915.
- [204] J. A. Thornton, J. Tabock, D. W. Hoffman, Thin Solid Films 64 (1979) 111.
- [205] D. W. Hoffman, J. A. Thornton, Thin Solid Films 40 (1977) 355.
- [206] A. Cimpoiasu, N. M. v. d. Pers, T. H. d. Keyser, A. Venema, M. J. Vellekoop, Smart Materials & Structures 5 (1996) 744.
- [207] S. S. Lin, J. L. Huang, D. F. Lii, Surface and Coating Technology 176 (2004) 173.
- [208] W. W. Lee, D. Oblas, Journal of Vacuum Science and Technology 7 (1970) 129.
- [209] H. F. Winters, E. Kay, Journal of Applied Physics 38 (1967).
- [210] H. D. Hagstrum, Physical Review 123 (1961) 758.
- [211] R. Menon, K. Sreenivas, V. Gupta, Journal of Applied Physics 103 (2008) 094903.
- [212] V. P. Kutepova, D. A. Hall, IEEE Ultrasonics Symposium (1998) 213.
- [213] Y. E. Lee, J. B. Lee, Y. J. Kim, H. K. Yang, J. C. Park, H. J. Kim, Journal of Vacuum Science and Technology A 14 (1996) 1943.
- [214] J. J. Garrido, D. Gerstenberg, R. W. Berry, Thin Solid Films 41 (1977) 87.
- [215] H. Wang, T. Wang, P. Xu, Journal of Materials Science: Materials in Electronics 9 (1998) 327.
- [216] M. K. Puchert, P. Y. Timbrell, R. N. Lamb, Journal of Vacuum Science and Technology A 14 (1996) 2220.
- [217] T. Hanbusa, H. Hosoda, K. Kusaka, K. Tominaga, Thin Solid Films 343-344 (1999) 164.
- [218] M. J. Brett, R. R. Parsons, Journal of Materials Science 22 (1987) 3611.
- [219] E. Kay, Journal of Vacuum Science and Technology A 4 (1986) 462.
- [220] J. A. Thornton, Thin Solid Films 40 (1977) 335.
- [221] R. Navamathavan, K. K. Kim, D. K. Hwang, S. J. Park, J. H. Hahn, T. G. Lee, G. S. Kim, Applied Surface Science 253 (2006) 464.
- [222] S. O. Kucheyev, J. E. Bradby, J. S. Williams, C. Jagadish, M. V. Swain, Applied Physics Letter 80 (2002) 956.
- [223] M. Ohring, Materials Science of Thin Films, Academic Press, 2002.
- [224] P. H. Kobrin, A. B. Harker, Journal of Materials Science 24 (1989) 1363.
- [225] S. B. Krupanidhi, N. Maffei, M. Sayer, K. El-Assal, Journal of Applied Physics 54 (1983) 6601.
- [226] N. Nagao, T. Takeuchi, K. Iljima, Japan Journal of Applied Physics 32 (1993) 4065.
- [227] D. Roy, S. B. Krupanidhi, J. P. Dougherty, Journal of Applied Physics 69 (1991) 7930.
- [228] J. Lappalainen, J. Frantti, V. Lantto, Journal of Applied Physics 82 (1997) 3469.

- [229] K. S. Lee, J. H. Choi, J. Y. Lee, S. Baik, *Journal of Applied Physics* 90 (2001) 4095.
- [230] B. S. Kwak, A. Erbil, J. D. Budai, M. F. Chisholm, L. A. Boatner, B. J. Wilkens, *Physical Review B* 49 (1994) 14865.
- [231] B. S. Kwak, A. Erbil, B. J. Wilkens, J. D. Budai, M. F. Chisholm, L. A. Boatner, *Physical Review Letters* 68 (1992) 3733.
- [232] C. M. Foster, Z. Li, M. Buckett, D. Miller, P. M. Baldo, L. E. Rehn, G. R. Bai, D. Guo, H. You, K. L. Merkle, *Journal of Applied Physics* 78 (1995) 2607.
- [233] K. D. Budd, S. K. Dey, D. A. Payne, *Proceedings of British Ceramic Society* 36 (1985) 107.
- [234] M. L. Calzada, S. J. Milne, *Journal of Materials Science Letters* 12 (1993) 1221.
- [235] R. W. Schwartz, *Chemistry of Materials* 9 (1997) 2325.
- [236] D. Kaewchinda, T. Chairaungsri, M. Naksata, S. J. Milne, R. Brydson, *Journal of the European Ceramic Society* 20 (2000) 1277.
- [237] R. W. Schwartz, R. A. Assink, D. Dimos, M. B. Sinclair, T. J. Boyle, C. D. Buchheit, *Proceedings of Materials Research Society Symposium* 361 (1995) 377.
- [238] C. Sanchez, L. Livage, M. Henry, F. Babonneau, *Journal of Non-Crystalline Solids* 100 (1988) 65.
- [239] H. Kozuka, S. Takenaka, H. Tokita, T. Hirono, Y. Higashi, T. Hamatani, *Journal of Sol-Gel Science and Technology* 26 (2003) 681.
- [240] S. Hirano, T. Yogo, K. Kikuta, Y. Araki, M. Saitoh, S. Ogasahara, *Journal of American Ceramic Society* 75 (1992) 2785.
- [241] R. W. Schwartz, J. A. Voigt, B. A. Tuttle, D. A. Payne, T. L. Reichert, R. S. DaSalla, *Journal of Materials Research* 12 (1997) 444.
- [242] Z. Huang, Q. Zhang, R. W. Whatmore, *Journal of Applied Physics* 86 (1999) 1662.
- [243] K. S. Hwang, T. Manabe, T. Nagahama, I. Yamaguchi, T. Kumagai, S. Mizuta, *Thin Solid Films* 347 (1999) 106.
- [244] S. Yokoyama, Y. Honda, H. Morioka, S. Okamoto, H. Funakubo, T. Iijima, H. Matsuda, K. Saito, T. Yamamoto, H. Okino, O. Sakata, S. Kimura, *Journal of Applied Physics* 98 (2005) 094106.
- [245] P. Muralt, T. Maeder, L. Sagalowicz, S. Hiboux, S. Scalese, D. Naumovic, R. G. Agostino, N. Xanthopoulos, H. J. Mathieu, L. Patthey, E. L. Bullock, *Journal of Applied Physics* 83 (1998) 3835.
- [246] Z. Chen, C. Yang, B. Li, M. Sun, B. Yang, *Journal of Crystal Growth* 285 (2005) 627.
- [247] J. H. Kim, F. F. Lange, *Journal of Materials Research* 14 (1999) 1626.
- [248] T. Maeder, P. Muralt, L. Sagalowicz, I. Reaney, M. Kohli, A. Kholkin, N. Setter, *Applied Physics Letter* 68 (1996) 776.
- [249] S. Y. Chen, I. W. Chen, *Journal of American Ceramic Society* 81 (1998) 97.
- [250] L. Fe, G. J. Norga, D. J. Wouters, H. E. Maes, *Journal of Materials Research* 16 (2001) 2499.
- [251] K. G. Brooks, I. M. Reaney, R. Klissurska, Y. Huang, L. Bursill, N. Setter, *Journal of Materials Research* 9 (1994) 2540.

- [252] I. M. Reaney, K. Brooks, R. Klissurska, C. Pawlaczyk, N. Setter, *Journal of The American Ceramic Society* 77 (1994) 1209.
- [253] C. W. Law, K. Y. Tong, J. H. Li, K. Li, *Thin Solid Films* 335 (1998) 220.
- [254] T. Mihara, S. Mochizuki, S. Kimura, R. Makabe, *Japanese Journal of Applied Physics* 31 (1992) 1872.
- [255] P. R. Coffman, C. K. Barlingay, A. gupta, S. K. Dey, *Journal of Sol-Gel Science and Technology* 6 (1996) 83.
- [256] L. Fe, G. Norga, D. J. Wouters, R. Nouwen, L. C. v. Poucke, *Journal of Sol-Gel Science and Technology* 19 (2000) 149.
- [257] M. L. Calzada, R. Sirera, F. Carmona, B. Jimenez, *Journal of American Ceramic Society* 78 (1995) 1802.
- [258] A. Leautic, F. Babonneau, J. Livage, *Chemistry of Materials* 1 (1989) 240.
- [259] S. Doeuff, M. Henry, C. Sanchez, J. Livage, *Journal of Non-Crystalline Solids* 89 (1987) 206.
- [260] H. G. Mcadie, *Journal of Inorganic and Nuclear Chemistry* 28 (1966) 2801.
- [261] J. Laubersheimer, H. J. Ritzhaupt-Kleissl, J. Haubelt, G. Emig, *Journal of the European Ceramic Society* 18 (1998) 255.
- [262] G. J. Norga, L. Fe, *Proceedings of Materials Research Society Symposium* 655 (2001) CC9.1.1.
- [263] A. D. Polli, F. F. Lange, C. G. Levi, *Journal of American Ceramic Society* 83 (2000) 873.
- [264] R. Ramesh, H. Gilchrist, T. Sands, V. G. Keramidas, R. Haakenaasen, D. K. Fork, *Applied Physics Letters* 63 (1993) 3592.
- [265] T. J. Zhu, L. Lu, M. O. Lai, *Sensors and Actuators A* 125 (2006) 335.
- [266] S. Y. Chen, I. W. Chen, *Journal of American Ceramic Society* 77 (1994) 2332.
- [267] K. Aoki, Y. Fukuda, K. Numata, A. Nishimura, *Japan Journal of Applied Physics* 34 (1995) 192.
- [268] G. J. Norga, L. Fe, F. Vasiliu, J. Fompeyrine, J. P. Locquet, O. V. d. Biest, *Journal of the European Ceramic Society* 24 (2004) 969.
- [269] P. Muralt, *Journal of Micromechanics and Microengineering* 10 (2000) 136.
- [270] G. J. Norga, F. Vasiliu, L. Fe, D. J. Wouters, O. V. d. Biest, *Journal of Materials Research* 18 (2003) 1232.
- [271] A. P. Wilkinson, J. S. Speck, A. K. Cheetham, S. Natarajan, J. M. Thomas, *Chemistry of Materials* 6 (1994) 750.
- [272] L. J. Schowalter, R. W. Fathauer, R. P. Goehner, L. G. Turner, R. W. DeBlois, S. Hashimoto, J. L. Peng, W. M. Gabson, J. P. krusius, *Journal of Applied Physics* 58 (1985) 302.
- [273] A. Seifert, F. F. Lange, J. S. Speck, *Journal of Materials Research* 10 (1995) 680.
- [274] C. J. Kim, D. S. Yoon, J. S. Lee, C. G. Choi, K. No, *Japan Journal of Applied Physics* 33 (1994) 2675.
- [275] A. G. S. Filho, K. C. V. Lima, A. P. Ayala, I. Guedes, P. T. C. Freire, F. E. A. Melo, J. M. Filho, E. B. Araujo, J. A. Eiras, *Physical Review B* 66 (2002) 132107.
- [276] W. H. Xu, D. Lu, T. Y. Zhang, *Applied Physics Letters* 79 (2001) 4112.

- [277] M. Takashige, T. Nakamura, Japan Journal of Applied Physics, Suppl. 20-4 20 (1981) 43.
- [278] K. Saito, T. Kurosawa, T. Akai, T. Oikawa, H. Funakubo, Journal of Applied Physics 93 (2003) 545.
- [279] H. Morioka, G. Asano, T. Oikawa, H. Funakubo, Applied Physics Letters 82 (2003) 4761.
- [280] J. L. Jones, E. B. Slamovich, K. J. Bowman, Journal of Applied Physics 97 (2005) 034113.
- [281] B. Noheda, J. A. Gonzalo, L. E. Cross, R. Guo, S. E. Park, D. E. Cox, G. Shirance, Physical Review B 61 (2000) 8687.
- [282] B. Noheda, D. E. Cox, G. Shirance, R. Guo, B. Jones, L. E. Cross, Physical Review B 63 (2000) 014103.
- [283] D. E. Cox, B. Noheda, G. Shirane, Y. Uesu, K. Fujishiro, Y. Yamada, Applied Physics Letters 79 (2001) 400.
- [284] K. C. V. Lima, A. G. S. Filho, A. P. Ayala, J. M. Filho, P. T. C. Freire, F. E. A. Melo, E. B. Araujo, J. A. Eiras, Physical Review B 63 (2001) 184105.
- [285] G. Burns, B. A. Scott, Physical Review B 7 (1973) 3088.
- [286] I. Taguchi, A. Pignolet, L. Wang, M. Proctor, F. Levy, P. E. Schmid, Journal of Applied Physics 73 (1993) 394.
- [287] J. Frantti, V. Lantto, Physical Review B 56 (1997) 221.
- [288] M. Deluca, T. Sakashita, G. Pezzotti, Applied Physics Letters 90 (2007) 051919.
- [289] P. S. Dobal, R. S. Katiyar, Journal of Raman Spectroscopy 33 (2002) 405.
- [290] W. Cao, L. E. Cross, Physical Review B 47 (1993) 4825.
- [291] G. Burns, J. A. Sanjurjo, E. Lopez-Cruz, Physical Review B 30 (1984) 7170.
- [292] J. A. Sanjurjo, E. Lopez-Cruz, G. Burns, Physical Review B 28 (1983) 7260.
- [293] J. Haines, J. Rouquette, V. Bornand, M. Pintard, P. Papet, F. A. Gorelli, Journal of Raman Spectroscopy 34 (2003) 519.
- [294] H. Furuta, S. Endo, L. C. Ming, H. Fujishita, Journal of Physics and Chemistry of Solids 60 (1999) 65.
- [295] F. Cerdeira, W. B. Holzapfel, D. Bauerle, Physical Review B 11 (1975) 1188.
- [296] W. H. Ma, M. S. Zhang, L. Shun, Z. Yin, Q. Chen, Y. F. Chen, N. B. Ming, Applied Physics A 62 (1996) 281.
- [297] S. H. Lee, H. M. Jang, S. M. Cho, G. C. Yi, Applied Physics Letters 80 (2002) 3165.
- [298] C. M. Foster, Z. Li, M. Grimsditch, S. K. Chan, D. J. Lam, Physical Review B 48 (1993) 10160.
- [299] M. Deluca, T. Sakashita, C. Galassi, G. Pezzotti, Journal of the European Ceramic Society 26 (2006) 2337.
- [300] S. Pojprapai(Imlao), J. L. Jones, M. Hoffman, Applied Physics Letters 88 (2006) 162903.
- [301] J. F. Meng, R. S. Katiyar, G. T. Zou, X. H. Wang, Physica Status Solidi A 164 (1997) 851.
- [302] S. H. Lee, H. M. Jang, H. H. Sung, H. Yi, Applied Physics Letters 81 (2002) 2439.

- [303] K. Kim, M. Yoo, S. Lee, D. Kim, S. Bae, M. Lee, IEEE International Symposium on Applications of Ferroelectrics (2000) 929.
- [304] S. Trolier-McKinstry, P. Muralt, Journal of Electroceramics 12 (2004) 7.
- [305] N. Tirole, A. Choujaa, D. Hauden, G. Martin, P. Blind, M. Froelicher, J. C. Pommier, A. Cachard, IEEE Ultrasonic Symposium (1993) 371.
- [306] B. Cunningham, M. Weinberg, J. Pepper, C. Clapp, R. Bousquet, B. Hugh, R. Kant, C. Daly, E. Hauser, Sensors and Actuators B 73 (2001) 112.
- [307] M. S. Weinberg, B. T. Cunningham, C. W. Clapp, Journal of Microelectromechanical System 9 (2000) 370.
- [308] A. Bryant, D. L. Lee, J. F. Vetelino, IEEE Ultrasonic Symposium (1981) 171.
- [309] C. T. Chuang, R. M. White, J. J. Berstein, IEEE Electron Device Letters 3 (1982) 145.
- [310] R. M. White, P. J. Wicher, S. W. Wenzel, E. T. Zellers, IEEE Ultrasonic Symposium (1987) 162.
- [311] K. Uozumi, K. Ohson, R. M. White, Applied Physics Letters 43 (1983) 917.
- [312] C. T. Chuang, R. M. White, IEEE Ultrasonic Symposium (1982) 295.
- [313] S. Shin, N. E. Lee, H. D. Park, J. S. Park, J. Lee, Integrated Ferroelectrics 80 (2006) 355.
- [314] H. Dabirikhah, C. W. Turner, IEEE Ultrasonic Symposium (1992) 313.
- [315] C. S. Lee, K. No, D. M. Wee, IEEE Ultrasonic Symposium (1999) 493.
- [316] A. Choujaa, N. Tirole, C. Bonjour, G. Martin, D. Hauden, P. Blind, A. Cachard, C. Pommier, Sensors and Actuators A 46-47 (1995) 179.
- [317] Y. Wu, M. d. Labachellerie, F. Bastien, Sensors and Actuators A 100 (2002) 214.
- [318] M. Hoummady, D. Hauden, Sensors and Actuators A 44 (1994) 177.
- [319] H. Jia, R. Duhamel, J. F. Manceau, M. d. Labachellerie, F. Bastien, Sensors and Actuators A 121 (2005) 321.
- [320] B. A. Martin, S. W. Wenzel, R. M. White, Sensors and Actuators A21-A23 (1990) 704.
- [321] V. Rajendran, M. Koike, K. Hashimoto, M. Yamaguchi, IEEE Ultrasonic Symposium (1992) 263.
- [322] S. W. Wenzel, R. M. White, Applied Physics Letters 54 (1976) 1976.
- [323] Q. Y. Cai, J. Park, D. Heldsinger, M. D. Hsieh, E. T. Zellers, sensors and Actuators B 62 (2000) 121.
- [324] B. J. Costello, B. A. Martin, R. M. White, IEEE Ultrasonic Symposium (1989) 977.
- [325] R. M. White, S. W. Wenzel, Applied Physics Letters 52 (1988) 1653.
- [326] M. J. Vellekoop, A. J. v. Rhijn, G. W. Lubking, A. Venema, IEEE Ultrasonic Symposium (1990) 275.
- [327] S. W. Wenzel, R. M. White, Sensors and Actuators A21-A23 (1990) 700.
- [328] J. W. Grate, S. W. Wenzel, R. M. White, Analytical Chemistry 64 (1992) 413.
- [329] A. W. Wang, B. J. Costello, R. M. White, Analytical Chemistry 65 (1993) 1639.
- [330] I. Y. Huang, M. C. Lee, Y. W. Chang, R. S. Huang, IEEE International Symposium on Industrial Electronics (ISIE 2007) (2007) 2736.
- [331] Z. Wang, J. Miao, T. Xu, L. Yu, C. M. Li, X. Chen, Proceedings of the 3rd IEEE International Conference on Nano/Micro Engineered and Molecular Systems (2008) 374.

- [332] J. P. Black, B. Chen, R. Quinn, M. Madou, R. M. White, IEEE Ultrasonic Symposium (2000) 435.
- [333] R. M. White, IEEE Ultrasonic Symposium (1985) 490.
- [334] B. J. Costello, S. W. Wenzel, A. Wang, R. M. White, IEEE Ultrasonic Symposium (1990) 279.
- [335] J. C. Pyun, H. Beutel, J. U. Meyer, H. H. Ruf, Biosensor & Bioelectronics 13 (1998) 839.
- [336] S. W. Wenzel, R. M. White, IEEE Transaction on Electron Devices 35 (1988) 735.
- [337] T. Laurent, F. O. Bastien, J. C. Pommier, A. Cachard, D. Remiens, E. Cattan, Sensors and Actuators 87 (2000) 26.
- [338] K. R. Williams, R. S. Muller, Journal of Microrlrectromechanical Systems 5 (1996) 256.
- [339] T. Maeder, P. Muralt, L. Sagalowicz, Thin Solid Films 345 (1999) 300.
- [340] J. D. N. Cheeke, Fundamentals and applications of ultrasonic waves, CRC Press, Boca Raton, FL, 2002.
- [341] I. A. Viktorov, Rayleigh and Lamb Waves: Physical Theory and Applications, Plenum Press, New York, 1967.
- [342] L. M. Dorozhkin, I. A. rozanov, Journal of Analytical Chemistry 56 (2001) 399.
- [343] K. Fujii, R. Masui, Journal of the Acoustical Society of America 93 (1993) 276.
- [344] C. Campbell, Surface acoustic wave devices and their signal processing applications, Academic Press, 1989.
- [345] A. J. Ricco, S. J. Martin, G. C. Frye, T. M. Niemczyk, IEEE Solid State Sensor and Actuator Workshop (1988) 23.
- [346] R. M. White, F. W. Volmer, Journal of Applied Physics 7 (1965) 314.
- [347] A. J. Devries, Surface wave bandpass filters in 'Surface wave filters', John Wiley & Sons, 1977.
- [348] T. Laurent, F. Bastien, Journal of the Acoustical Society of America 99 (1996) 2876.
- [349] K. Toda, Journal of Applied Physics 44 (1973) 56.
- [350] S. G. Joshi, Y. Jin, Journal of Applied Physics 69 (1991) 8018.
- [351] G. S. Kino, Acoustic Waves: Devices, Imaging, and Analog Signal Processing, Pretice-Hall, INC, Englewood Cliffs, New Jersey, 1987.
- [352] C. T. Chuang, R. M. White, IEEE Untrasonics Symposium (1981) 159.